



Universiteit  
Leiden  
The Netherlands

## **Towards optical detection of a single electron**

Moradi, A.

### **Citation**

Moradi, A. (2021, February 23). *Towards optical detection of a single electron. Casimir PhD Series*. Retrieved from <https://hdl.handle.net/1887/3149275>

Version: Publisher's Version

License: [Licence agreement concerning inclusion of doctoral thesis in the Institutional Repository of the University of Leiden](#)

Downloaded from: <https://hdl.handle.net/1887/3149275>

**Note:** To cite this publication please use the final published version (if applicable).

Cover Page



Universiteit Leiden



The handle <https://hdl.handle.net/1887/3149275> holds various files of this Leiden University dissertation.

**Author:** Moradi, A.

**Title:** Towards optical detection of a single electron

**Issue Date:** 2021-02-23

# Towards Optical Detection of a Single Electron

Amin Moradi



# **Towards Optical Detection of a Single Electron**

Proefschrift

ter verkrijging van  
de graad van Doctor aan de Universiteit Leiden,  
op gezag van Rector Magnificus Prof. dr. ir. H. Bijl,  
volgens besluit van het College voor Promoties  
te verdedigen op woensdag 23 februari 2021  
klokke 11.15 uur

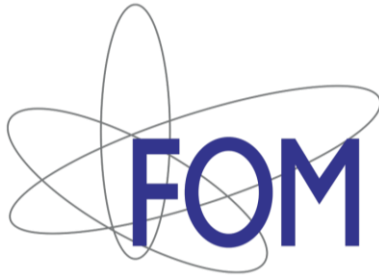
door

Amin Moradi

geboren te Shahrood, Iran  
in 1985

Promotor: Prof. dr. M.A.G.J. Orrit  
Co-promotor: Prof. dr. ir. S.J. van der Molen

Promotiecommissie: Dr. S. Faez (Utrecht University)  
Prof. dr. ir. H.S.J. van der Zant (Delft University of Technology)  
Prof. dr. J. Aarts  
Prof. dr. E.J.J. Groenen  
Prof. dr. J.M. van Ruitenbeek



Casimir PhD series, Delft-Leiden 2021-42

ISBN 978-90-8593-466-0

An electronic version of this thesis can be found at <https://openaccess.leidenuniv.nl>

The work described in this thesis is part of the research program of the Foundation of Fundamental Research on Matter (FOM), which is now part of Netherlands Organization for Scientific Research (NOW). Part of this research is supported by ORQUID, a project of the EraNET cofund Initiatives QuantERA. The research of this thesis was performed at Leiden University.

Cover: designed by Amin Moradi and drawn by Ms. Forough Moosavi. It shows a girl staring at a sky full of shooting stars, dreaming of having a greater share in society. The sky is actually the DBT:DBN Stark shift data from this thesis. The cover represents the writer's support for increasing women's contribution to science.

*To my lovely sisters*





## Table of Content

Chapter 1. Introduction	11
1.1. Single-Molecule Fluorescence Spectroscopy and Microscopy	12
1.2. SMS experimental setup	15
1.3. Molecule sensitivity to electric field	16
1.4. Outline	17
References	18
Chapter 2: Matrix-induced Linear Stark Effect of Single Dibenzoterrylene Molecules in 2,3-Dibromonaphthalene Crystal	23
2.1. Introduction	24
2.2. Experimental Section	25
2.2.1. Crystal Growth	25
2.2.2. Optical Microscopy	25
2.2.3. Quantum Chemistry Calculations	26
2.3. Results	27
2.3.1. Photophysical Properties of the System	27
2.3.2. Stark Effect Experiments	28
2.3.3. Quantum Chemistry Calculations	31
2.4. Discussion	33
2.5. Conclusions	34
2.6. Supporting information	35
2.6.1. Crystal Alignment for the Stark Experiment	35
2.6.2. Calculation of the Stark Shifts: Four-dipoles Model	36
2.6.3. Unit cell and glide planes of the DBN host crystal	37
2.6.4. DFT Calculations	38
References	41
Chapter 3: Laser-Induced Frequency Tuning of Fourier-Limited Single-Molecule Emitters	45
3.1 Introduction	46
3.2. Methods	47
3.2.1. Sublimation growth of DBT:DBN single crystals	47
3.2.2. Preparation of DBT:Ac Nanocrystals	47
3.2.3. Optical Microscopy (DBT:DBN)	48
3.2.4. Optical Microscopy (DBT:Ac)	48
3.3. Results and discussions	49
3.3.1. Characterization of the light-induced frequency shift	51
3.3.2. Tuning molecules into resonance	53
3.3.3. Photoionization model of the laser-induced charge separation	55
3.4. Conclusion	58
3.5. Supporting Information	59
3.5.1. Measurements of DBT:Ac nanocrystals	59
Shift dependence of power and pump laser wavelength	59

Measurement of the photon statistics: single photon purity	60
Independence on the sample substrate	61
3.5.2. Measurements of DBT:DBN single crystals	62
Single-molecule trajectories and inter-molecular heterogeneity	62
Power law behavior of individual trajectories	63
Spectral shift power dependence in DBT:DBN	64
Background fluorescence	64
Dibenzoterrylene in polycrystalline naphthalene	66
3.5.3. Quantum chemistry calculations	67
Calculations on isolated molecules	67
Energies of the excited electronic states of DBT	67
Calculations of locally excited (LE) and charge-transfer (CT) states	68
Electronic states and transitions of bimolecular DBT/DBN system	69
Electronically excited states of DBT:Ac system	70
Recovery of neutral DBT	72
Consistency of the model with experiments	74
References	77
Supplementary_References	80
Chapter 4: Single-electron control for optical charge detection	83
4.1. Single-electron transfer and control.	84
4.1.1. Coulomb blockade	84
4.1.2. Charge quantization and charging energy	84
4.1.3. Self-capacitance of an island	86
4.1.4. Barrier	86
4.2. Single-electron transistor	87
4.2.1. Current through a SET	88
4.2.2. SETs for optical charge detection.	89
4.3. Optical detection of an electron by using SET	90
4.4. Conclusion	91
References	92
Chapter 5: Single-electron fabrication	95
5.1. Electron beam Lithography	96
5.1.1. Substrate preparation	96
5.1.2. Resist coating	97
5.1.3. E-beam pattern generator	98
5.1.4. Development, descum and metal deposition	99
5.2. Self-assembly	100
5.3. Hybrid recipe to make SETs	102
5.3.1. Atomic Layer Deposition	103
5.3.2. Final recipe for making SETs	105
5.4. Sample storage and transport	108
5.5. Electrical measurements	109
5.6. Conclusion	110
References	111
Chapter 6: Seeking for single-electron signals	115
6.1. Sample preparation	116
6.1.1. Crystal transfer to the chip	116

6.1.2. Wire bonding	117
6.1.3. sample transportation	117
6.2. Experimental section	118
6.2. Results and Discussion	119
6.4. Conclusion	121
Summary	123
Samenvatting	127
Curriculum Vitae	131
List of Publication	133
Acknowledgments	135



# 1

## Introduction

Competition for miniaturizing electronic circuits and pushing their extent to the size of atoms and molecules has intensified significantly. Concurrently, quantum integrated photonics circuits are considered as a reliable platform to build quantum computers. The key to nanoelectronics, quantum technology, and the fabrication of quantum integrated devices is a correct understanding of the rules governing the nanoworld. Gaining knowledge in the field of nanotechnology demands developing and advancing our observation tools. Different types of electron microscopes, atomic force microscopes (AFM), optical imaging systems, and many other techniques were developed to enable insights into nanoscience. In many of these techniques, the observation is limited to the surface of the sample, whereas its inner parts remain unexplored. Moreover, the act of measuring by itself may alter the measurement circumstances or even damage the sample. For instance, bombarding the sample with high-energy electrons during scanning electron microscopy can change the sample's structure dramatically (a well-known effect is carbonaceous film formation on the surface of the sample).<sup>1,2</sup> Another example is atomic force microscopy (AFM), where a direct contact of the tip may damage both sample and AFM's tip.<sup>3-5</sup> Among nanoscience methods, the optical methods are exceptional because of their ability to observe and probe a sample without disturbing it. However, the advantage of contactless monitoring by optical methods comes at the cost of a severe diffraction limit in spatial resolution, which appears as a major obstacle to their use at nanometer scales. The invention of single-molecule spectroscopy<sup>6</sup> and super-resolution microscopy<sup>7</sup> broke through this limit and made the optical detection of individual molecules possible.

The light emitted and absorbed by molecules contains information not only about the molecule itself but also about its local environment. Single-molecule spectroscopy (SMS) translates this information into a detectable signal. In a single-molecule experiment, the molecule acts as an extremely sensitive immediate probe of its local environment. The local information can be received and read out as changes in the spectral response of the probe molecule.<sup>8-12</sup> Many different molecular systems have been developed to screen changes in nano-environment, from temperature,<sup>13-17</sup> electric fields,<sup>17-25</sup> to mechanical stress<sup>26-28</sup> and pressure in a crystal.<sup>29</sup> In addition, a single fluorescent molecule is an excellent single-photon light source capable of producing millions of photons per second<sup>30-32</sup> that is comparable with other single-photon emitters such as impurity vacancy centers and quantum dots. All these applications depend on accurate knowledge of the optical properties of molecular systems that can be performed using spectroscopy.

## 1.1. Single-molecule fluorescence spectroscopy and microscopy

Abbe's optical diffraction limit states that the smallest resolvable distance between the features in an optical system is about half the illumination light wavelength. This limits the resolution of optical microscopes to about 200 nm for visible light. However, optical detection of single atoms in the gas phase exists for almost 50 years.<sup>33-35</sup> In many applications such as remote sensing in biology and solid-state physics or as coherent single-photon sources in quantum physics, the molecule needs to be immersed inside its natural medium, i.e., it is surrounded by many other molecules. Such an environment is completely different from the ultrahigh vacuum needed for single-atom detection. In 1990, Orrit and Bernard have shown that it is possible to resolve one molecule of pentacene embedded inside a crystal of p-terphenyl.<sup>6</sup> Considering the

size of a fluorescent molecule (of the order of 1 nm) and the crowded environments of the molecule, this detection is far beyond all mentioned limits and shows the fantastic capability of single-molecule spectroscopy (SMS). SMS is based on high-resolution fluorescence excitation spectroscopy driven by a tunable narrow-band laser. The emission and absorption energy of a molecule is randomly shifted by defects in its environment, and this energy is used to spatially address each molecule in a crystal lattice<sup>7,36–38</sup> and to spectrally resolve it in low-temperature measurements.<sup>8,9</sup>

The invention of SMS was an outstanding step toward visualizing the nanoscale phenomena. It brought the ability to study nature on its simplest level, avoiding the complexities of an ensemble measurement. As fluorescent molecules are small, they can be easily placed in the vicinity of the desired phenomenon in a crystal or attached to proteins inside a cell. They are flexible and can be designed and synthesized for a specific application. Thanks to the methods of synthetic chemistry, probe molecules in a molecular system are replicated with identical chemical structures, making single-molecule data as reproducible as theoretically possible. All these phenomenal features made molecules and SMS a popular tool in biology, chemistry, solid-state physics, and quantum physics. In our experiments, we took advantage of high-resolution single-molecule spectroscopy at liquid-helium temperatures to spectrally select fluorescent molecules and study their optical properties in different host molecular systems.

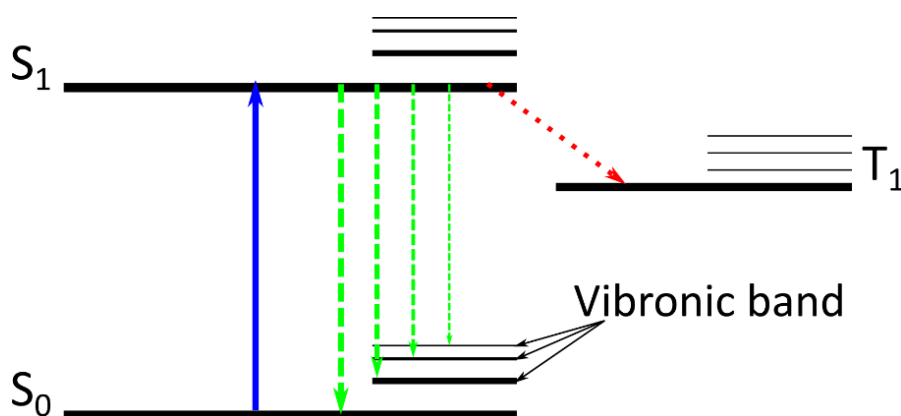


**Figure 1.1:** Energy diagram of a molecule presenting singlet ground  $S_0$  and first excited state  $S_1$  and the triplet state  $T_1$ , each with their vibrational or vibronic bands. The blue solid arrow shows absorption, the green dashed arrows show fluorescence emission, and the red dotted arrow shows intersystem crossing to the triplet state.

The basic principle of SMS can be described by the energy diagram of a single organic molecule showed in Figure 1.1. The diagram presents the molecule's ground electronic state  $S_0$ , excited state  $S_1$ , and the lowest triplet state  $T_1$ . For each energy level several vibrational levels are also shown. In a typical SMS measurement, the molecule is pumped by a laser from the lowest vibrational ground-state energy level to the lowest vibrational level of the first excited state, commonly denoted as (0-0) transition. This transition is purely electronic, i.e., it does not involve any creation or destruction of vibrational quanta and is therefore called the zero-phonon line (ZPL). The excited molecule relaxes back to its ground state by either releasing the energy as heat or emitting a photon (green dashed arrows in Figure 1.1). The emitted light is called fluorescence and has equal energy to, or lower energy than, the excitation light. Therefore, the red-shifted part of the fluorescence emission is easily distinguished from scattered light by means of a long-pass filter.

The ZPL linewidth is described by equation 1.1, where  $T_2$  is the total coherence lifetime that is a function of the excited state lifetime  $T_1$ , and pure decoherence lifetime  $T_2^*$ , determined by phonons and other bath fluctuations. At liquid helium temperature (below 5 K) phonon population is weak or negligible so the homogeneous Lorentzian width of ZPL can reach its lifetime limit of a few nanosecond. Compared with the optical frequency, the ZPL transition linewidth is about  $10^7$  times narrower. The tiny ZPL linewidth makes the line extremely sensitive to the smallest changes in the nano-environment of the molecule. Any variation of electric or strain field leads to a detectable shift in the ZPL energy. Therefore, with a careful selection of probe (guest) molecule and transparent matrix (host molecule), the ZPL can be precisely addressed and the desired perturbation (electric field in our case) can be read out.

$$\gamma_{\text{ZPL}} = \frac{1}{\pi T_2} = \frac{1}{2\pi T_1} + \frac{1}{\pi T_2^*} \quad (1.1)$$

In addition to the ground and excited singlet states, organic molecules generally exhibit a third state in between, known as the triplet state. Transitions between singlet and triplet states are known as intersystem crossing (ISC) transitions. ISC transitions are spin-forbidden and the transition rate for the systems studied in this thesis is very low. The branching ratio from the excited singlet to the triplet is typically below  $10^{-6}$ .<sup>39,40</sup> As the molecule stops interacting with the laser when it is in its triplet state, ISC transitions switch the fluorescence emission off and on. The triplet state is also known as the dark state. Although intersystem crossing has interesting applications such as making optical transistors, this topic is not directly relevant to the questions developed in this thesis.

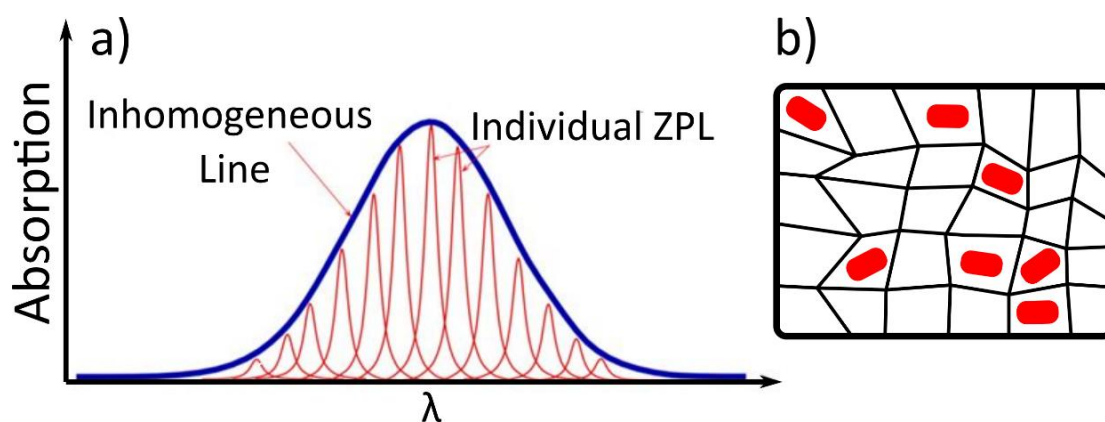


**Figure 1.2:** a) Gaussian lineshape of inhomogeneous broadening produced by superposition of individual ZPL of many inserted molecules in the crystal. b) Schematics of different insertion geometries in a host matrix.

In case of many embedded guest molecules in a host matrix, molecules insert in (slightly) different geometries (Figure 1.2b). Each of the insertion sites is affected by different random defects in the crystal and different local strain and electric fields. In consequence, the homogenous ZPL of each individual molecule is slightly shifted away from the average position. The superposition of all the energies forms a more-or-less Gaussian distribution, centered at the average resonance frequency. This Gaussian distribution is known as an inhomogeneous profile and its width as the inhomogeneous broadening. The inhomogeneous line is sketched in Figure 1.2 beside schematics of different insertion geometries in a crystal.



The other important parameter in SMS measurements is the concentration of guest molecules. The optimum contrast against background in a single-molecule measurement is reached when, in a small frequency interval, only one molecule in the focal volume of the exciting laser is excited resonantly. Other molecules in this focal volume will be too far detuned from the laser to significantly contribute to the fluorescence signal. In other words, the collected fluorescence light from the focal volume will be emitted by one molecule only. The inhomogeneous broadening causes molecules in the focal volume to have different ZPL energies. If the energy difference is more than the ZPL linewidth, the molecules are spectrally selectable. Assuming a focal volume of  $1 \mu\text{m}^3$ , the concentration needs to be a few micromolar at most to excite one molecule per excitation volume and per width of the frequency scan.

## 1.2. SMS experimental setup

Various set-ups have been developed for use in SMS. Exciting molecules by focusing light with a long-focal-length lens and collecting the fluorescence light with a parabolic mirror, focusing and collecting by a parabolic mirror, exciting the molecule through an optical fiber for a crystal attached to its tip and collecting with a parabolic mirror, and even exciting through a tiny pinhole ( $5 \mu\text{m}$ ) and collecting on the other side of the pinhole are some examples of SMS experimental set-ups. In all these methods the major focus has been on increasing the collecting efficiency.

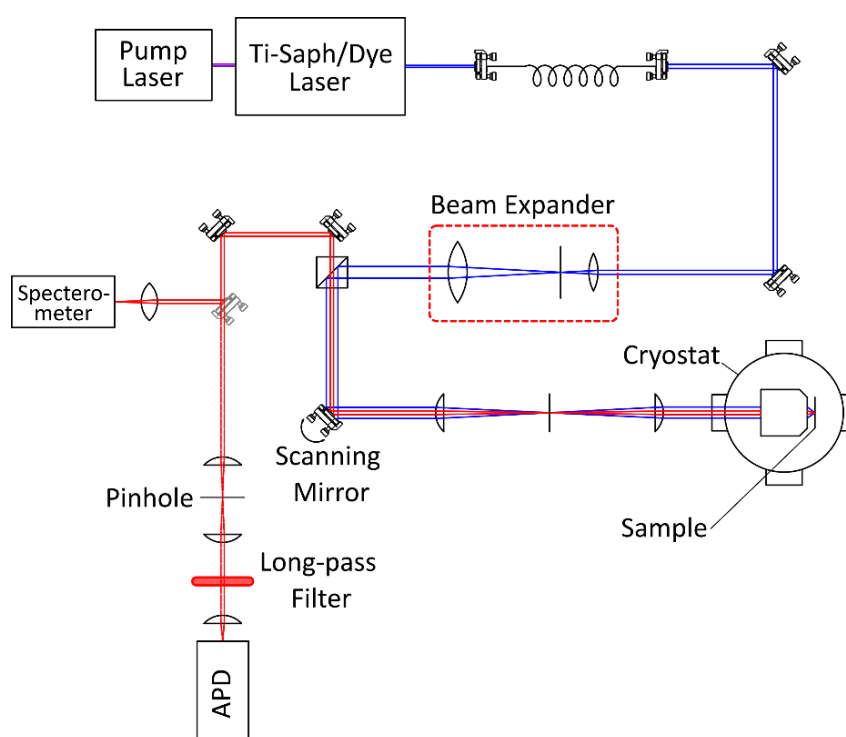


**Figure 1.3:** The schematics of the optical setup for single-molecule spectroscopy.

The development of single-photon detectors has brought the ability to use simpler microscopy methods such as confocal microscopy. In the studies presented in this thesis confocal microscopy (Figure 1.3) was used to detect single molecules and do spectroscopy on them. The excitation light produced by precisely tuneable lasers was sent to the set-up. The excitation light was focused on the sample by a low-temperature objective ( $\text{NA} = 0.7$ ). A galvanometric mirror placed in the focal point of an optical  $4f$  system moves the beam in order to scan the

sample and search for molecules. The fluorescence light was collected via the same objective. The collected light was filtered spatially by a pinhole and spectrally by a long-pass filter. The fluorescence light was sent to either an avalanche photodiode (APD) for absorption measurements or to a spectrometer for emission spectroscopy.

### 1.3. Molecule sensitivity to electric field

The spectral lines of atoms and molecules shift in the presence of an external electric field. This phenomenon is known as Stark effect, named after Johannes Stark, who discovered it in 1913. From the classical point of view, the Stark effect originates from the polarization of charge carriers in the molecules or atoms under the influence of an electric-field perturbation. The new charge distribution introduces changes of energy levels. Figure 1.3 shows schematics of energy levels in a two-level system such as a molecule. The energy levels are different before and after applying the electric field. The different changes in the energy of ground state  $S_0$  and excited state  $S_1$  lead to a shift in absorption energy.

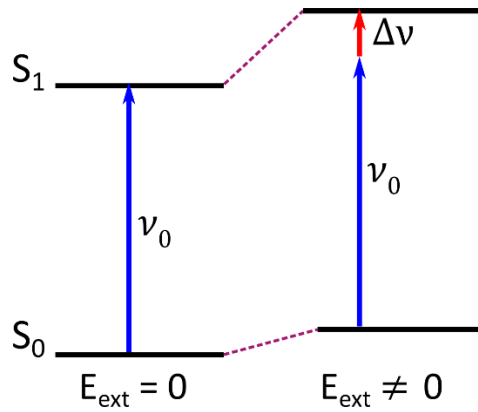


**Figure 1.4:** The schematics of energy level of a two-level system. Changes in the energy level after applying an external electric field lead to a shift in absorption energy  $\nu_1 = \nu_0 + \Delta\nu$ .

In the presence of an external electric field  $\vec{E}_{ext}$ , the energy of a level can be approximated by a Taylor series:

$$\begin{aligned} W(\vec{E}) &= W_1 + W_2 + \dots \\ &= -\vec{\mu}f_l\vec{E}_{ext} - \frac{1}{2}\alpha f_l^2 E_{ext}^2 + \dots, \end{aligned} \quad (1.2)$$

where  $\vec{\mu}$  is the dipole moment of the molecule,  $f_l$  is a local electric field correction factor, and  $\alpha$  is the molecule's polarizability. Using equation (1.2) the Stark shift of a molecule ZPL is given by the equation 1.3:

$$\begin{aligned} h\Delta\nu &= \Delta W_{S_1} - \Delta W_{S_0} \\ &= -\Delta\vec{\mu}f_l \cos\theta E_{ext} - \frac{1}{2}\Delta\alpha f_l^2 E_{ext}^2 + \dots, \end{aligned} \quad (1.3)$$

where  $\theta$  is the angle between the external electric field and the molecule dipole moment. The first part of the equation (1.3) defines the linear Stark shift, and the second element represents the quadratic Stark shift. The linear Stark effect is the result of existence of a dipole moment

in molecules with broken inversion symmetry while the quadratic Stark shift arises from the molecule's polarizability and occurs in centro-symmetric molecules.

The Stark effect is the source of a molecule's sensitivity to the electric field. Small perturbations of the electric field in the environment of a molecule are detectable by measuring the Stark shift of the molecule ZPL. Besides monitoring the electric field in the nano-environment, the Stark effect can be used to tune molecular absorption and emission.<sup>22</sup> Single-molecule spectroscopy provides the ability to measure shifts in the order of 1 MHz for the resonance frequency of a molecule.<sup>7,23</sup> Such a high resolution enables many applications such as learning information about the dipole moment and polarizability of a chromophore and optical tracking quasi-static charges or even single-charge detection.

## 1.4. Outline

In this research, we studied molecular systems with an emphasis on improving their sensitivity to electric fields. We also investigated the operation and realization of a photonic device using an organic single molecule as an interface between elementary charges in an electronic circuit and the laboratory. This device could be used as a quantum coherent information exchange platform between electrons and flying photons.

In Chapter 2, an ultra-sensitive molecular system based on the large aromatic polycyclic hydrocarbon DBT embedded in a 2,3-dibromo-naphthalene crystal was developed. We monitored its response to an external electric field and found it to surpass that of earlier-studied systems, while presenting reliable signals for every single guest DBT molecule in the crystal. In Chapter 3, we report our discovery of a new phenomenon: laser-induced charge generation in three different matrixes and its effect on the excitation spectra of DBT guest molecules. This effect was used to achieve long-lived shifts of the spectral lines of single DBT emitters and to tune them to a frequency of interest. In chapter 4 the working principle of single-electron transistors (SET) is described from a theoretical viewpoint. Then our approach towards optical detection of a single electron by using SETs to control single charge movement is presented. We report our progress in fabrication methods to make SET suitable for the optical study of charge movement and localization in Chapter 5. Finally, the efforts, challenges, and experimental data towards single-charge detection is described in chapter 6.

## References

- (1) Watson, J. H. L. An Effect of Electron Bombardment upon Carbon Black. *Journal of Applied Physics* 1947, 18 (2), 153–161. <https://doi.org/10.1063/1.1697597>.
- (2) Folch, A.; Servat, J.; Esteve, J.; Tejada, J.; Seco, M. High-vacuum versus “Environmental” Electron Beam Deposition. *Journal of Vacuum Science & Technology B: Microelectronics and Nanometer Structures Processing, Measurement, and Phenomena* 1996, 14 (4), 2609–2614. <https://doi.org/10.1116/1.588994>.
- (3) Strahlendorff, T.; Dai, G.; Bergmann, D.; Tutsch, R. Tip Wear and Tip Breakage in High-Speed Atomic Force Microscopes. *Ultramicroscopy* 2019, 201, 28–37. <https://doi.org/10.1016/j.ultramic.2019.03.013>.
- (4) Meli, F.; Küng, A. AFM Investigation on Surface Damage Caused by Mechanical Probing with Small Ruby Spheres. *Meas. Sci. Technol.* 2007, 18 (2), 496–502. <https://doi.org/10.1088/0957-0233/18/2/S24>.
- (5) Komai, K.; Minoshima, K.; Inoue, S. Fracture and Fatigue Behavior of Single Crystal Silicon Microelements and Nanoscopic AFM Damage Evaluation. *Microsystem Technologies* 1998, 5 (1), 30–37. <https://doi.org/10.1007/s005420050137>.
- (6) Ambrose, W. P.; Basché, Th.; Moerner, W. E. Detection and Spectroscopy of Single Pentacene Molecules in a P-terphenyl Crystal by Means of Fluorescence Excitation. *J. Chem. Phys.* 1991, 95 (10), 7150–7163. <https://doi.org/10.1063/1.461392>.
- (7) Hell, S. W.; Wichmann, J. Breaking the Diffraction Resolution Limit by Stimulated Emission: Stimulated-Emission-Depletion Fluorescence Microscopy. *Opt. Lett.*, OL 1994, 19 (11), 780–782. <https://doi.org/10.1364/OL.19.000780>.
- (8) Moerner, W. E. Physical Principles and Methods of Single-Molecule Spectroscopy in Solids. In *Single-Molecule Optical Detection, Imaging and Spectroscopy*; John Wiley & Sons, Ltd, 2007; pp 1–30. <https://doi.org/10.1002/9783527614714.ch1>.
- (9) Orrit, M.; Bernard, J. Single Molecule Spectroscopy. *Mod. Phys. Lett. B* 1991, 05 (11), 747–751. <https://doi.org/10.1142/S0217984991000927>.
- (10) Fleury, L.; Zumbusch, A.; Orrit, M.; Brown, R.; Bernard, J. Spectral Diffusion and Individual Two-Level Systems Probed by Fluorescence of Single Terrylene Molecules in a Polyethylene Matrix. *Journal of Luminescence* 1993, 56 (1), 15–28. [https://doi.org/10.1016/0022-2313\(93\)90049-S](https://doi.org/10.1016/0022-2313(93)90049-S).
- (11) Ambrose, W. P.; Moerner, W. E. Fluorescence Spectroscopy and Spectral Diffusion of Single Impurity Molecules in a Crystal. *Nature* 1991, 349 (6306), 225–227. <https://doi.org/10.1038/349225a0>.

- (12) Zumbusch, A.; Fleury, L.; Brown, R.; Bernard, J.; Orrit, M. Probing Individual Two-Level Systems in a Polymer by Correlation of Single Molecule Fluorescence. *Phys. Rev. Lett.* 1993, 70 (23), 3584–3587. <https://doi.org/10.1103/PhysRevLett.70.3584>.
- (13) Jang, S.; Cao, J.; Silbey, R. J. On the Temperature Dependence of Molecular Line Shapes Due to Linearly Coupled Phonon Bands. *J. Phys. Chem. B* 2002, 106 (33), 8313–8317. <https://doi.org/10.1021/jp0208440>.
- (14) Ashraf, I.; Konrad, A.; Lokstein, H.; Skandary, S.; Metzger, M.; Djouda, J. M.; Maurer, T.; Adam, P. M.; Meixner, A. J.; Brecht, M. Temperature Dependence of Metal-Enhanced Fluorescence of Photosystem I from *Thermosynechococcus Elongatus*. *Nanoscale* 2017, 9 (12), 4196–4204. <https://doi.org/10.1039/C6NR08762K>.
- (15) Verdal, N.; Kelley, A. M. Temperature Dependence of Phonon Sidebands in Line-Narrowed Fluorescence Spectra of Chromophores in Glasses. *J. Chem. Phys.* 2003, 118 (17), 7985–7992. <https://doi.org/10.1063/1.1565318>.
- (16) Ye, J.; Zhao, Y.; Ng, N.; Cao, J. Width of Phonon Sidebands in the Brownian Oscillator Model. *J. Phys. Chem. B* 2009, 113 (17), 5897–5904. <https://doi.org/10.1021/jp809425g>.
- (17) Nicolet, A. A. L.; Bordat, P.; Hofmann, C.; Kol'chenko, M. A.; Kozankiewicz, B.; Brown, R.; Orrit, M. Single Dibenzoterrylene Molecules in an Anthracene Crystal: Main Insertion Sites. *ChemPhysChem* 2007, 8 (13), 1929–1936. <https://doi.org/10.1002/cphc.200700340>.
- (18) Orrit, M.; Bernard, J.; Zumbusch, A.; Personov, R. I. Stark Effect on Single Molecules in a Polymer Matrix. *Chemical Physics Letters* 1992, 196 (6), 595–600. [https://doi.org/10.1016/0009-2614\(92\)86000-8](https://doi.org/10.1016/0009-2614(92)86000-8).
- (19) Tamarat, Ph.; Lounis, B.; Bernard, J.; Orrit, M.; Kummer, S.; Kettner, R.; Mais, S.; Basché, Th. Pump-Probe Experiments with a Single Molecule: Ac-Stark Effect and Nonlinear Optical Response. *Phys. Rev. Lett.* 1995, 75 (8), 1514–1517. <https://doi.org/10.1103/PhysRevLett.75.1514>.
- (20) Brunel, Ch.; Tamarat, Ph.; Lounis, B.; Woehl, J. C.; Orrit, M. Stark Effect on Single Molecules of Dibenzanthanthrene in a Naphthalene Crystal and in a N-Hexadecane Shpol'skii Matrix. *J. Phys. Chem. A* 1999, 103 (14), 2429–2434. <https://doi.org/10.1021/jp983956t>.
- (21) Bordat, P.; Orrit, M.; Brown, R.; Würger, A. The Anomalous Stark Effect of Single Terrylene Molecules in P-Terphenyl Crystals. *Chemical Physics* 2000, 258 (1), 63–72. [https://doi.org/10.1016/S0301-0104\(00\)00173-7](https://doi.org/10.1016/S0301-0104(00)00173-7).
- (22) Orrit, M.; Bernard, J.; Mouhsen, A.; Talon, H.; Möbius, D.; Personov, R. I. Stark Effect in Langmuir—Blodgett Films Studied by Hore-Burning. *Chemical Physics Letters* 1991, 179 (3), 232–236. [https://doi.org/10.1016/0009-2614\(91\)87029-B](https://doi.org/10.1016/0009-2614(91)87029-B).
- (23) Bernard, J.; Talon, H.; Orrit, M.; Möbius, D.; Personov, R. I. Stark Effect in Hole-Burning Spectra of Dye-Doped Langmuir-Blodgett Films. *Thin Solid Films* 1992, 217 (1), 178–186. [https://doi.org/10.1016/0040-6090\(92\)90627-N](https://doi.org/10.1016/0040-6090(92)90627-N).

- (24) Kulzer, F.; Matzke, R.; Bräuchle, C.; Basché, Th. Nonphotochemical Hole Burning Investigated at the Single-Molecule Level: Stark Effect Measurements on the Original and Photoproduct State. *J. Phys. Chem. A* 1999, 103 (14), 2408–2411. <https://doi.org/10.1021/jp9839448>.
- (25) Faez, S.; Verhart, N. R.; Markoulides, M.; Buda, F.; Gourdon, A.; Orrit, M. Design and Synthesis of Aromatic Molecules for Probing Electric Fields at the Nanoscale. *Faraday Discuss.* 2015, 184 (0), 251–262. <https://doi.org/10.1039/C5FD00065C>.
- (26) Davies, G. Approximate Widths of Zero Phonon Lines Broadened by Point Defect Strain Fields. *J. Phys. D: Appl. Phys.* 1971, 4 (9), 1340–1345. <https://doi.org/10.1088/0022-3727/4/9/314>.
- (27) Tian, Y.; Navarro, P.; Orrit, M. Single Molecule as a Local Acoustic Detector for Mechanical Oscillators. *Phys. Rev. Lett.* 2014, 113 (13), 135505. <https://doi.org/10.1103/PhysRevLett.113.135505>.
- (28) Kol'chenko, M. A.; Nicolet, A. A. L.; Galouzis, M. D.; Hofmann, C.; Kozankiewicz, B.; Orrit, M. Single Molecules Detect Ultra-Slow Oscillators in a Molecular Crystal Excited by Ac Voltages. *New J. Phys.* 2009, 11 (2), 023037. <https://doi.org/10.1088/1367-2630/11/2/023037>.
- (29) Müller, A.; Richter, W.; Kador, L. Pressure Effects on Single Molecules of Terrylene in P-Terphenyl. *Chemical Physics Letters* 1995, 241 (5), 547–554. [https://doi.org/10.1016/0009-2614\(95\)00670-Y](https://doi.org/10.1016/0009-2614(95)00670-Y).
- (30) Brunel, C.; Lounis, B.; Tamarat, P.; Orrit, M. Triggered Source of Single Photons Based on Controlled Single Molecule Fluorescence. *Phys. Rev. Lett.* 1999, 83 (14), 2722–2725. <https://doi.org/10.1103/PhysRevLett.83.2722>.
- (31) Lounis, B.; Moerner, W. E. Single Photons on Demand from a Single Molecule at Room Temperature. *Nature* 2000, 407 (6803), 491–493. <https://doi.org/10.1038/35035032>.
- (32) De Martini, F.; Di Giuseppe, G.; Marrocco, M. Single-Mode Generation of Quantum Photon States by Excited Single Molecules in a Microcavity Trap. *Phys. Rev. Lett.* 1996, 76 (6), 900–903. <https://doi.org/10.1103/PhysRevLett.76.900>.
- (33) Itano, W. M.; Bergquist, J. C.; Wineland, D. J. Laser Spectroscopy of Trapped Atomic Ions. *Science* 1987, 237 (4815), 612–617. <https://doi.org/10.1126/science.237.4815.612>.
- (34) Dehmelt, H. G. Radiofrequency Spectroscopy of Stored Ions I: Storage\*\*Part II: Spectroscopy Is Now Scheduled to Appear in Volume V of This Series. In *Advances in Atomic and Molecular Physics*; Bates, D. R., Estermann, I., Eds.; Academic Press, 1968; Vol. 3, pp 53–72. [https://doi.org/10.1016/S0065-2199\(08\)60170-0](https://doi.org/10.1016/S0065-2199(08)60170-0).
- (35) Diedrich, F.; Krause, J.; Rempe, G.; Scully, M. O.; Walther, H. Laser Experiments with Single Atoms as a Test of Basic Physics. *IEEE Journal of Quantum Electronics* 1988, 24 (7), 1314–1319. <https://doi.org/10.1109/3.968>.

(36) Klar, T. A.; Engel, E.; Hell, S. W. Breaking Abbe's Diffraction Resolution Limit in Fluorescence Microscopy with Stimulated Emission Depletion Beams of Various Shapes. *Phys. Rev. E* 2001, 64 (6), 066613.

<https://doi.org/10.1103/PhysRevE.64.066613>.

(37) Hess, S. T.; Girirajan, T. P. K.; Mason, M. D. Ultra-High Resolution Imaging by Fluorescence Photoactivation Localization Microscopy. *Biophysical Journal* 2006, 91 (11), 4258–4272. <https://doi.org/10.1529/biophysj.106.091116>.

(38) Rust, M. J.; Bates, M.; Zhuang, X. Sub-Diffraction-Limit Imaging by Stochastic Optical Reconstruction Microscopy (STORM). *Nature Methods* 2006, 3 (10), 793–796. <https://doi.org/10.1038/nmeth929>.

(39) Verhart, N. R.; Navarro, P.; Faez, S.; Orrit, M. Intersystem Crossing Rates of Single Perylene Molecules in Ortho-Dichlorobenzene. *Phys. Chem. Chem. Phys.* 2016, 18 (26), 17655–17659. <https://doi.org/10.1039/C6CP02678H>.

(40) Lawetz, V.; Orlandi, G.; Siebrand, W. Theory of Intersystem Crossing in Aromatic Hydrocarbons. *J. Chem. Phys.* 1972, 56 (8), 4058–4072. <https://doi.org/10.1063/1.1677816>.





# 2

## **Matrix-induced linear Stark effect of single Dibenzoterrylene molecules in 2,3-Dibromonaphthalene crystal<sup>1</sup>**

Absorption and fluorescence from single molecules can be tuned by applying an external electric field – a phenomenon known as the Stark effect. A linear Stark effect is associated to a lack of centrosymmetry of the guest in the host matrix. Centrosymmetric guests can display a linear Stark effect in disordered matrices, but the response of individual guest molecules is often relatively weak and non-uniform, with a broad distribution of the Stark coefficients. Here we introduce a novel single-molecule host-guest system, dibenzoterrylene (DBT) in 2,3-dibromonaphthalene (DBN) crystal. Fluorescent DBT molecules show excellent spectral stability with a large linear Stark effect, of the order of  $1.5 \text{ GHz/kVcm}^{-1}$ , corresponding to an electric dipole moment change of around 2 D. Remarkably, when the electric field is aligned with the *a* crystal axis, nearly all DBT molecules show either positive or negative Stark shifts with similar absolute values. These results are consistent with quantum chemistry calculations. Those indicate that DBT substitutes three DBN molecules along the *a*-axis, giving rise to eight equivalent embedding sites, related by the three glide planes of the orthorhombic crystal. The static dipole moment of DBT molecules is created by host-induced breaking of the inversion symmetry. This new host-guest system is promising for applications that require a high sensitivity of fluorescent emitters to electric fields, for example to probe weak electric fields.

---

1-This Chapter has been published in Chemphyschem 2019 Jan 7;20(1):55-61.

## 2.1. Introduction

Fluorescent polycyclic aromatic hydrocarbons (PAHs) are recently receiving increasing attention as bright and photostable single-photon emitters that can be integrated into on-chip quantum electronic devices.<sup>1-4</sup> Single-molecule fluorescence spectroscopy of PAHs at cryogenic temperatures has been used as a highly sensitive technique to optically probe the interactions of individual emitters with their local environments.<sup>5-7</sup> The spectral position of the narrow optical transitions (typical linewidth 30–50 MHz) is very sensitive to external perturbations, for example from electric fields. The shift in the spectral transition frequency between the ground and the excited state of a molecule in an electric field is commonly known as the Stark effect. Typically, the frequency shift has both linear and quadratic Stark contributions which depend on the change in electric dipole moment and in polarizability tensor, respectively, between the excited and ground states.<sup>8,9</sup>

Several host-guest systems with different contributions of the linear and quadratic Stark effects have been reported in the literature.<sup>10-15</sup> These studies mostly concentrated on centrosymmetric fluorescent emitters that should exhibit a quadratic Stark effect only. However, the central symmetry of the guest molecules is often broken in disordered host matrices, such as polymers, making it possible to observe the linear Stark effect.<sup>9</sup>

For terrylene in *p*-terphenyl, flipping of a host phenyl ring close to the guest leads to switching from a centrosymmetric to a non-centrosymmetric insertion, with distinct quadratic and linear dependences.<sup>11,16</sup> Nevertheless, a broad distribution of the linear Stark coefficients (often centered around zero) and low linear Stark coefficients for the majority of emitters still remain serious experimental limitations. For applications where the transition frequency should be tuned by an applied electric field, it is highly desirable to have a large fraction of single emitters responding uniformly (i.e. with similar Stark shifts) to the applied electric field. Furthermore, as the quadratic Stark effect is very weak in nature, the large linear Stark effect is advantageous. Such probes would enable faster and more reproducible tuning of single-photon emission, as well as a higher sensitivity of single molecules to small perturbations by local electric fields, including the optical detection of single electrons.<sup>17-19</sup>

Many of the probe molecules in single-molecule spectroscopy, such as dibenzoterrylene (DBT),<sup>20</sup> are centrosymmetric, which means that they do not intrinsically possess a permanent electric dipole moment. DBT has been recently a popular choice for fluorescent studies due to its excellent photophysical properties, including high brightness, photostability, single-emitter coupling to waveguides and to on-chip cavities,<sup>21-23</sup> and single-photon emission.<sup>24</sup>

A tunable single-molecule emission of DBT in the electric field can further facilitate quantum manipulation and integration of this molecule into molecular electronic quantum devices. Because they are easily synthesized, chemically identical and reproducible, single-molecule-based quantum emitters offer an appealing alternative to more frequently used single-photon sources, such as color centers in diamond, quantum dots, and other solid-state systems.<sup>25-27</sup> However, the well-studied and the most used molecular-based system, DBT in anthracene,

mainly exhibits quadratic Stark effect with very small linear coefficients (due to crystal defects) that are distributed around zero.<sup>28</sup> One strategy to induce a permanent electric dipole of the guest molecule is by the chemical synthesis of an asymmetric dye molecule.<sup>29</sup> Another strategy is to insert the symmetric guest molecule into a crystal built from asymmetric host molecules. This latter strategy is not risk-free, as the insertion of the guest into the host molecular crystal should not induce further defects nor any significant spectral diffusion.<sup>30</sup> The resulting doped crystals ideally should preserve the desirable spectral properties of the low-temperature fluorescent probe, such as narrow optical transitions, high spectral stability, and low spectral diffusion. Recent experimental and quantum chemistry studies on terrylene in di-substituted naphthalenes, such as 2,3-dichloronaphthalene and 2,3-dibromonaphthalene (DBN for short), have shown that these dihalogenated compounds can be suitable hosts for fluorescent PAH molecules.<sup>31,32</sup> Here we show that the electro-negativity of halogen atoms, combined with the herring-bone crystalline structure of the host, is able to induce large electric dipoles on a centrosymmetric molecule such as dibenzoterrylene. We introduce a novel host-guest system based on DBT in DBN and report for the first time on a large linear Stark shift homogeneously affecting all fluorescent molecules by matrix-induced symmetry breaking.

## 2.2. Experimental section

### 2.2.1. Crystal growth

DBN used in this work was purchased from Ark Pharm Inc. High-quality single crystals of zone-refined DBN doped with DBT molecules were obtained by co-sublimation at  $\sim 0.2$  (*bar*) of argon gas. To prevent perturbations from the convection flow in the sublimation chamber, the sublimator was kept horizontal during growth. The sublimation-grown crystals develop along the (*a. b*) plane as thin mm-sized plates or flakes, with a typical thickness of few microns along the *c*-axis.

### 2.2.2. Optical microscopy

A well-defined single crystal free of visible defects was carefully transferred to a silica substrate on which interdigitated gold electrodes had been deposited by lithography (see Figure 2.1.b). The electrodes were 200 *nm* thick and were separated by a distance of 10  $\mu\text{m}$ . The external electric field was varied through the voltage applied to the electrodes. The crystals were placed on the chip at the desired angle between the electric field and the crystallographic *a*-axis, determined by separately measuring the orientation of the transition dipole moment of DBT impurities. To this aim, the crystal was placed on a rotating stage and excited at normal incidence by a 756 *nm* laser beam with linear polarization in the (*a. b*)-plane of the crystal. Fluorescence images were recorded with a sensitive CMOS camera (Hamamatsu, Orca Flash 4.0) while rotating the stage.

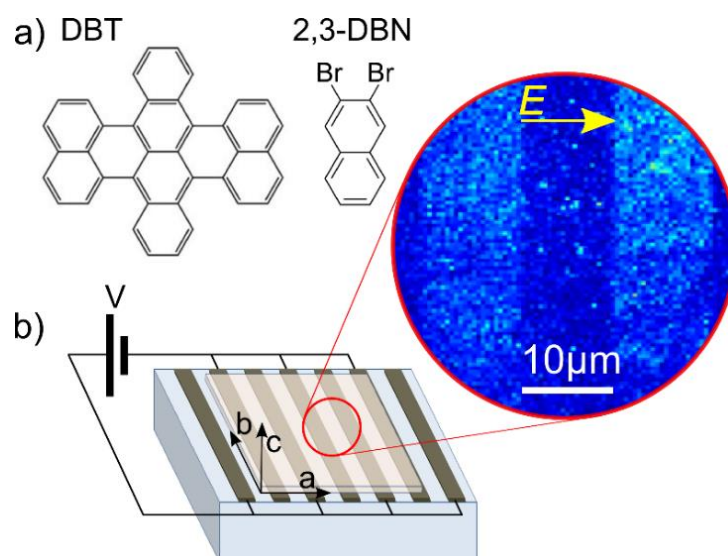


**Figure 2.1.** a) Molecular structures of DBT and 2,3-DBrN. b) Schematic of the chip for Stark effect measurements with a crystal placed on the top of electrodes. The axes designate the crystallographic orientation of the crystal in the plane of electrodes. Zoom-in shows a confocal fluorescence microscopy image of the crystal containing fluorescent DBT molecules. The electrodes are visible through stronger light scattering.

All single-molecule measurements were done at 1.2 K in a home-built liquid-helium bath cryostat. Single DBT molecules were excited by a tunable continuous wave Ti:Sapphire laser (Coherent, 899–21) with a 2 MHz bandwidth. The sample was scanned in a confocal arrangement using a scanning mirror (Newport, FSM-300-01). The fluorescence light was collected by a cryogenic objective (Microthek,  $NA = 0.8$ ) and detected by a single-photon counting module (Excelitas Single Photon Counting Module, SPCM-AQRH-16) with a set of filters (Chroma HQ760LP and Semrock FF02-809/81) in the detection path.

Bulk fluorescence excitation and emission spectra were obtained at 5K using a Ti:Sapphire laser (Coherent, Mira-HP). For the detection path, a scanning monochromator (McPherson, 207) and a photo-multiplier (EMI, 9659) operating in photon-counting mode were used. The fluorescence excitation spectrum was obtained by scanning the laser while the monochromator was set to  $773.6\text{ nm}$  (a band pass filter Chroma D780/20 was used in the detection path). For the fluorescence emission spectrum, the laser was in resonance with the vibronic component located at  $740.3\text{ nm}$  (with Semrock FF01-785/62 filter in the detection path).

### 2.2.3. Quantum chemistry calculations

All calculations in this work were done with the Gaussian 09 package.<sup>33</sup> Like in our previous works<sup>32,34</sup> optimization of the geometry of DBT placed inside the rigid crystalline lattice was done with the aid of the ONIOM(B3LYP/6-31G(d,p):UFF) procedure, where B3LYP/6-31G(d,p) is used for the DBT molecule (as so-called high layer in the division of the calculated system) and UFF method for the DBN lattice (low layer). In our calculations we consider a crystal composed by  $3 \times 2 \times 2$  unit cells (i.e. 96 molecules of DBN) with geometry based on the orthorhombic  $P_{bca}$  unit cell of DBN crystal, as described in previously published

crystallographic data.<sup>32,35</sup> A DBT molecule replaces three molecules of DBN aligned along the crystal  $a$ -axis. Calculations were strongly limited by the requirements of the computational memory and time, especially for the electronically excited states. Therefore, the simplest TD B3LYP/STO-3G method was used for calculations of the dipole moments of both, the whole system and the individual components.

## 2.3. Results

### 2.3.1. Photophysical properties of the system

The molecular structures of DBT and DBN are shown in Figure 2.1.a. A platelet-like crystal of DBT/DBN was optically contacted to a custom-made glass chip with electrodes (Figure 2.1.b). First, we studied the bulk photophysical properties of the DBT/DBN system. Figure 2.1.a displays the bulk fluorescence excitation (blue curve) and emission (red curve) spectra of DBT/DBN. A single, inhomogeneously broadened line at about  $756.6 \text{ nm}$  is found at the same wavelength in the excitation and fluorescence spectra. Thus, it indicates a purely electronic zero-phonon line (ZPL) of this system, and it was the only one we could find. The inhomogeneous linewidth of the ZPL is  $\sim 5 \text{ cm}^{-1}$ . The absence of other resonant absorption and fluorescence peaks points towards a *single spectroscopic site* in this host-guest system.

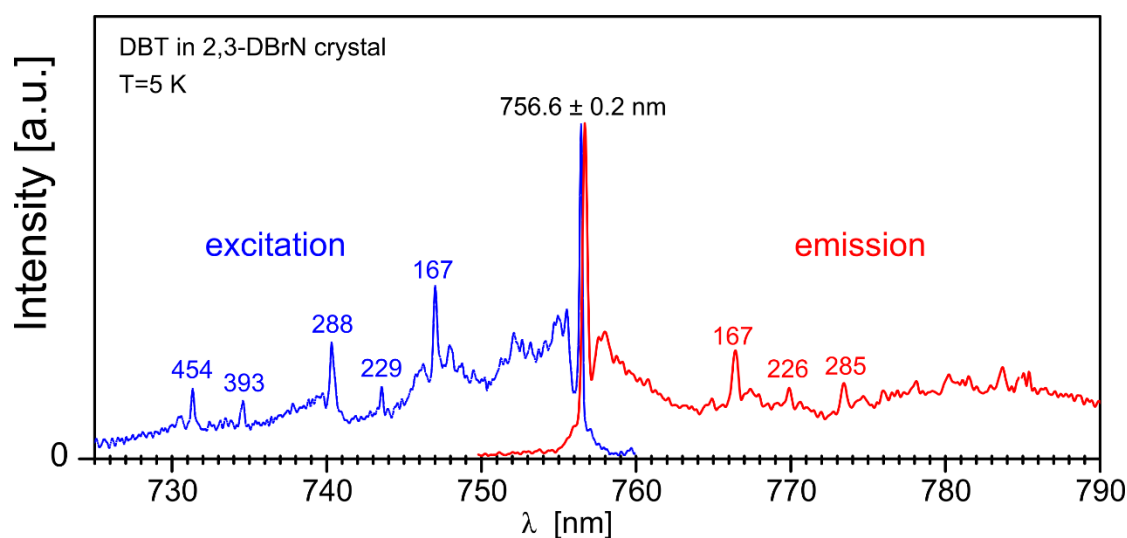


**Figure 2.2.** Fluorescence excitation spectrum (blue) with fluorescence detection at wavelengths longer than  $773.6 \text{ nm}$ , and fluorescence spectrum (red) excited at  $740.3 \text{ nm}$ . The number above each vibronic line indicates the vibration frequency (shift from the ZPL) in reciprocal centimeters ( $\text{cm}^{-1}$ ).

For the cryogenic single-molecule experiments, the laser was tuned at  $756.4 \text{ nm}$  to excite individual DBT molecules from the ground vibronic level of the ground state ( $|g, \nu = 0\rangle$ ) to the ground vibronic level of the excited electronic state ( $|e, \nu = 0\rangle$ ). In the following, we will use the static dipole moment vectors  $\mu_g$  and  $\mu_e$  in the ground and excited state, respectively, as well as their difference  $\Delta\mu = \mu_e - \mu_g$ . The transition matrix element between these two states is another vector, noted  $\mu_{eg}$ . The studied system also provided a conveniently large number of single emitters within a  $3 \text{ GHz}$  single frequency scan.

Figure 2.3.a shows the excitation spectra of more than 20 DBT molecules recorded over 250 s of repetitive frequency scans. Each horizontal line indicates an individual DBT molecule within the focal spot of the laser beam, showing excellent spectral stability in time. No significant frequency jumps or spectral diffusion have been observed, even during longer measurements. Similarly, we did not observe significant broadening of the homogeneous linewidth, as shown for a single molecule in Figure 2.3.b. The full width at half-maximum (FWHM) was extrapolated from the measured saturation curves of 30 molecules (Figure 2.3.c). The average FWHM of  $37 \pm 4$  MHz agrees well with the observed fluorescence lifetime of DBT in DBN, 4.84 ns (see Figure S2.1 in the Supporting Information). The number of detected counts at saturation was around 80,000 cps for most molecules, a typical detection rate for well-oriented DBT molecules.<sup>20</sup> These measurements already indicate very favorable photophysical properties of the DBT/DBN system for single-molecule spectroscopy.

We point out here that the size of the host halogen atoms most likely also plays a role in stabilizing the system. We performed similar experiments with 2,3-dichloronaphthalene as host, but DBT molecules in this system turned out to be significantly less photostable. The introduction of halogen atoms to the aromatic host could be a common strategy to induce a linear Stark shift. Türschmann et al. have reported linear Stark effect on DBT in *para*-dichlorobenzene, although the authors noted that different individual DBT molecules in this system respond differently to the electric field.<sup>36</sup>

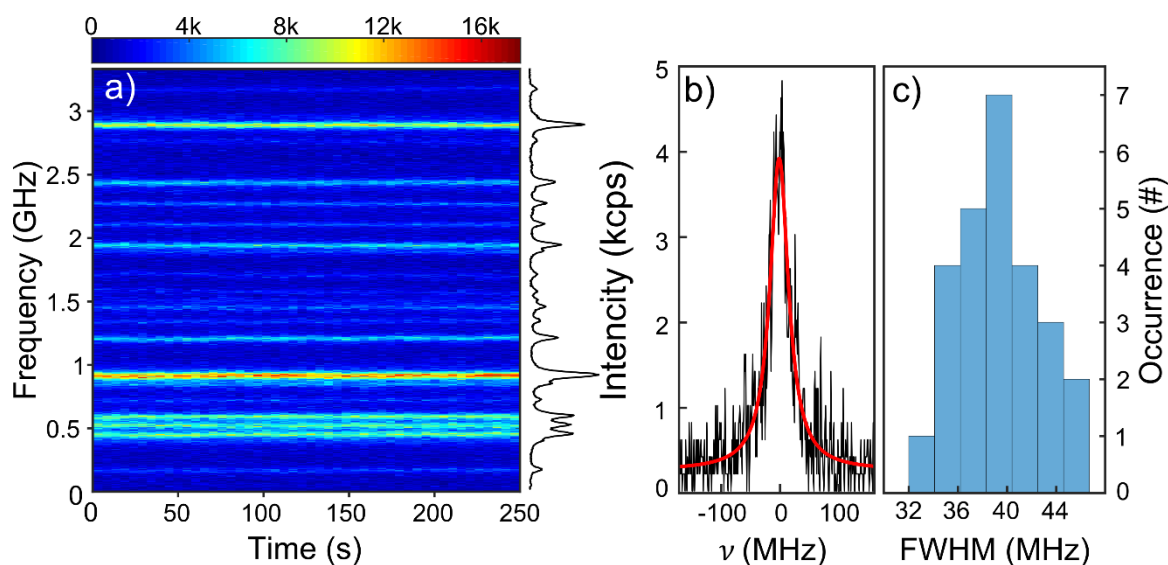


**Figure 2.3.** a) Time traces of more than 20 single molecules measured at 756.4 nm. The color scale units are counts per second. b) Single DBT molecule ZPL spectrum fitted with the Lorentzian profile. c) Histogram of the single-molecule homogeneous linewidth.

### 2.3.2. Stark effect experiments

The Stark shift of single-molecule ZPLs was measured by applying a variable voltage on the electrodes. In all Stark measurements the applied electric field varied from  $-1$  kV/cm to  $1$  kV/cm while the laser was scanned for each voltage applied. The uniformity of the electric field was ensured by measuring molecules at the distance of  $5 \pm 1$   $\mu$ m from the

edges of the electrodes and within the same focal plane as the electrodes (Figure 2.1.b). Figure 2.4.a presents the Stark shift of more than 20 DBT molecules when the  $a$ -axis of the crystal was aligned along the applied electric field. The large linear Stark shifts in the order of  $1.5 \text{ GHz}/\text{kVcm}^{-1}$  proved that the strategy of inducing static dipole moments in the guest molecules by the use of asymmetric host molecules is effective. Remarkably, all molecules within the scanned confocal volume exhibited similar absolute values of the Stark coefficients, as shown in Figure 2.4.b. We find two distinct sub-populations of molecules, but with identical absolute values of their Stark shift ( $1.4 \text{ GHz}/\text{kVcm}^{-1}$ ).

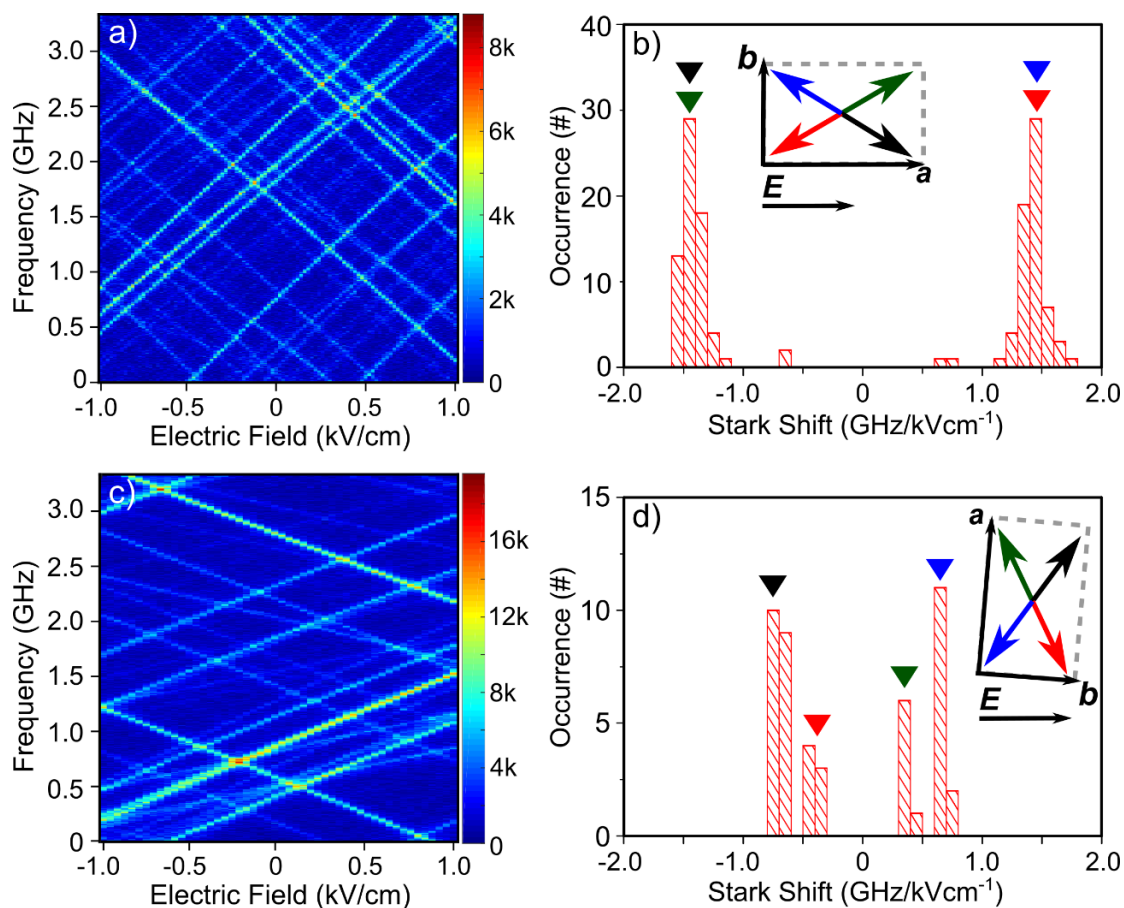


**Figure 2.4.** Stark shifts of DBT single molecules in an electric field nearly parallel or perpendicular to the  $a$ -axis. a) Electric field nearly parallel ( $2 \pm 5^\circ$ ) to the  $a$ -axis, and b) corresponding histogram of the Stark shift. c) Electric field nearly perpendicular ( $85 \pm 5^\circ$ ) to the  $a$ -axis, and d) corresponding histogram of the Stark shift. The color scales in (a) and (c) are in counts per second. Insets in (b) and (d) indicate the orientation of the crystal (and 4 molecular dipoles) in the ( $a,b$ ) plane with respect to the electric field,  $E$ . The color-coded triangles indicate the values of the Stark shifts for the corresponding four dipoles.

The opposite slopes of the two sub-populations indicate that the electric dipole difference vector,  $\Delta\mu$ , can have either a positive or a negative projection onto the applied electric field, directed along the  $a$ -axis. Previously, large linear Stark shifts of similar magnitudes were observed on single molecules of terylene in amorphous polyethylene (up to  $2 \text{ GHz}/\text{kVcm}^{-1}$ ).<sup>9</sup> In crystalline hydrocarbon matrices, such as naphthalene, p-terphenyl and n-hexadecane, the Stark shifts of terylene and dibenzanthrene are comparatively weak, with the highest recorded linear coefficients in the order of  $200 \text{ MHz}/\text{kVcm}^{-1}$ .<sup>10,11,13</sup> In

stark contrast to these previous studies, almost all molecules in our system exhibit equally large linear Stark shifts, without any non-responsive molecules. Such a large and homogenous response of all emitters to an external electric field has never been reported previously.

Further inspection of the crystal orientation in the electric field shows that the magnitudes of the Stark shift depend on the exact alignment of the crystal in the electric field. As expected, the minimum in the Stark response is reached when the crystallographic  $a$ -axis is nearly perpendicular to the electric field (Figure 2.4.c). For an arbitrary orientation of the crystal with respect to the electrodes, we found four distinct sub-populations of molecules with different Stark shifts, and two-by-two opposite values. For example, for an angle  $\varphi \sim 85^\circ$  between the electric field and the  $a$ -axis, we find Stark shifts centered around  $\pm 0.4$  and  $\pm 0.7 \text{ GHz/kVcm}^{-1}$ , as shown in Figure 2.4.d. This result suggests at least 4 distinct dipole orientations in the electric field, related to each other by the symmetry on the crystal. Interestingly, the maximum value of the Stark coefficient ( $1.56 \text{ GHz/kVcm}^{-1}$ ) is reached for a crystal with an angle  $\varphi$  of  $20^\circ$  between the  $a$ -axis and the electric field (Figure S2.3). The measured Stark coefficient maximum translates into the electric dipole moment change of 2.1 D, if a local-field correction factor of 1.5 is applied.

We can now consider our results as a special case of four dipoles in an electric field  $E$  situated in the (a, b) plane, which is our experimental arrangement. The linear Stark shift is proportional to a scalar product of  $\Delta\mu$  and  $E$ , i.e.  $h\Delta\nu = -\Delta\mu \cdot E$ . Here we consider the effective electric field which includes the local-field correction. As discussed later, the symmetries of the host crystal give rise to four possible projections of the dipole moment onto the field, which can be expressed using the angle  $\varphi$  between the electric field and the crystal's  $a$ -axis, as well as the angle  $\theta$  between the  $a$ -axis and the  $\Delta\mu$  a particular molecule taken as a reference (see Figure 2.5). Note that  $\theta$  is an intrinsic property of the crystal, whereas we can give arbitrary values by orienting the crystal with respect to the electrodes. By using the two angles  $\theta$  and  $\varphi$ , the Stark shift will be different for each of the four *differently oriented* guest dipoles. The Stark shift of the reference molecule will then be  $h\nu = -\Delta\mu_{max} \cdot E \cos(\varphi + \theta)$  or expressed as the frequency change,  $\Delta\nu = -\Delta\nu_{max} \cos(\varphi + \theta)$ . For the three other molecules deduced by mirror symmetries on glide planes (a,c) and (b,c), the shifts are:  $\Delta V = \Delta V_{max} \cos(\varphi - \theta)$ ,  $\Delta V = -\Delta V_{max} \cos(\varphi + \theta)$ ,  $\Delta V = -\Delta V_{max} \cos(\varphi - \theta)$  corresponding to four possible orientations of the dipole moments in the (a,b) plane.



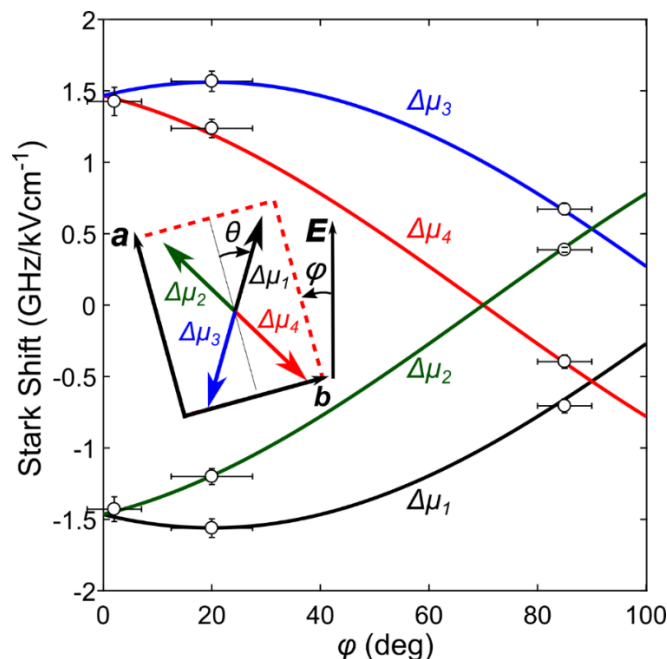


**Figure 2.5:** Angle-dependent Stark shift as a function of the angle,  $\varphi$ , between the  $a$  crystallographic axis and the electric field. The Stark shift is calculated for four electric dipoles (rotated  $-\theta + \varphi$ ,  $\theta + \varphi$ ,  $\pi - \theta + \varphi$ ,  $\pi + \theta + \varphi$  and compared to the experimental data (hollow circles). The simulated values are determined for the maximum of the Stark shift  $1.56 \pm 0.06 \text{ GHz/kVcm}^{-1}$  and  $\theta = 20^\circ$ . The inset illustrates the orientation of the four dipoles used in calculation;  $a$  and  $b$  axes, electric field vector  $E$ , as well as angles  $\theta$  and  $\varphi$  are shown.

Figure 2.5 shows the dependence of the Stark shift on the tilt angle  $\varphi$  of the crystal's  $a$ -axis with respect to the electric field. The calculated Stark shift as a function of  $\varphi$  (solid lines) coincided with the experimental data (circles) for  $\theta = 20 \pm 5^\circ$ . Other values of  $\theta$  could not match our results, as shown in Figure S2.4. The results also show that the four values of the Stark shift should merge into two values when the crystal is perfectly aligned with the electric field ( $\varphi = 0^\circ$ ), which is the case for the measurement shown in Figure 2.4.a. The maximum of the Stark shift will be, however, recorded for the alignment angle  $\varphi = -\theta$ , when  $E$  coincides with one of the four projections of  $\Delta\mu$  vectors. These experimental findings will be generalized for an arbitrary electric field in the Discussion section.

### 2.3.3. Quantum chemistry calculations

To understand the origin of the large Stark shift of DBT, we have performed quantum chemistry calculations looking for the structure of a DBT molecule and its dipole moments, which may be affected by interaction with the surrounding DBN host molecules. In the calculations, a guest DBT molecule was embedded in a  $P_{bca}$  orthorhombic unit cell of DBN (Figure S2.5) by replacing 3 host molecules along the crystal  $a$ -axis and was surrounded by 96 DBN molecules (12 elementary cells). The result of ONIOM (B3LYP/6-31G (d, p): UFF) optimization is shown in Figure 2.6.a (for coordinates of the optimized DBT see Tab. S2.1). It is visible that the embedded DBT molecule loses the  $C_{2h}$  symmetry characterizing the isolated DBT.<sup>37</sup>

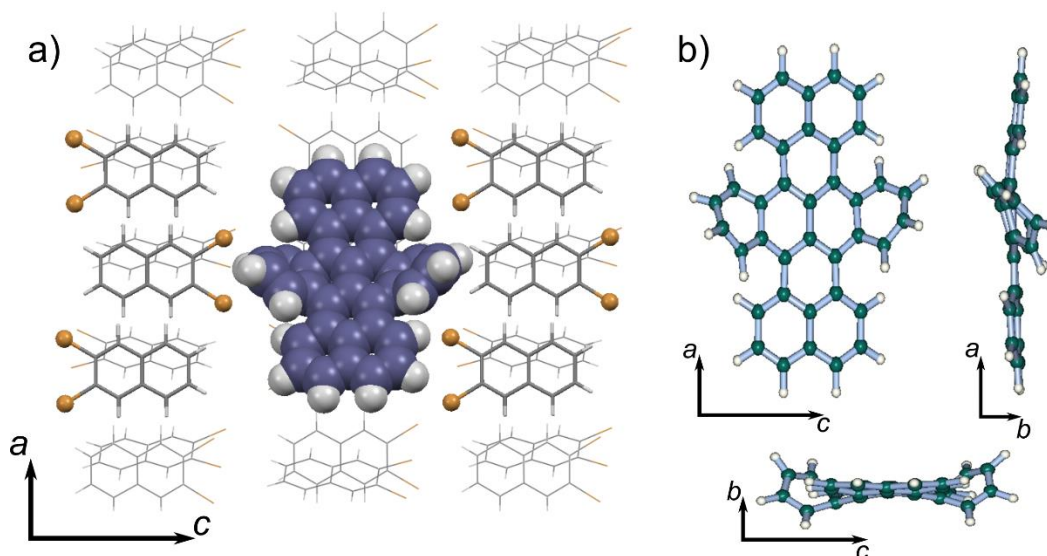


**Figure 2.6:** a) Insertion site, visualized in the (*a,c*) plane. The DBT molecule is represented in space-fill molecular model, replacing 3 host molecules; the adjacent DBN molecules (along *a*-axis) are highlighted as capped sticks. Bromine atoms (golden balls) are highlighted for convenience. b) Host-induced distortion and bending of the guest DBT molecule visualized in all three planes. For more detailed crystallographic information about the unit cell of the host matrix, see Figure S2.5.

Figure 2.6.b illustrates the resulting large distortion of the terrylene core and the tetracene unit of DBT. Structural changes of the DBT molecule are accompanied by changes of the static dipole moments in the ground and excited states. A free-space DBT molecule does not possess any permanent dipole moment. The total dipole moment of each unit cell of the DBN crystal (containing 8 DBN molecules) is also zero, although each of the DBN molecules has a non-zero dipole moment (1.48 D). Creating an empty cavity in the DBN crystal by removing three DBN molecules along the axis *a* results in the appearance of a dipole moment of 1.8 D, directed mainly along the *a* crystal axis (see Table S2.3). The asymmetric distribution of the electron density at the DBT molecule (with the DBN crystal optimized structure) has relatively large components of the electric dipole moment along the two crystal axes (*a* and *c*), as shown in Table S2.2. The total dipole moment of the whole system, i.e. DBT in DBN crystal, after optimization of DBT structure is 2.46 D (Table S2.3). The difference between dipole moment vectors of the crystal with the empty cavity and with the cavity filled with DBT is 1.53 D. This value is greater than the dipole moment calculated for the isolated DBT molecule in its crystal-deformed geometry, 0.69 D (Table S2.2). Thus, the interaction of DBT (in the electronic ground state) with the surrounding DBN molecules leads to a significant increase of the dipole moment of the whole system.

The isolated DBT molecule in the distorted geometry optimized in the DBN crystal also possesses a nonzero permanent dipole moment in the excited singlet  $S_1$  state, equal 0.38 D according to our calculations (Table S2.2). The calculated difference between dipole moments in excited  $S_1$  and ground  $S_0$  electronic states is  $|\Delta\mu| = 0.47D$ . The transition moment  $\mu_{eg}$  reaches 7.8 D and is oriented almost perfectly along the molecule's long axis (Table S2.2), as found experimentally. An interesting observation is that the vector

difference  $\Delta\mu$  responsible for the large Stark effect, is directed mainly along the transition dipole moment  $\mu_{eg}$  (and thus along the  $a$ -axis of the host crystal).

**Table 1.** Components along the crystal axes of the transition dipole moment  $\mu_{eg}$  and dipole moments  $\mu_g$ ,  $\mu_e$ ,  $\Delta\mu = \mu_e - \mu_g$  of DBT obtained for the simulation cell with 28 host molecules (see Table S2.4 for details). All values are in D (where  $1D = 3.34 \cdot 10^{-30} Cm$ );  $a$ -,  $b$ -, and  $c$ -axis, represent the projections of the calculated vectors on the crystallographic axes of the crystal, whereas  $|\mu|$  represents the modulus of the corresponding vector.

	$a$ -axis	$b$ -axis	$c$ -axis	$ \mu $
$\mu_{eg}$	8.0150	0.3820	0.4592	8.0372
$\mu_g$	-0.6149	-0.6587	-7.7383	7.7906
$\mu_e$	0.1438	-0.7913	-8.4195	8.4579
$\mu_e - \mu_g$	0.7587	-0.1326	-0.6812	1.0282

Unfortunately, the size of the system required to calculate the dipole moment in the electronic excited  $S_1$  state must be much smaller than for the ground  $S_0$  state. Therefore, the  $s_1$  calculations were performed for a limited number of 28 surrounding host molecules, with the DBT geometry optimized in the ground state. Summarizing these results in Table 1 we may conclude that the dipole moment in the excited  $S_1$  state increased by about 1 D, which is larger than the value calculated for the isolated DBT in the optimized geometry. Similar results were obtained with smaller simulation cells (Supporting Information Table S2.4). The projection of  $\Delta\mu$  onto the crystal  $a$ -axis is found to be 0.76 D, with an angle of  $10^\circ$  between the  $a$ -axis and  $\Delta\mu$  (see Table 1). This value matches reasonably well with  $\theta = 20^\circ$  derived from the experiment.

## 2.4. Discussion

Before discussing possible DBT insertions in the DBN crystal, let us briefly recall the structure of this crystal. DBN crystallizes in the orthorhombic  $P_{bca}$  system, which is characterized by three glide planes, with glide mirrors (a,b), (b,c), (c,a), and a center of symmetry at the center of the unit cell. The unit cell contains 8 molecules arranged in a herring-bone pattern. These molecules are all related by mirror symmetries in the glide planes, as illustrated in Figure S2.5. The 8 molecules in the unit cell thus cover all the 8 possible images of any particular molecule in the 3 glide planes (i.e., after suitable translations, see Figure S2.5), in the 3 screw axis rotations, which are products of two glide mirror symmetries, and in the inversion. Embedding a DBT molecule in this crystal requires removing 3 host molecules. Quantum chemistry calculations indicate that the most favorable way to do this is to replace 3 DBN molecules along the crystallographic  $a$ -axis (Figure 2.6.a). Indeed, this is in accordance with the experimental finding that the DBT transition dipole moment, directed along the long DBT axis, is roughly aligned along the  $a$ -axis of the

crystal. Taking the crystal structure into account, we find that the substitution can be realized in 8 different manners, taking each molecule in the DBN unit cell as the starting point for the substitution of 3 DBN molecules along the  $a$ -axis. Moreover, these 8 distinct insertion sites are all related by the same mirror symmetries in the glide planes as the original host molecules. Therefore, they are completely equivalent from a spectroscopic point of view, which nicely explains why only one single spectroscopic site is observed (Figure 2.2).

Let us now consider any vector  $V$  (components  $V_a, V_b, V_c$  in the crystal's orthonormalized reference frame) related to a molecule (1) in the DBN unit cell (see Figure S.5). The associated vectors for each of the seven other molecules will be deduced from  $V$  through mirror symmetries and their products, leading to 8 vectors with components  $\pm V_a, \pm V_b, \pm V_c$ . In particular, the Stark effect is determined by the dipole moment change  $\Delta\mu$  of molecule (1). The symmetry of the crystal thus gives rise to 8 possible dipole moment changes,  $\Delta\mu_i(\pm\Delta\mu_a, \pm\Delta\mu_b, \pm\Delta\mu_c)$ . To each possible DBT insertion site we can thus associate one of these 8  $\Delta\mu_i$  vectors. Note, however, that these 8 vectors all have equal magnitudes of  $|\Delta\mu|$ . Upon application of an external electric field  $E$  with components  $(E_a, E_b, E_c)$ , we obtain 8 possible linear Stark effects with the shifts:  $h\Delta\nu = (\pm\Delta\mu_a E_a \pm \Delta\mu_b E_b \pm \Delta\mu_c E_c)$ , i. e., 8 sub-populations of molecules with different Stark shifts. In the special case of a field situated in one of the planes, e. g. (a, b),  $E_c = 0$  and we find only four sub-populations,  $h\Delta\nu = -(\pm\Delta\mu_a E_a \pm \Delta\mu_b E_b)$ . Similarly, for a field oriented along one of the crystal axes, e. g. the  $a$ -axis, we find only two sub-populations with shifts  $h\Delta\nu = \mp\Delta\mu_a$ . The cases of two and four distinct sub-populations are observed experimentally (see Figure 2.4). Finally, we note that, according to calculations,  $\Delta\mu$  can have a significant component along the  $c$  axis, but the effective electric field component  $E_c$  should be negligible in our experiment. A small angle between the crystal and the chip surface ( $1-5^\circ$ ), or a small displacement of the molecule with respect to the electrode plane, can account for the deviations in the order of  $50-100 \text{ MHz/kVcm}^{-1}$ . Because of the inhomogeneous broadening, these values are too small to be unambiguously determined experimentally.

## 2.5. Conclusions

We presented a new host-guest system for single-molecule fluorescence spectroscopy based on DBT in 2,3-dibromonaphthalene (DBN). The system is the first successful demonstration of a strategy to use an asymmetric and polar host matrix to induce large static dipole moments in otherwise centrosymmetric guest molecules. This strategy leads to a large linear Stark effect in the order of  $1.5 \text{ GHz/kVcm}^{-1}$  for DBT in DBN. DBT molecules in the system behave remarkably well—they all respond similarly to the applied electric field, showing at the same time excellent spectral stability and narrow single-molecule resonances of about  $40 \text{ MHz}$  width. Our results were further complemented by quantum chemistry calculations, which indicated host-induced symmetry breaking in DBT molecules. By considering the symmetry of the host crystal, we have explained why embedding of DBT in DBN crystal, while exhibiting a single spectroscopic site, can lead to up to 8 different Stark coefficients in an applied electric field with arbitrary orientation. This system is an excellent candidate for single-molecule spectroscopy of DBT—an increasingly popular single-photon

emitter. In addition, the large and homogeneous linear Stark response of the probe could be used for sensing local electric fields and for a precise tuning of the single-molecule emission wavelength over a large spectral range.

## 2.6. Supporting information

compare to the extrapolated linewidth of single molecules at low temperature and low power, we measured ensemble fluorescence decays of DBT in DBN crystals at 5 K, using a confocal fluorescence microscope. The extracted lifetime, 4.84 ns, corresponds to a life-time limited linewidth of 33 MHz, in good agreement with the measurements (36-40 MHz, see Figure 2.3.c).

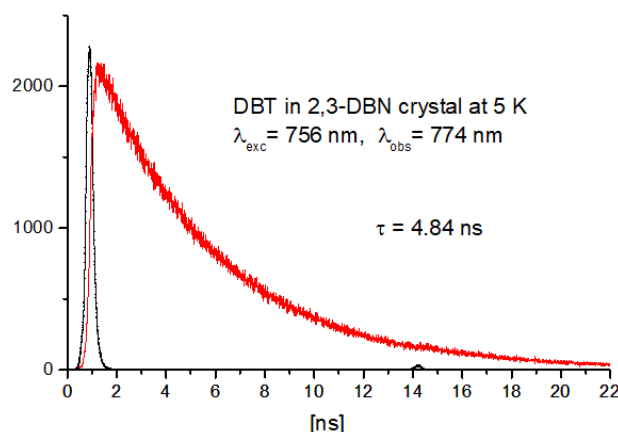


**Figure S2.1:** Fluorescence lifetime decay measurement of DBT in 2,3-DBN (red line), as measured for an ensemble at 5 K using a confocal fluorescence microscope. The instrument response function is shown in black. The fluorescence emission of DBT was excited at 756 nm and detected using a long-pass filter at 774 nm and an SPCM-AQR-14 photon counting module.

### 2.6.1. Crystal Alignment for the Stark Experiment

A DBT/DBN single crystal was aligned to the custom-made electrodes and optically contacted to them, as described in the experimental section. We aligned the crystal based on the guest transition dipole moment. As a verification, we could check that the cleavage planes of the crystal ((a, c) and (b, c) planes) appear as cracks due to thermal stress after the cryogenic experiment (Figure S2.2). More cracks are observed along the direction. This is expected based on the crystal packing presented in Figure 2.6.

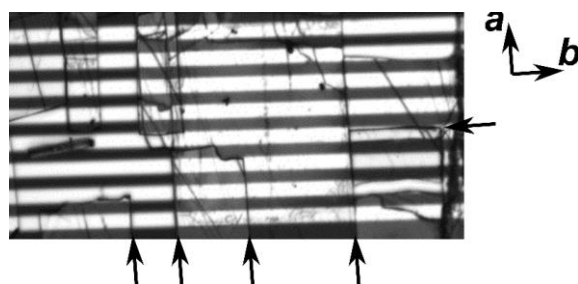


**Figure S2.2:** Optical micrograph of a cracked crystal taken after a cryogenic experiment. The bright parallel bands are the gold electrodes, with the interspacing distance of 10  $\mu\text{m}$ . The direction of several of the cracks reveals cleavage planes of the crystal along the a-axis, here parallel to the applied electric field, i.e., perpendicular to the electrodes.

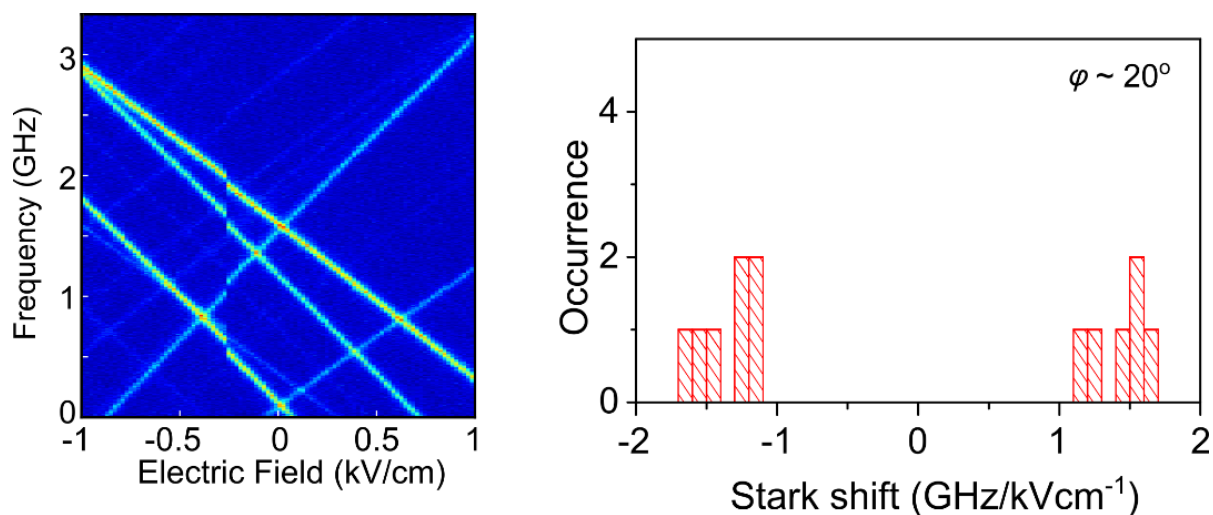


**Figure S2.3:** Left: The highest value of the Stark shift ( $1.56 \text{ GHz/kVcm}^{-1}$ ) is observed for the angle  $\phi = 20^\circ$  between the electric field and the crystal a-axis. Right: Corresponding histogram of the Stark shifts clearly showing four sub-populations. The discontinuity observed for electric field  $\sim -0.3 \text{ kV/cm}$  is due to a jump in the electric voltage source.

### 2.6.2. Calculation of the Stark Shifts: Four-dipoles Model

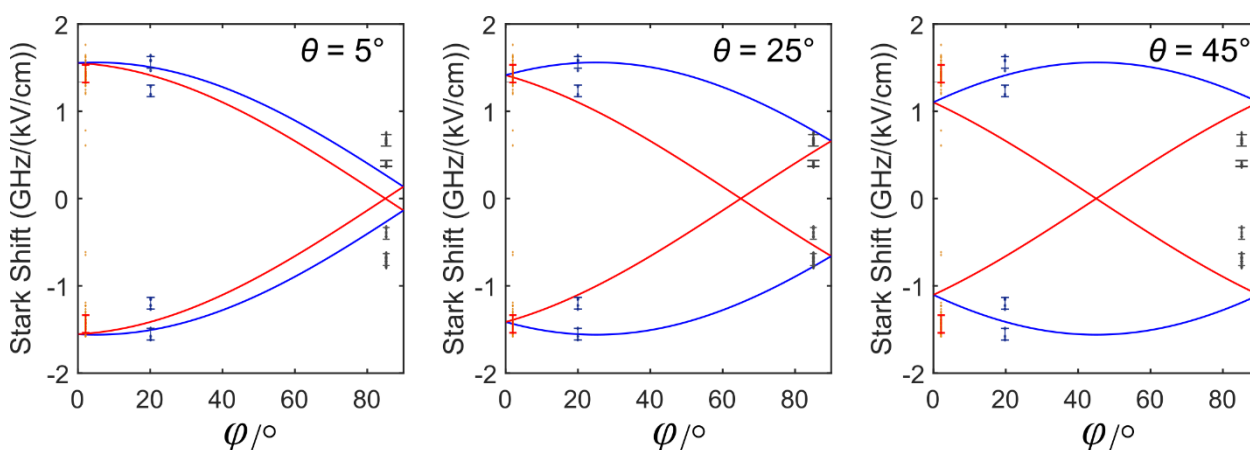


**Figure S2.4:** Calculated Stark shifts (red and blue lines) for three different values of  $\theta$  (angle between the a-axis and the dipole moment difference vector  $\Delta\mu$ ). The angle  $\phi$  is the angle between the a-axis and the electric field, as described in the main text. Experimental data points are shown as dots with error bars and compared with calculations (solid lines) for 3 values of  $\theta$ .

Although up to eight populations of molecules with different Stark effects can be expected in the general case, we could fit our data with four sub-populations only because the electric field was applied in the (a,b) plane of the crystal. For the simple model explained in the main text, we obtain a sinusoidal variation of the Stark coefficient with the angle  $\phi$  between the crystal a-axis and the electric field. Depending on the angle  $\theta$  between the dipole moment difference of one population with the a-axis, we obtain four different dependences for the Stark shift as a function of  $\phi$ . The plot of Figure S2.4 shows global fits of all measurement points for different values of  $\theta$ . The value  $\theta = 20^\circ \pm 5^\circ$  gives an excellent agreement with the measurements.

### 2.6.3. Unit cell and glide planes of the DBN host crystal

2,3-dibromonaphthalene crystallizes in the orthorhombic  $P_{bca}$  space group with 8 molecules in the unit cell (Figure S2.5); the lattice constants are:  $a = 11.692 \text{ \AA}$ ,  $b = 7.545 \text{ \AA}$ ,  $c = 20.193 \text{ \AA}$ ; see ref. 24 of the main text for more details. Each molecule in the unit cell is related to a reference one, for example molecule (1), by a symmetry operation, such as a glide plane. A glide plane is a symmetry operation associating (1) a reflection in the plane with (2) a translation parallel to that plane. The glide planes of 2,3-DBrN are shown as the red lines in Figure S2.5.

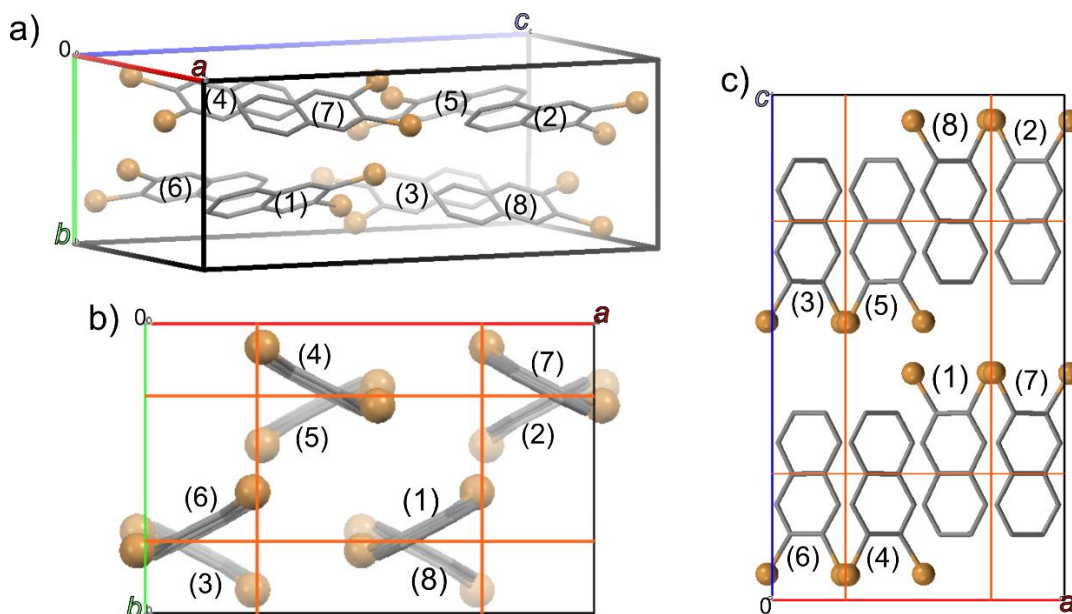


**Figure S2.5:** a) Unit cell of 2,3-dibromonaphthalene with numbered molecules. Molecule (1) is taken as a reference. b,c) Projections of the unit cell and corresponding glide planes (red lines), shown in (b) a-b, and (c) a-c plane. Each of the molecules in the unit cell is related to another one by glide planes or products thereof. Bromines are highlighted as golden balls to stress the broken symmetry of DBN molecules, whereas hydrogens are omitted for clarity.

The 7 operations relating a reference molecule (e.g., mol. (1)) to the others molecules in the cell are: i) the inversion in the unit cell center (with mol. (5)), ii-iv) 3 glide planes, associating translations with reflections in (a,b) (mol. (6)), (b,c) (mol. (7)), and (c,a) (mol. (8)) planes, v-vii) 3 screw axes (2-fold) associating translations with rotations around a (mol. (3)), b (mol. (4)), c (mol. (2)) axes. The screw axis rotations are products of 2 glide plane reflections, and the inversion is the product of the 3 of them. All molecules in the unit cell are thus related to one another by glide planes or products of glide planes.



The symmetry operations for the designated molecules, in respect to molecule (1), are:

Molecule #	Description	Symmetry Operation
(1)	Identity	$x. y. z$
(2)	Screw $c$ -axis (2-fold)	$\frac{1}{2} - x. -y. 1/2 + z$
(3)	Screw $a$ -axis (2-fold)	$\frac{1}{2} + x. \frac{1}{2} - y. -z$
(4)	Screw $b$ -axis (2-fold)	$-x. \frac{1}{2} + y. 1/2 - z$
(5)	Inversion center	$-x. -y. -z$
(6)	Glide ( $a, b$ ) plane	$\frac{1}{2} + x. y. 1/2 - z$
(7)	Glide ( $b, c$ ) plane	$\frac{1}{2} - x. \frac{1}{2} + y. z$
(8)	Glide ( $a, c$ ) plane	$x. \frac{1}{2} - y. 1/2 + z$

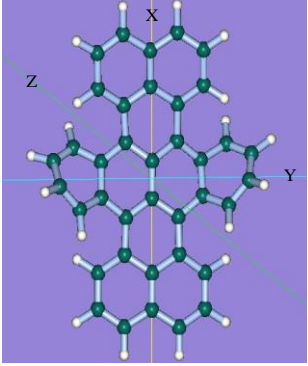
## 2.6.4. DFT Calculations

**Table S2.1:** Cartesian coordinates of DBT optimized in DBN crystal by ONIOM(B3LYP/6-31G(d,p):UFF) method. E(RB3LYP) = -1460.01164427 au;  $\mu$  = 0.6954 D.

<i>atom</i>	<i>x</i>	<i>y</i>	<i>z</i>	<i>atom</i>	<i>x</i>	<i>y</i>	<i>z</i>
	5.813991	-1.244366	0.050208	C	-1.151752	-3.433592	-0.904995
C	5.132390	-0.004193	0.119411	C	-0.700916	-4.420353	-0.153958
C	5.112554	-2.402917	-0.205659	C	0.200473	-4.263671	0.947477
C	3.700885	0.013277	0.066504	C	1.139221	-3.340861	0.728851
C	3.712366	-2.378853	-0.316408	C	-1.227788	3.510411	-1.015905
C	2.987591	-1.204350	-0.082837	C	-0.894976	4.548123	-0.242088
C	5.830300	1.225021	0.174225	C	0.056581	4.319369	0.821454
C	2.980012	1.246581	0.056758	C	1.024911	3.413003	0.689233
C	1.533804	-1.146912	-0.095970	H	6.897952	-1.252687	0.125156
C	3.728360	2.420129	-0.011581	H	3.231368	3.365528	-0.167085
C	5.128485	2.402954	0.069944	H	5.656906	3.341109	0.012511
C	1.519874	1.214849	-0.050380	H	5.640065	-3.341666	-0.347541
C	0.793285	0.031293	-0.124301	H	6.915631	1.222116	0.224144
C	0.716992	2.335732	-0.143304	H	3.199691	-3.287317	-0.605484
C	-0.669035	0.037769	-0.130308	H	2.102236	-3.300159	1.171391
C	0.742275	-2.265634	-0.064930	H	0.345961	-5.025335	1.689127
C	-0.624369	-2.221621	-0.470110	H	-0.898886	-5.375432	-0.524632
C	-0.641094	2.291898	-0.627001	H	-1.889932	-3.545389	-1.677632
C	-1.408219	-1.140152	-0.244871	H	-2.051000	3.559127	-1.708697
C	-1.422463	1.192894	-0.343712	H	-1.426465	5.457366	-0.471352
C	-2.863662	-1.250468	-0.110214	H	0.167049	4.875715	1.731306
C	-2.896330	1.194626	-0.161058	H	1.838288	3.341627	1.398016
C	-3.597991	-0.043904	-0.065115	H	-3.106074	3.271182	0.160333
C	-3.549187	-2.448153	0.124286	H	-5.587616	3.227551	0.464997
C	-4.946274	-2.486730	0.263203	H	-6.806434	1.110008	0.374913
C	-5.680056	-1.325260	0.227138	H	-6.763261	-1.336239	0.305808
C	-5.016702	-0.080758	0.128470	H	-5.435433	-3.445403	0.408160
C	-5.726739	1.132081	0.257861	H	-3.010670	-3.373897	0.231376



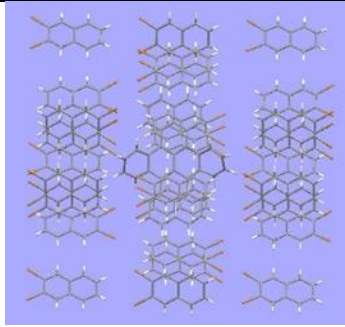
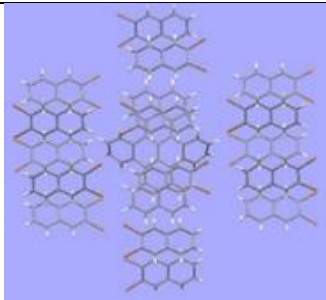
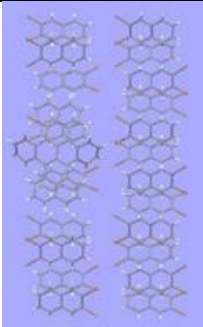
**Table S2.2:** Structure of the DBT molecule as deformed in the crystal field (see Table S2.1). Components of the dipole moments in the electronic ground  $S_0$  and excited  $S_1$  states of a DBT molecule, their difference ( $\mu(S_1) - \mu(S_0)$ ), and the transition moment  $\mu(S_0 \rightarrow S_1)$ , all given in Debye (D). The last column shows the results obtained with the use of B3LYP/STO-3G method, which was also used for the calculations of dipole moments of the whole DBT-DBN system.

		X	Y	Z	$ \mu $	$ \mu (\text{STO-3G})$
	$\mu(S_0)$	-0.626	-0.095	0.287	0.695	0.671
	$\mu(S_1)$	-0.168	-0.205	0.265	0.375	0.338
	$\mu(S_0 \rightarrow S_1)$	7.770	0.102	-0.282	7.776	8.285
	$\mu(S_1) - \mu(S_0)$	0.458	-0.110	-0.022	0.472	0.822

**Table S2.3:** Calculation of the ground state dipole moment of a DBT molecule embedded in a DBN crystal. Components of the dipole moments of (1) an empty cavity created by removing 3 host molecules along the a-axis, (2) the system upon embedding of a DBT molecule into the cavity, and (3) the resulting difference. a, b, c denotes the unit cell axes. Dipole moments are given in Debye [D]. Dipole moments were calculated with the use of TD B3LYP/STO-3G method.

	a	b	c	$ \mu $
(1) Cavity without DBT	-1.750	-0.354	0.232	1.800
(2) DBT in DBN	-1.963	0.724	1.299	2.463
(2) – (1) difference	-0.213	1.079	1.067	1.532

**Table S2.4:** Quantum chemistry calculations of the electric dipole moments of the ground and excited states of DBT in DBN matrix. Projections of the transition dipole moment  $\mu_{ge}$  and dipole moments  $\mu_g$ ,  $\mu_e$ ,  $\Delta\mu = \mu_e - \mu_g$  of DBT obtained for the different simulation cells. The number of DBN molecules in the simulation cell was varied from 21 to 28.

Calculated system Number of DBN molecules	Dipole moment of empty cavity		<i>a</i> -axis	<i>b</i> -axis	<i>c</i> -axis	$ \mu $
 28	6.631	$\mu_{ge}(S_0 \rightarrow S_1)$	8.015	0.382	0.459	8.037
		$\mu_g(S_0)$	-0.615	-0.659	-7.738	7.791
		$\mu_e(S_1)$	0.144	-0.791	-8.420	8.458
		$\mu_e(S_1) - \mu_g(S_0)$	0.759	-0.133	-0.681	1.028
 24	0.780	$\mu_{ge}(S_0 \rightarrow S_1)$	7.930	0.434	0.359	7.950
		$\mu_g(S_0)$	-0.276	-0.699	-1.032	1.277
		$\mu_e(S_1)$	0.475	-1.409	-1.165	1.889
		$\mu_e(S_1) - \mu_g(S_0)$	0.751	-0.710	-0.133	1.042
 21	1.663	$\mu_{ge}(S_0 \rightarrow S_1)$	-8.513	1.141	-0.104	8.590
		$\mu_g(S_0)$	0.002	-3.634	-0.446	3.661
		$\mu_e(S_1)$	-0.802	-4.214	-0.502	4.319
		$\mu_e(S_1) - \mu_g(S_0)$	-0.804	-0.580	-0.056	0.993

## References

- (1) B. Lounis, W. E. Moerner, *Nature* **2000**, 407, 491–493.
- (2) Y. L. A. Rezus, S. G. Walt, R. Lettow, A. Renn, G. Zumofen, S. Götzinger, V. Sandoghdar, *Phys. Rev. Lett.* **2012**, 108, 093601.
- (3) G. Wrigge, I. Gerhardt, J. Hwang, G. Zumofen, V. Sandoghdar, *Nat. Phys.* **2008**, 4, 60–66.
- (4) C. Hettich, C. Schmitt, J. Zitzmann, S. Kühn, I. Gerhardt, V. Sandoghdar, *Science* **2002**, 298, 385–389.
- (5) T. Basché, W. E. Moerner, M. Orrit, U. P. Wild, Eds., *Single Molecule Optical Detection, Imaging and Spectroscopy*, VCH, Weinheim, **1997**.
- (6) W. E. Moerner, M. Orrit, *Science* **1999**, 283, 1670–1676.
- (7) Y. Tian, P. Navarro, M. Orrit, *Phys. Rev. Lett.* **2014**, 113, 135505.
- (8) U. P. Wild, F. Güttler, M. Pirotta, A. Renn, *Chem. Phys. Lett.* **1992**, 193, 451–455.
- (9) M. Orrit, J. Bernard, A. Zumbusch, R. I. Personov, *Chem. Phys. Lett.* **1992**, 196, 595–600.
- (10) C. Brunel, P. Tamarat, B. Lounis, J. C. Woehl, M. Orrit, *J. Phys. Chem. A* **1999**, 103, 2429–2434.
- (11) F. Kulzer, R. Matzke, C. Bräuchle, T. Basché, *J. Phys. Chem. A* **1999**, 103, 2408–2411.
- (12) P. Bordat, M. Orrit, R. Brown, A. Würger, *Chem. Phys.* **2000**, 258, 63–72.
- (13) T. Y. Latychevskaia, A. Renn, U. P. Wild, *Chem. Phys.* **2002**, 282, 109–119.
- (14) M. Bauer, L. Kador, *J. Lumin.* **2002**, 98, 75–79.
- (15) M. Bauer, L. Kador, *J. Phys. Chem. B* **2003**, 107, 14301–14305. (16 P. Bordat, R. Brown, *Chem. Phys. Lett.* **2000**, 331, 439–445.
- (17) T. Plakhotnik, *ChemPhysChem* **2006**, 7, 1699–1704.
- (18) T. Plakhotnik, *J. Lumin.* **2007**, 127, 235–238.
- (19) S. Faez, S. J. van der Molen, M. Orrit, *Phys. Rev. B* **2014**, 90, 205405.
- (20) A. A. L. Nicolet, C. Hofmann, M. A. Kol'chenko, B. Kozankiewicz, M. Orrit, *ChemPhysChem* **2007**, 8, 1215–1220.
- (21) P. Türschmann, N. Rotenberg, J. Renger, I. Harder, O. Lohse, T. Utikal, S. Götzinger, V. Sandoghdar, *Nano Lett.* **2017**, 17, 4941–4945.

- (22) P. Lombardi, A. P. Ovyvan, S. Pazzagli, G. Mazzamuto, G. Kewes, O. Neitzke, N. Gruhler, O. Benson, W. H. P. Pernice, F. S. Cataliotti, C. Toninelli, *ACS Photonics* **2017**, 5, 126–132
- (23) D. Wang, H. Kelkar, D. Martin-Cano, T. Utikal, S. Göttinger, V. Sandoghdar, *Phys. Rev. X* **2017**, 7, 021014. (24) S. Pazzagli, P. Lombardi, D. Martella, M. Colautti, B. Tiribilli, F. S. Cataliotti, C. Toninelli, *ACS Nano* **2018**, 12, 4295–4303.
- (25) C. Kurtsiefer, S. Mayer, P. Zarda, H. Weinfurter, *Phys. Rev. Lett.* **2000**, 85, 290–293.
- (26) X. Ding, Y. He, Z.-C. Duan, N. Gregersen, M.-C. Chen, S. Unsleber, S. Maier, C. Schneider, M. Kamp, S. Höfling, *Phys. Rev. Lett.* **2016**, 116, 020401.
- (27) I. Aharonovich, D. Englund, M. Toth, *Nat. Photonics* **2016**, 10, 631–641.
- (28) A. A. L. Nicolet, P. Bordat, C. Hofmann, M. A. Kol'chenko, B. Kozankiewicz, R. Brown, M. Orrit, *ChemPhysChem* **2007**, 8, 1929–1936.
- (29) S. Faez, N. R. Verhart, M. Markoulides, F. Buda, A. Gourdon, M. Orrit, *Faraday Discuss.* **2015**, 184, 251–262.
- (30) Y. Tian, P. Navarro, B. Kozankiewicz, M. Orrit, *ChemPhysChem* **2012**, 13, 3510–3515.
- (31) M. Białkowska, W. Chaładaj, A. Makarewicz, B. Kozankiewicz, *Acta Phys. Pol. A* **2015**, 128, RK.3.1.
- (32) M. Białkowska, W. Chaładaj, I. Deperasin'ska, A. Drzewiecka-Antonik, A. E. Koziol, A. Makarewicz, B. Kozankiewicz, *RSC Adv.* **2017**, 7, 2780–2788.
- (33) Gaussian 09, Revision B.01, M. J. Frisch, G. W. Trucks, H. B. Schlegel, G. E. Scuseria, M. A. Robb, J. R. Cheeseman, G. Scalmani, V. Barone, B. Mennucci, G. A. Petersson, H. Nakatsuji, M. Caricato, X. Li, H. P. Hratchian, A. F. Izmaylov, J. Bloino, G. Zheng, J. L. Sonnenberg, M. Hada, M. Ehara, K. Toyota, R. Fukuda, J. Hasegawa, M. Ishida, T. Nakajima, Y. Honda, O. Kitao, H. Nakai, T. Vreven, Jr. J. A. Montgomery, J. E. Peralta, F. Ogliaro, M. Bearpark, J. J. Heyd, E. Brothers, K. N. Kudin, V. N. Staroverov, T. Keith, R. Kobayashi, J. Normand, K. Raghavachari, A. Rendell, J. C. Burant, S. S. Iyengar, J. Tomasi, M. Cossi, N. Rega, J. M. Millam, M. Klene, J. E. Knox, J. B. Cross, V. Bakken, C. Adamo, J. Jaramillo, R. Gomperts, R. E. Stratmann, O. Yazyev, A. J. Austin, R. Cammi, C. Pomelli, J. W. Ochterski, R. L. Martin, K. Morokuma, V. G. Zakrzewski, G. A. Voth, P. Salvador, J. J. Dannenberg, S. Dapprich, A. D. Daniels, O. Farkas, J. B. Foresman, J. V. Ortiz, J. Cioslowski, D. J. Fox, Gaussian Inc., Wallingford CT, **2010**
- (34) I. Deperasin'ska, B. Kozankiewicz, *Chem. Phys. Lett.* **2017**, 684, 208–211.
- (35) C. R. Groom, I. J. Bruno, M. P. Lightfoot, S. C. Ward, *Acta Crystallogr. Sect. B Struct. Sci. Cryst. Eng. Mater.* **2016**, 72, 171–179.
- (36) P. Trschmann, N. Rotenberg, J. Renger, I. Harder, O. Lohse, T. Utikal, S. Göttinger, V. Sandoghdar, *ArXiv:1702.05923v1 Cond-Mat Physics* **2017**.
- (37) I. Deperasin'ska, E. Karpiuk, M. Banasiewicz, B. Kozankiewicz, *Chem. Phys. Lett.* **2010**, 492, 93–97





# 3

## **Laser-induced frequency tuning of fourier-limited single-molecule emitters**

The local interaction of charges and light inorganic solids is the basis of distinct and fundamental effects. We here observe, at the single-molecule scale, how a focused laser beam can locally shift by hundreds of times their natural line width and, in a persistent way, the transition frequency of organic chromophores cooled at liquid helium temperature in different host matrices. Supported by quantum chemistry calculations, the results can be interpreted as effects of a photoionization cascade, leading to a stable electric field, which Stark shifts the molecular electronic levels. The experimental observation is then applied to a common challenge in quantum photonics, i.e., the independent tuning and synchronization of close-by quantum emitters, which is desirable for multiphoton experiments. Five molecules that are spatially separated by about  $50\mu m$  and originally  $20GHz$  apart are brought into resonance within twice their line width. This tuning method, which does not require additional fabrication steps, is here independently applied to multiple emitters, with an emission line width that is only limited by the spontaneous decay and an inhomogeneous broadening limited to  $1nm$ . The system hence shows promise for photonic quantum technologies.

### 3.1. Introduction

Single fluorescent molecules of polycyclic aromatic hydrocarbons (PAHs) embedded in crystalline organic matrices are widely considered highly coherent, stable, and bright two-level quantum systems in the solid state.<sup>1-5</sup> Indeed, they can be operated as single-photon sources,<sup>6</sup> combining high count rate and Fourier-limited line widths,<sup>7-9</sup> or as nanoprobe with exquisite sensitivity to electric fields, pressure, and strain.<sup>10,11</sup> PAH-based quantum devices can also be readily integrated in photonic chips.<sup>12-15</sup> A major advantage of PAH systems resides in the possibility to mass produce nominally identical fluorescent molecules at low costs and still obtain outstanding optical and optoelectronic properties. PAHs are under investigation for their use also in organic solar cells,<sup>16</sup> as well as in super-resolution microscopy methods.<sup>17</sup> Furthermore, the Stark effect is a well-established technique for tuning the molecular transitions.<sup>18-20</sup> Broad tunability has been demonstrated for instance in the case of anthracene nanocrystals (Ac NCXs) doped with dibenzoterrylene (DBT) molecules, exhibiting a quadratic Stark shift upon the application of a voltage bias (tuning range  $> 400$  GHz, comparable to the inhomogeneous broadening).<sup>21</sup> Also a large linear and homogeneous Stark shift has been achieved, embedding DBT in 2,3-dibromonaphthalene (DBN), suggesting the system as a promising nanoprobe of electric fields and charges.<sup>22</sup> Such previous results demonstrate the potential of molecular-based techniques which, in principle, could also go beyond single-emitter devices. However, current tuning methods have to be scaled up, allowing for local control of the transition frequency. This is crucial to optimize coupling of multiple emitters to photonic structures, as well as quantum interference among distinct sources on chip. To this purpose, electrical tuning of the emission wavelength for multiple sources is challenging to implement. Optical control might instead enable simple, fast, and independent frequency tuning of separated emitters. Recent promising works have shown laser-induced frequency tuning of epitaxial quantum dots' transitions. Physical manipulation of the sample is in this case confined within the laser beam diameter, and localized tuning of the emitters is achieved *via* thermal annealing,<sup>23</sup> mechanical expansion through phase-change materials,<sup>24</sup> or controlled strain through the host/substrate medium.<sup>25</sup> Nevertheless, the observed decoherence and spectral diffusion of the emitters' line width can be detrimental in many applications.

In this work we demonstrate fabrication-free, micron-resolved, optical frequency tuning of individual DBT molecules. We attribute the laser-induced frequency tuning of the molecular zero-phonon line (ZPL) to a local Stark shift, associated with optically induced long-lived charge-separated states, which notably persists for at least several hours after the pump laser is switched off. We first demonstrate the versatility of the concept, studying DBT in two different types of molecular crystals. A full characterization of the laser-induced frequency tuning is presented. In particular, we show how the magnitude of the induced spectral shift can be extended over a broad frequency range, by acting on the pump laser parameters. We also verify that close-to-Fourier-limited emission and photostability are preserved at cryogenic temperatures after the tuning process. In the following section, we demonstrate the scalability of the presented method as we show



independent tuning of individual emitters down to 15 m in proximity. In particular, we prove that the method can be extended to the frequency scale of the inhomogeneous line broadening, achieving spectral shifts that are more than 3 orders of magnitude larger than the natural line width. We show ZPL frequency matching (within two linewidths) of five molecular emitters, all within a  $50 \times 50 \mu\text{m}$  area and initially  $> 20 \text{ GHz}$  apart in frequency. Finally, we propose a model based on the photoionization mechanism of charge generation and support it with low-level quantum chemistry calculations. Different routes for the charge generation process, which may be an alternative or concurrent to the one described by our model, are also briefly discussed.

Overall, the possibility of using an all-optical approach to shift the transition frequency of individual emitters while maintaining coherent spectral properties offers a promising tool for applications in quantum nanophotonics. In particular, the presented results will benefit the realization of scalable quantum photonic devices and protocols based on multiple photons and multiple single-molecule emitters. More generally, the concept of laser-induced charge separation *via* photo-ionization of molecules can have broader scope in applications of single-molecule emitters, for example in nanoscale sensing of charge-carrier generation and in understanding the photo-conductivity and photorefractive of organic semiconductors.

## 3.2. Methods

### 3.2.1. Sublimation growth of DBT:DBN Single Crystals

2,3-Dibromonaphthalene used in this work was purchased from Ark Pharm Inc. High-quality single crystals of zone-refined DBN doped with dibenzoterrylene molecules were obtained by co-sublimation at  $\sim 0.2$  bar of argon gas. To prevent perturbations from the convection flow in the sublimation chamber, the sublimator was kept horizontal during growth. The sublimation-grown crystals develop along the (a,b) plane as thin mm-sized plates or flakes, with a typical thickness of a few microns along the *c*-axis.

### 3.2.2. Preparation of DBT:Ac nanocrystals

Nanocrystals (NCs) of anthracene doped with a single-molecule concentration of DBT are grown by injecting 100  $\mu\text{L}$  of a 4:107 mixture of 1 mM DBT–toluene and 5 mM Ac–acetone solutions into 2 mL of sonicating Milli-Q water. After 30 min of sonication, solvents are completely dissolved and DBT:Ac NCs are formed as an aqueous suspension (for more details see ref S1). The nanocrystals are then deposited on the substrate via drop-casting of  $\sim 10 \mu\text{L}$  of the suspension followed by desiccation. In particular, the substrates employed in the experiment are simple glass coverslips and coverslips coated with sputtered gold (film thickness of  $\sim 200$  nm). After the deposition, NCs are protected from sublimation by spin-coating a 200 nm thick layer of poly(vinyl alcohol) (PVA). Solvents Ac and PVA were purchased from Sigma- Aldrich, water was deionized by a Milli-Q Advantage A10 system (resistivity of  $18.2 \text{ M}\Omega \times \text{cm}$  at  $25^\circ\text{C}$ ), and DBT was purchased from Mercachem.

### 3.2.3. Optical microscopy (DBT:DBN)

All single-molecule measurements with DBT:DBN crystals were done at 1.2 K in a home-built-liquid-helium bath cryostat. Single crystals of DBT:DBN were optically attached to a glass substrate containing interdigitated gold markers previously deposited by lithography, which served to locate different parts of the single crystal in consecutive experiments. All pump excitation experiments on DBT:DBN were performed on the crystal parts that were in contact with the glass substrate. Single DBT molecules were excited by a tunable continuous-wave Ti:sapphire laser (M Squared) at around  $756.7 \pm 0.2$  nm. This laser is denoted in the text as a probe (laser) beam. The frequency range of typically 10 GHz was scanned with 1000 points and 5 ms integration time per point, with a typical power of 0.3 to 0.7  $\mu$ W focused on the sample. The output of the laser was continuously monitored by an external Fabry–Perrot cavity. The response of this cavity was used to monitor the laser frequency drift in real time and to compensate for a small nonlinearity of the frequency scan. A second, more intense (pump) laser beam was used to induce spectral shifts in DBT:DBN crystals. The laser light was produced by a Coherent ring laser, operated with rhodamine 101 (640) dye and pumped with a 532 nm solid-state laser. The operating wavelength of the pump laser was at around 631 nm, and a typical power focused on the sample was 10  $\mu$ W to 5 mW. In all experiments the sample was scanned with either only a probe laser (756.7 nm) or simultaneously with both pump (631 nm) and probe lasers focused on the sample. The sample was scanned in a confocal epi-fluorescence arrangement using a scanning mirror (Newport, FSM-300-01). A  $\lambda/4$  wave plate was used to produce a circularly polarized beam for more efficient excitation of single DBT emitters. The fluorescence light was collected by a cryogenic objective (Microthek,  $NA = 0.8$ ) and detected by a single-photon counting module (Excelitas SPCM-AQRH-16) with a set of filters (Chroma HQ760LP and Semrock FF02-809/81) in the detection path.

### 3.2.4. Optical microscopy (DBT:Ac)

The optical characterization of individual DBT molecules in Ac NCs was performed with a home-built scanning fluorescence confocal microscope. All measurements were done at about 3.5 K, with the sample in a closed-cycle helium cryostat (Cryostation by Montana Instruments). The transition line width of individual molecules was measured under confocal resonant excitation, with a CW distributed feedback diode laser (Toptica, LD-0785-0080-DFB-1), named probe, which is centered at 784.6 nm and can be scanned continuously in frequency over a range of 800 GHz. Frequency shifts of molecules emission were generally induced in off-resonant configuration by using a CW external-cavity diode laser (Toptica, DLX110), named pump, centered at 767 nm and operated at higher power (also in confocal mode). In particular, the laser frequency can be tuned through fine tilting of the Bragg grating of the diode source, enabling mode-tuning within about  $\pm 4$  nm around the central value. Laser-induced shifting was also performed by using the probe laser operated at higher power. All laser sources were fiber-coupled and linearly polarized by means of a half-wave plate in the excitation path to allow for optimal

coupling to the single molecules' linear dipole. The excitation light was focused onto the sample by a glass-thickness-compensation air objective (OptoSigma 50 ×,  $NA = 0.67$ ,  $WD = 10.48$  mm) and scanned over the sample by a telecentric system and a dual-axis galvo-mirror. The Stokes-shifted fluorescence was hence separated from the excitation light through a dichroic mirror (Semrock FF776-Di01) and a long-pass filter (Semrock RazorEdge LP02-785RE-25) and detected by either an EMCCD camera (Andor iXon 885,  $1004 \times 1002$  pixels, pixel size  $8 \mu\text{m} \times 8 \mu\text{m}$ ), for measuring fluorescence space-maps and spectral properties, or by a SPAD (SPCM-AQRH-14-TR by Excelitas). A converging lens was inserted in the excitation path, just before the dichroic mirror, to switch between confocal and wide-field illumination. For the antibunching measurement shown in the SI, we employed a Hanbury-Brown and Twiss configuration, based on a fibered beam splitter, two fiber-coupled SPADs (SPCM-800-14-FC by Excelitas), and a time-correlated single-photon counting (TCSPC) card (PicoHarp 300 by PicoQuant). Fiber-coupling of the single-molecule fluorescence was achieved by means of an adjustable fiber-collimator and a free-space telescope for mode-matching.

### 3.3. Results and discussions

The optically induced frequency tuning of light emission is studied via single-molecule measurements on DBT chromophores embedded in two different host systems, namely, anthracene (Ac) nanocrystals doped with low DBT concentration ( $\sim 10^{-2}$  molecules/GHz) and DBN crystal flakes, doped with high DBT concentration ( $\sim 1$  molecule/GHz). The molecular components of the two studied systems and their electronic energy levels are summarized in Figure 3.1.a. We also report additional results on a third system of DBT in naphthalene in the SI, showing that the effect applies to a broader range of organic crystals. The studied systems share the same guest molecule (DBT) but are known to have different response to the electric field. In particular, DBT:DBN exhibits a large linear Stark coefficient due to the broken inversion symmetry of guest DBT molecules,<sup>22</sup> while DBT:Ac shows a quadratic Stark coefficient.<sup>7,21</sup>

All the experiments are performed at liquid helium temperatures. In these conditions, the purely electronic ZPL is about 40 to 60 MHz wide. The spectral line shape can be traced with a standard epifluorescence microscope by scanning the frequency of the CW excitation laser (named “probe” hereafter) around the resonant wavelength. The Stokes-shifted fluorescence, spectrally selected through a long-pass filter, is correspondingly measured with an avalanche photodiode, giving access to the excited state occupation probability as a function of the excitation wavelength.

Optical frequency tuning of the narrow-band ZPL is achieved by focusing on the target crystalline regions a second CW laser (named “pump” hereafter), generally operating at a different wavelength and higher intensity. In Figure 3.1.b,c, real-time information on the laser-induced shift is provided by color maps showing, as a function of time, the excitation spectra of DBT molecules, exposed to the pump laser for a long time interval. In Figure 3.1.a, simplified Jablonski diagrams are outlined, showing the energies of the

pump as well and probe lasers employed in the experiments. The probe laser is scanned over the ZPL transitions around 785 nm for DBT:Ac (Figure 3.1.b) and 756 nm for DBT:DBN (Figure 3.1.c), whereas the pump laser is centered at 765.8 and 630 nm, respectively.

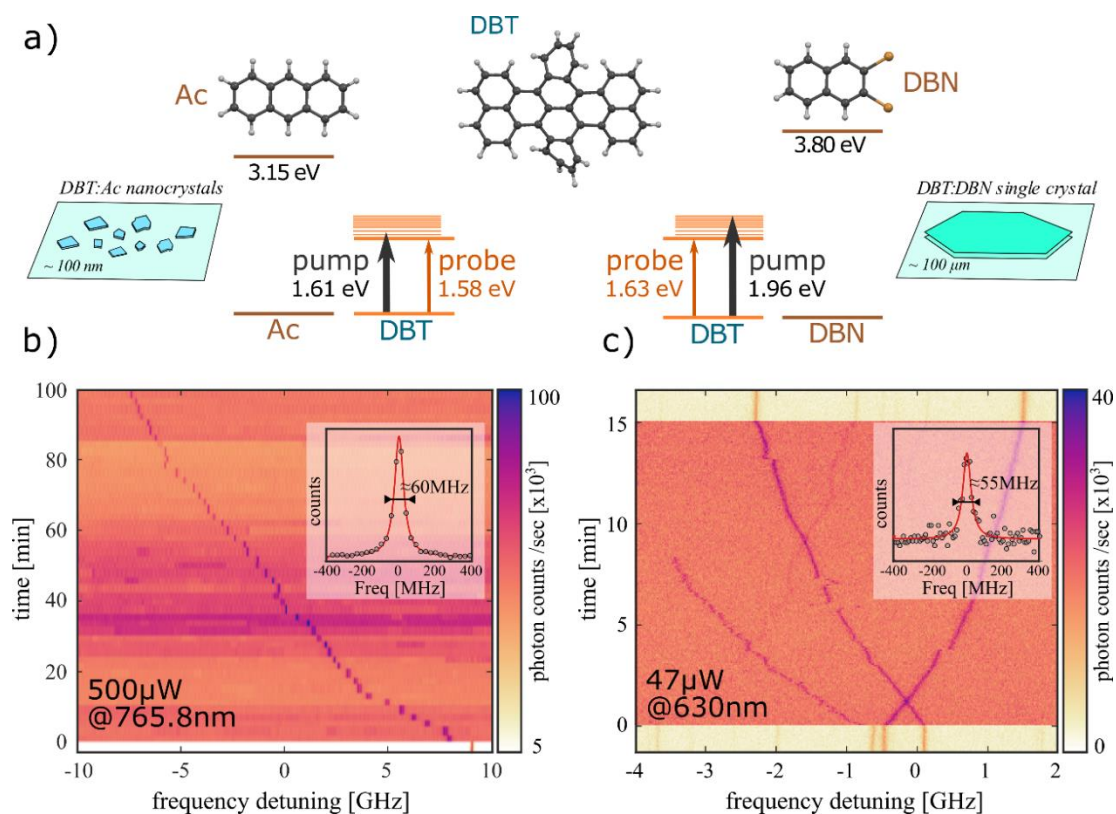


**Figure 3.1:** a) Chemical structures of the guest (DBT) and host molecules (Ac, DBN) used in this study. The energies of the pump and probe beams used in the experiments are indicated for comparison. Laser-induced frequency shift for DBT in Ac (b) and DBT in DBN (c). The fluorescence count rate is plotted in color scale as a function of the excitation laser frequency, scanning over the molecular ZPL. The measurements are repeated in time, while the pump laser is switched on. The pump presence is recognized by the onset of a strong background signal; that is, the light-yellow background represents scans without the pump beam. Insets in panels (b) and (c) represent horizontal cuts and include the Lorentzian fits to the data.

Zero-phonon lines corresponding to different molecules can thus be initially identified, followed during the burst duration above the background fluorescence, and recovered at different frequency positions after the exposure (Figure 3.1.c). It is worth noticing that after the pump laser illumination DBT molecules preserve excellent spectral stability and close-to-lifetime limited resonance line width. In particular, the spectral width amounts to  $\sim 60$  and  $\sim 55$  MHz for DBT:Ac and DBT:DBN, respectively (see insets in Figure 3.1). In the first case, the line broadening, compared to before the shift procedure, is unchanged and is attributed to the higher temperature of about 3.5 K at which the experiment is held. Spectral wandering is present in these samples and is related to the fluctuations of the local electric field, due to charge migrations. The energy shift in DBT emission persists even after the pump is turned off for about 24 h, ruling out the hypothesis of temporary heating effects. Furthermore, the frequency increment after each probe

scan (single row in the color map), on the order of a few line widths, hints at the possibility of a fine calibration of the effect, which is analyzed in more details in the following sections.

The number of DBT molecules exposed to the laser confocal illumination (beam diameter  $d \approx 1\mu m$ ) is different in the two host–guest systems. On a sample of distributed DBT:Ac NCX (Figure 3.1.b), a single nanocrystal can be isolated within the beam area, which implies that typically only one molecule is resonant within a  $500GHz$  scan of the probe. However, this cannot exclude the presence of broader molecules on the surface that could be weakly resonant with the intense pump laser. The reported frequency shift is always toward longer wavelengths, in agreement with the characteristic quadratic Stark effect of DBT in Ac.<sup>21</sup> On the other hand, within the highly doped DBN flakes, the confocal volume typically contains several chromophores within a  $10GHz$  scan of the probe-laser frequency. As reported in Figure 3.1.c, shifts with opposite signs are observed within the sample of DBT:DBN, for which a large linear Stark coefficient has been reported.<sup>22</sup>

Importantly, although each individual molecule may sense slightly different local electric fields (see the SI for more information), the fairly homogeneous response of most emitters in this well-defined system indicates that the laser-induced effect acts on all emitters within the diffraction-limited volume. These results jointly corroborate the interpretation of a laser-induced electric field buildup, leading to a Stark effect.

It is worth noticing that, when the pump is switched on, the measurements exhibit a strong background signal, which scales linearly with power. This light might be due to the presence of several DBT molecules within the illumination volume in the host matrices, weakly excited by the high-power pump laser. We note that such background shows much higher variability in the case of DBT:Ac than for DBT:DBN (Figure 3.1.b,c), as expected, since fewer molecules are involved in the former system. The role of nearby nonresonant DBT molecules in the shifting mechanism is thoroughly discussed further in the manuscript and in the Supporting Information. Notably, the emission purity for single-photon-based applications is not compromised by such background levels (see SI, Figure S3.3), since the pump power employed for single-photon source operation is much lower than that used to shift the ZPL frequency, yielding a negligible background level.<sup>26</sup> In particular, the statistical analysis of  $g^{(2)}(t)$  measurements on 40 DBT:Ac nanocrystals performed in our previous work<sup>27</sup> yields a single-photon purity higher than 97% for 82% of the cases. In the following, we discuss in detail the shift dependence on pump-burst duration, power, and wavelength.

### 3.3.1. Characterization of the light-induced frequency shift

The results on the dynamics of the optical tuning are analyzed in Figure 3.2, where the frequency shifts of individual molecules in the two host–guest systems are displayed (Figure 3.2.a,b for DBT:Ac and Figure 3.2.c for DBT:DBN). The experimental data represent the ZPL central frequency as a function of the cumulative pump exposure time and are extracted from the temporal map of the probe excitation spectrum *via* Lorentzian

fits. As the pictured data suggest, in each observed case the frequency shift slows down for long exposure times, with a characteristic time that typically varies among emitters and is, on average, different in the investigated matrix hosts. In general, such behavior can be fairly well described as a power-law function of time<sup>28</sup> (dashed red lines in the figure are fits to the experimental data):

$$v(t) = v(0) + \beta(P)(t/t_0)^\alpha \quad (3.1)$$

Where  $v$  is the molecule's ZPL central frequency,  $v(0)$  its initial value,  $t$  the cumulative pump-exposure time,  $t_0 = 1$  s the time normalization constant,  $\alpha$  the power exponent, and the parameter  $\beta(P)$  describes the extent of the frequency shift that can be achieved in a given exposure time. The specific dynamic parameters for the molecule's ZPL can vary among the two host matrices and even between different molecules within the same sample. This might be due to local differences in DBT concentration/orientation and to local crystalline impurities.

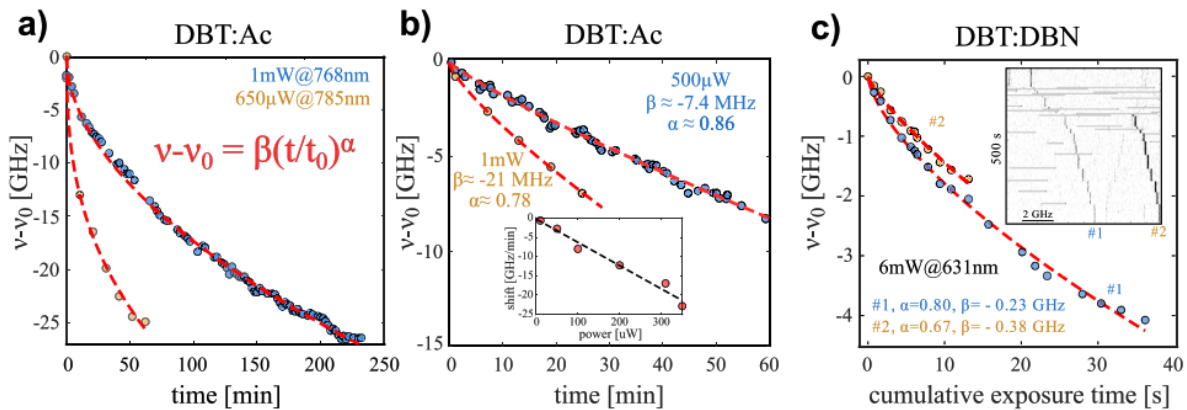


**Figure 3.2:** Dependence of the laser-induced shift on the exposure time and pump power for DBT:Ac (a, b) and DBT:DBN (c). The data points are the ZPL resonant frequencies obtained from a Lorentzian fit to the real-time excitation spectra, while the red dashed lines are power-law fits to the data. (a) Spectral shifts for pump laser frequency around the 0 – 1 transition (blue points) and tuned 10 GHz below  $v_0$  (yellow points) are compared. (b) Spectral shift dynamics for a DBT emitter pumped with different laser power. Inset: Spectral shifts of a second molecule subject to several 2 min long bursts at increasing power show a linear dependence on pump beam power. (c) Spectral shift as a function of cumulative exposure time for two DBT emitters (indicated as #1 and #2) in DBN. Inset: Frequency scans shown in real time (one line scan is 5 s). The gray horizontal lines indicate intermittent, short pump laser exposures (0.5 to 3 s).

Interestingly, no clear difference is observed in the induced shifts upon variation of the pump laser wavelength over a range of several nanometers (see also the SI). This suggests that the shift phenomenon can only be partially due to photon absorption by the shifting molecule. Indeed, this eventuality is ruled out by tuning the pump laser to the red of the molecule's ZPL, where no excited states exist. Figure 3.2.a shows in yellow dots the results of such an experiment, performed interrupting the pump illumination at regular intervals for about 1 h time. Despite a pump detuning of 10 GHz, a large frequency shift of  $> 20$  GHz is observed. Every DBT emitter conversely shows a clear dependence on the pump-laser power. Specifically, when comparing shifts induced in the very same

molecule, the parameter  $\beta$  is strictly increasing with the pump laser power and, for short enough illumination times, has a linear dependence. In Figure 3.2.b two frequency shifts operated on the same molecule, exposed to different values of the pump laser power, are compared. In particular, for the higher power the ZPL is probed during brief interruptions of the pump illumination every few minutes, since a real-time measurement is precluded by the increased background fluorescence. In the inset of Figure 3.2.b, a collection of data is displayed for a molecule in a different nanocrystal, which exhibits considerably larger frequency shifts and enables a characterization for low pump power values. In this case the experimental data represent the overall frequency shifts observed after single illumination bursts of 2 min each with increasing pump power, illustrating the linear behavior of  $\beta(P)$  for short illumination time. This result rules out the possibility of the direct two-photon-induced photoionization of the matrix, which would have a quadratic power dependence.

Qualitatively similar trends are reported for DBT:DBN in Figure 3.2.c, where two DBT emitters in the same DBN crystal are simultaneously shifted using a sequence of short, high-power, laser bursts. The burst duration varies between 0.5 and 3 s with a constant laser power of 6 mW. While one of the molecules undergoes photobleaching or large spectral jump during the process, the other accumulates a total shift of 4 GHz in less than 40 s of cumulative excitation. More results on intermolecular differences in the DBT:DBN system are available in the SI.

We note that for the results presented in Figure 3.2.a–c, the modest fluctuations overlapping with the frequency shift in the emission can be related to spectral wandering, which is enhanced at the high power levels reached during pump exposure.

### 3.3.2. Tuning molecules into resonance

The advantages of the all-optical frequency tuning presented here are its spatial resolution and the flexibility of operation. Indeed, the effect is directly activated on the emitting sample with no need for additional nanofabrication steps (e.g., lithography or etching in order to define the electrodes), and being confined to the confocal beam volume, it enables spatial resolution at the micron level. On the other side, once doped with single-molecule concentration, homogeneously deposited on the substrate via drop-casting and desiccation,<sup>27</sup> or even integrated in nanophotonic structures,<sup>15</sup> DBT:Ac nanocrystals allow for spatial isolation of individual molecules, which can thus be selectively tuned by laser focusing. This is shown in Figure 3.3, where the ZPL peaks of five nearby molecules, each contained in a different nanocrystal (data of different color), are probed at regular time intervals while exposing only one of the molecules to 2 min long laser pulses with increasing power. The corresponding molecule (blue in the figure) undergoes a large shift of about 100 GHz ( $\sim 0.20$  nm, corresponding to about a fifth of the inhomogeneous broadening and 2000 times the natural line width), whereas the transition frequency of others is not affected. In the inset, a wide-field fluorescence map shows the location of the respective nanocrystals, labeled with the same color code as in the main figure. Their



relative distance amounts to approximately  $10\ \mu\text{m}$  and is determined by the NCX suspension density before deposition. We note in passing that the limit to the spatial resolution of this approach has not been touched here and is likely determined by the specific charge migration mechanism in the sample.

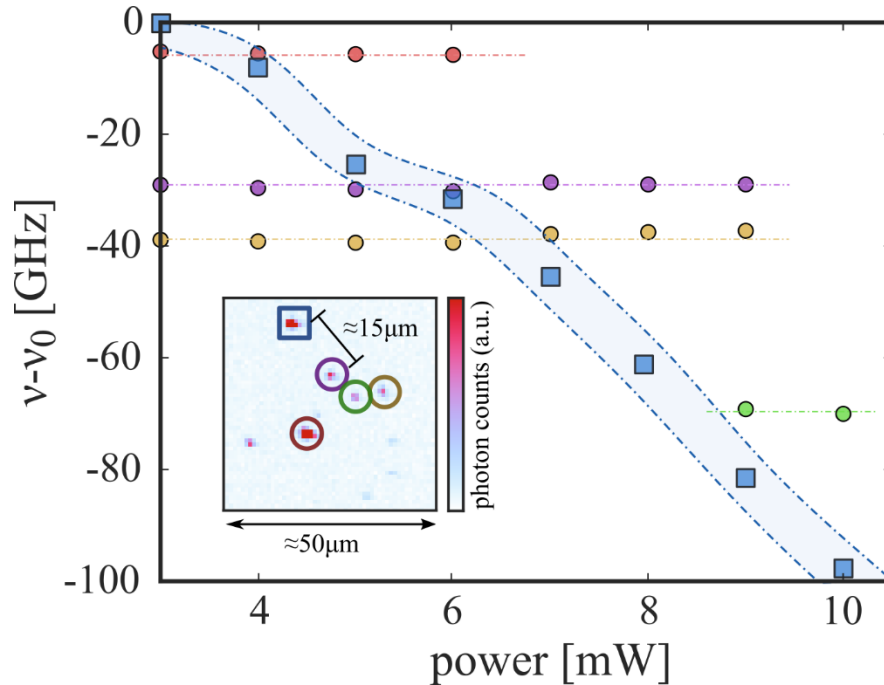


**Figure 3.3:** Localized frequency tuning. The central frequency of the ZPL is reported for several molecules as a function of the pump laser power, which only affects one of them (blue squares). The spatial distribution of the doped nanocrystals is given in the inset fluorescence map, revealing that as-close-as- $15\ \mu\text{m}$  molecules are completely unaffected by the manipulation.

Then we show the scalability of the proposed tuning approach, by shifting independently in a controlled way the ZPL of up to five close-by molecules, which are all brought on resonance within twice their line width. As in the case of the measurements shown in Figure 3.3, the emitters are embedded in different nanocrystals. Moreover their emission line widths, shown with the dashed lines in Figure 3.4, are originally well-separated by  $20\ \text{GHz}$ . The nanocrystals are addressed by the confocal pump-beam spot one after the other, independently, in order to shift their initial transition frequencies to a common targeted value. The latter, because of the dominant quadratic Stark effect in the Ac-matrix, is necessarily chosen as  $\nu_0 \leq \nu_i$ , where  $i$  labels the molecules' original emission frequencies. Based on previous calibration, the magnitude of the shift is adjusted by controlling the radiation dose (illumination power per exposure time). In general, the time required to shift the emission to a target frequency, which depends on the overall shift width, can be brought down to few minutes by playing on the pump laser power, as described in Figure 3.2.b. This is sufficiently quick to enable successive corrections for possible frequency deviations and hence preserve the target position for the time required to perform an experiment. The final excitation spectra are reported in Figure 3.4 using solid lines with shaded underlying areas in different colors, demonstrating fine-matching of five molecules, within about a two-line width range. Total shifts of up to about  $20\ \text{GHz}$



can be estimated by comparing the final values with the initial ones. In Figure 3.4.b, the relative wide-field fluorescence map is reported, showing the simultaneous excitation of all molecules by means of the probe beam centered at the targeted frequency  $\nu_0$ . Correspondingly, the bright spots highlight the spatial configuration of the synchronized nanocrystals. We finally observe that similar results have been obtained on different substrates, with nanocrystals deposited either on gold (SI), with a total shift of more than 20 GHz, or on sapphire (Figure 3.4). In particular, the current residual detuning of about two-line widths reported for five molecules and a line width for two molecules only depends on the spectral fluctuations arising during the pump-exposure process. Several mitigation techniques could be suitably implemented in the future to monitor and control the mutual frequency overlap of the emitters' ensemble, including an additional electrical bias to stabilize local charges.

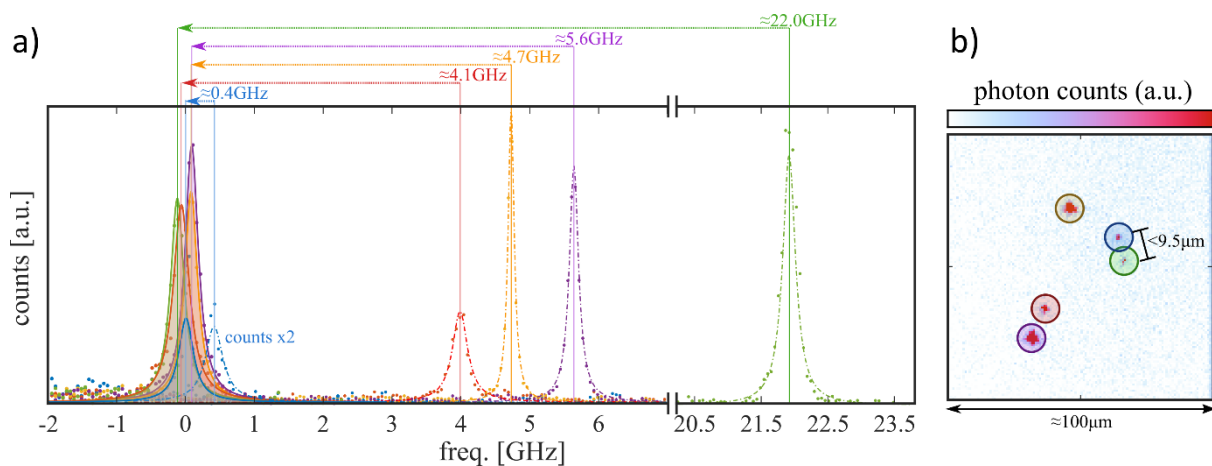


**Figure 3.4:** Frequency matching of five distinct molecules can be observed in the excitation spectra displayed in (a) as solid lines with underlying shaded areas. This exceptional condition is the result of a set of individual shifting applied to the original configuration, corresponding to the spectra reported as dashed dotted color lines. (b) Fluorescence map showing the simultaneous excitation of all nanocrystals when the probe is centered around  $\nu_0$  and applied in wide-field configuration.

The demonstrated results clearly show together several advantages of the proposed tuning approach: scalability, flexibility in the choice of substrate, high spectral and spatial resolution, and broad tunability range compared to the system's inhomogeneous broadening. We believe such characteristics will be crucial for the coupling of multiple emitters together in linear optical computing or simulation experiments and for the integration of molecules into resonant photonic structures.

### 3.3.3. Photoionization model of the laser-induced charge separation

In this section we propose a possible mechanism for our hypothesis of the laser-induced charge separation through photoionization of DBT molecules. We postulate a cascade photoionization mechanism for the buildup of the local electric field, *via* formation of long-lived charge-separated states.

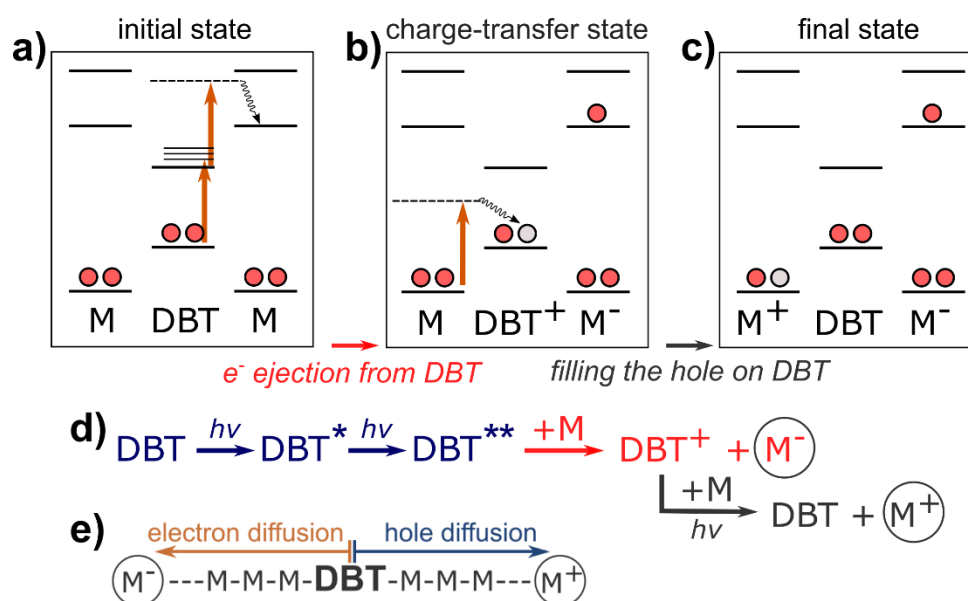


**Figure 3.5:** Proposed mechanism of the laser-induced charge generation. (a–c) Electronic energy diagrams describing (a) the initial electronic state and local excitation of DBT (red arrows), followed by electron ejection to the matrix (wavy line), (b) charge-transfer state and filling the hole on DBT, and (c) resulting final state of the system. Transitions induced by a single photon are shown with red arrows, virtual states are indicated by broken lines, and nonradiative CT transitions are indicated by wavy lines. Red and gray circles designate electrons and holes, respectively.  $M$  = matrix molecule (DBN or Ac). (d) Photoionization scheme that represents the path sketched in panels (a)–(c).  $h\nu$  = energy of a pump-beam photon; excited electronic states are represented with the star symbol. (e) The resulting charge carriers ( $M^+$  and  $M^-$ ) diffuse further into the charge-separated states under the illumination of the pump beam.

The proposed model is based on the following assumptions:

1. The laser-induced excitation of DBT molecules leads to their photoionization by electron ejection.
2. The process results in long-lived charge-separated states in the matrix. The initially excited DBT molecules may be regenerated to their neutral state.
3. The photoionization of DBT results in mobile charge carriers (electrons and holes, with different mobilities) and their transport to larger distances (on the order of tens of nanometers at least).
4. The charge separation and trapping of electrons and holes result in the buildup of a static electric field which shifts DBT's ZPLs through a Stark effect (quadratic for DBT:Ac and linear for DBT:DBN).

The laser-induced charge separation mechanism is outlined in Figure 3.5. The initial step of the charge generation process is the photoionization of DBT molecules by intense pump light (Figure 3.5.a). This process requires at least two laser photons: a first DBT excitation with one pump photon (1.61 eV for DBT:Ac or 1.96 eV for DBT:DBN) to its first excited electronic state (S1), followed by a further excitation with a second pump photon (red arrows in Figure 3.5.a). Such a highly excited electronic state of DBT can

presumably eject an electron to the matrix ( $M$ ) and give birth to a charge-separated state ( $\text{DBT}^+/M^-$ ). Finally, the hole left on the DBT molecule may be transferred to the matrix through a single-photon excitation (Figure 3.5.b), yielding back a neutral DBT molecule and a matrix cation ( $M^+$ ) (Figure 3.5.c). Figure 3.5.d summarizes the proposed photoionization cascade. However, while this is one of the most likely mechanisms, we note that other possible channels of light absorption and photoionization are also possible. The presence of dimers or clusters of DBT molecules, for instance, as well as other impurities, can red-shift the absorption spectrum by up to several thousands of  $\text{cm}^{-1}$ . This can explain the occurrence of the photoionization phenomenon for a broader range of pump frequencies. Notably, we observed that the spectral shifts in both DBT:Ac and DBT:DBN can be induced by using a pump beam at 795 nm, which is outside the inhomogeneous broadening of the studied systems (200 and 650  $\text{cm}^{-1}$  below the ZPL, respectively).

The migration of the induced charge carriers is possibly further activated by the pump beam, leading to charge diffusion and to charge-separated states ( $M^+$  and  $M^-$ ) far enough from each other so that the recombination probability becomes negligible (see Figure 3.5.e). It is important to realize that, if the initial DBT molecule is regenerated to its neutral state, the process can be repeated many times. In effect, each DBT molecule may give rise to a macroscopic charge distribution in its environment. The resulting charge density buildup shifts ZPLs of DBT probe molecules by the Stark effect.

Our photoionization scheme is inspired by earlier models of photoconductivity in organic solids. The inclusion of larger PAH impurities into an anthracene crystal, such as tetracene, significantly reduces the activation energy for the charge-carrier transport.<sup>29–31</sup> Likewise, the proposed charge separation mechanism is the key to the photorefractive effect in multicomponent photorefractive materials doped with optically active organic molecules.<sup>32</sup>

The suggested model is consistent with the continuous shift of the molecule's ZPL resonance, as well as with its narrow line, which rules out any heating-induced rearrangements. The Stark shift associated with a net field buildup well captures a shift that can have opposite signs for DBT:DBN, while is only toward longer wavelengths for DBT:Ac. Further details on the consistency between the model and the experimental observations are provided in the SI.

Finally, simple quantum chemistry calculations have been performed, which qualitatively support our photoionization model. All three steps presented in Figure 3.5 are found to be energetically feasible according to time-dependent density functional theory (TDDFT/B3LYP). For the details of the calculations, the reader is referred to the SI. Beyond the first electronic excitation, several higher electronic states of DBT are found above 3.0 eV, suggesting that excitation of DBT with two red photons is likely to happen under experimental conditions of strong illumination. According to the calculations, the following step of electron transfer to the matrix could be phonon-assisted for DBT in Ac,

while a direct excitation of the charge-transfer (CT) state may operate as well for the DBT:DBN system. The formation of the CT excitations on the neighboring molecular sites is considered important for the transport properties of photoexcited organic materials.<sup>33</sup> Nevertheless, due to their short lifetimes,<sup>34,35</sup> the CT states cannot explain the buildup of the stable electric field, which persists for long time after the excitation. These states can be rather considered as the precursors for the photoinduced formation of free electrons and holes, which are separated to larger distances by the pump beam. The transport of charges is further supported by the presence of many host molecules in the crystals, which results in the formation of a quasi-band structure of CT-type electronic states (see the SI).<sup>36</sup> Concerning the regeneration of neutral DBT molecules, several CT transitions are found from Ac to DBT<sup>+</sup> within the energy range of our excitation (1.6 eV). Lastly, the further transfer of charge carriers through the matrix to distances larger than several unit cells is assumed to take place through interaction of charged species with red light. Indeed, we find that Ac<sup>+</sup>, Ac<sup>-</sup>, and DBT<sup>+</sup> can all absorb red photons, which is in line with other theoretical results.<sup>37</sup>

### 3.4. Conclusion

We have demonstrated optically induced tuning of light emission from single DBT molecules in two different types of molecular crystals that are of interest for molecule-based integrated quantum devices. Tuning by up to 0.2 nm ( $\sim 1/5$  of the inhomogeneous broadening) has been observed, persisting for a macroscopic time (several hours), which allows the successive manipulation of several independent molecules. Because of the predictability of the frequency shift, we were able to tune five independent molecules on the same ZPL emission wavelength within twice their line width. Such fine control of an emitter's transition frequency, together with the achievable tuning range, might empower the presented technique in any context involving molecular emitters coupled to resonating photonic structures and/or multiple sources emitting at the same wavelength, such as in optical quantum computation, simulation, and communication.

We emphasize the potential applicability of our methodology to a broad range of host/guest molecular systems. Studying light-induced charge dynamics with single-molecule sensitivity could shed light on the microscopic mechanisms behind photoconductivity in organic solids and motivates the exploitation of single molecules in quantum technologies and molecular electronics. Many possibilities to further fine-tune and manipulate optical transitions of molecules can be envisaged in this context. Finally, tuning light emission of many single emitters by using this simple optical approach may become an important step in integrating single emitters into robust quantum protocols based on molecules.

## 3.5. Supporting Information

### 3.5.1. Measurements of DBT:Ac nanocrystals

#### Shift dependence of power and pump laser wavelength

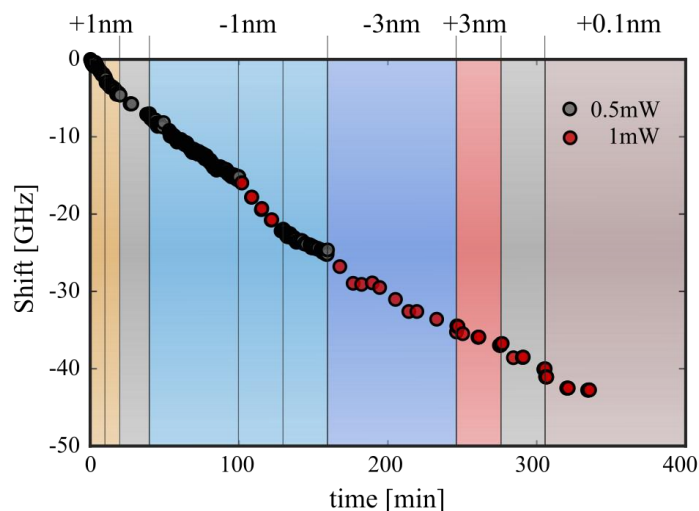


**Figure S3.1:** 0-0-ZPL transition shift induced on the same single molecule by a succession of “pump” laser bursts with different characteristics (wavelength and illumination power). The data-points are the ZPL resonant frequencies obtained from a Lorentzian fit to the excitation spectra. Data-points colors refer to the pump power value, whereas the temporal color-bands indicate the pump wavelength with respect to the most efficient excitation rate of the 0-1 transition, labeled in gray and corresponding to the pump at 767.8nm.

In Figure S3.1 the entire dynamics of the ZPL-transition frequency shift for an individual DBT molecule in an Ac-nanocrystal is reconstructed by monitoring its position after several consecutive burst exposures, operated with different parameters (illumination power and wavelength). The temporal colored bands indicate the pump wavelength value, according to the labeling on the right. Furthermore, colors of the dotted data refer to the two employed pump powers, one double (red) the other (black). This latter parameter change can be used as term of comparison: while the induced-shift dynamics is clearly dependent on the pump power (see also Figure 3.2.a in the main text), it is not visibly sensitive to wavelength. Consequently, we can state that the photochemistry process responsible for the charge separation and the Stark shift does not result from excitation of the DBT molecule under single-molecule investigation. Indeed, the spectral band explored in the measurements reported in Figure S3.1 corresponds to very different pumping efficiencies for a given illumination power. By comparison with a reference excitation spectroscopy of the 0-1 transition obtained for a different molecule (Figure S3.2), the excitation wavelengths labelled in gray in Figure S3.1 correspond to the strong peak at 764.7 nm, hence to the maximum excitation efficiency. The wavelength labelled in orange is instead associated to the plateau between the two resonance peaks, hence to an excitation efficiency reduced by more than one order of magnitude, while for 3 nm on the red (red band), we are close to the secondary resonance. Moreover, on the blue of the main peak it is established that no relevant resonances are present within 7 nm shift<sup>S2</sup> (not shown).

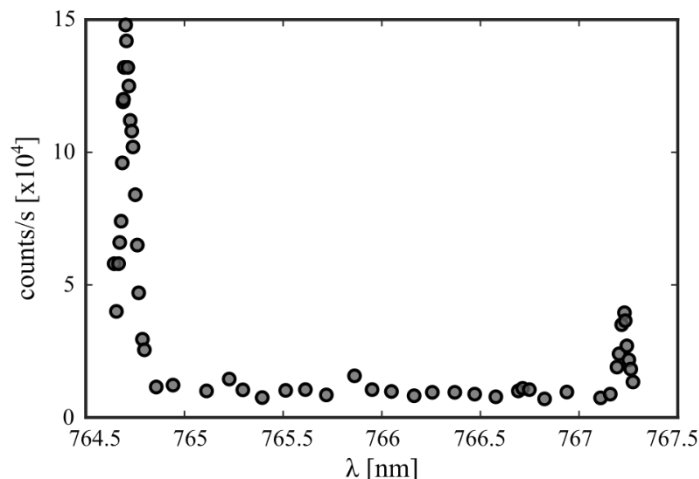


**Figure S3.2:** Excitation spectroscopy performed with the “pump” laser around the 01-ZPL transition: recording the spectrally integrated fluorescence intensity gives access to the pumping efficiency as a function of illumination wavelength. The reported spectrum is not measured for the same molecule of Figure S3.1, and in particular the main excitation peak in this case was shifted by around 3 nm to the blue with respect to the molecule of Figure S3.1. However, we have found evidence that the level scheme is almost rigidly shifted by the inhomogeneous broadening. Our findings are in substantial agreement with ref.[S2].

Despite this big variation on pumping efficiency, the laser-induced shift recorded in Figure S3.1 is not correspondingly affected by the difference in the excitation efficiency of the DBT molecule under investigation, as a function of the pump laser frequency. This is a relevant indication that the light-induced shift does not depend strongly on the target molecule's ZPL-transition.

### Measurement of the photon statistics: single photon purity

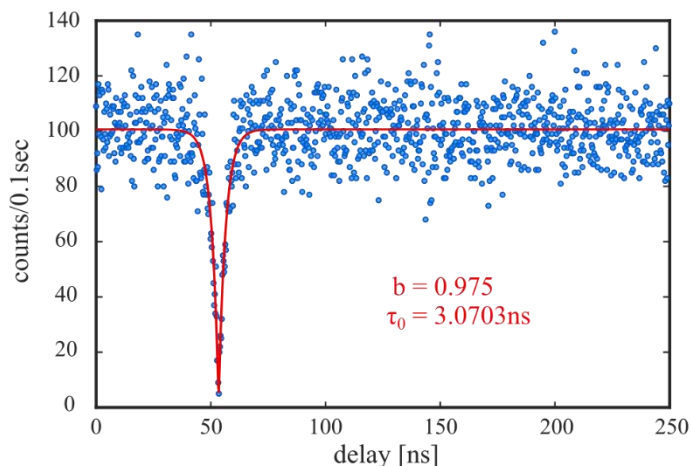


**Figure S3.3:** Anti-bunching measurement for fluorescence collected from an individual DBT:Ac nanocrystal under illumination with “pump” laser at 767 nm, evaluated as a histogram of the differential arrival times of the photons on two avalanche photodiodes in a Hanbury-Brown and Twiss configuration. The second-order autocorrelation function at zero delay is inferred by the best fit (red line) to the experimental data (blue dots), yielding  $g^{(2)}(0)=1-b=0.03\pm 0.03$ . In particular, the fit function is  $g^{(2)}(t) = A(1 - be^{-|t-t_0|/\tau})$ , with  $A$  a normalization factor,  $b$  anti-bunching dip depth,  $t_0$  a time delay and  $1/\tau$  accounting for the excitation and spontaneous emission rate.

In Figure S3.3 we show a representative example of anti-bunching measurements of an individual DBT:Ac nanocrystal. The data points are recorded under off-resonant excitation (767 nm). The second-order autocorrelation function at zero delay inferred by the fit to the experimental data yields  $g^{(2)}(0)=1-b=0.03\pm 0.03$ , which proves the high purity of the single-photon emission. This result is not in contradiction with the measurements reported in the main text (Figure 2), where we see a background comparable to the signal intensity. Indeed, shift measurements are performed with a strong illumination power (exciding by more than one order of magnitude the saturation level), which is able to excite other, more weakly coupled molecules. The latter are molecules without narrow lines, or with narrow lines at different wavelengths and/or spatially close to the one under investigation. With respect to the last “background source”, a relevant gain is obtained also thanks to the spatial selection introduced by fiber-coupling.

### Independence on the sample substrate

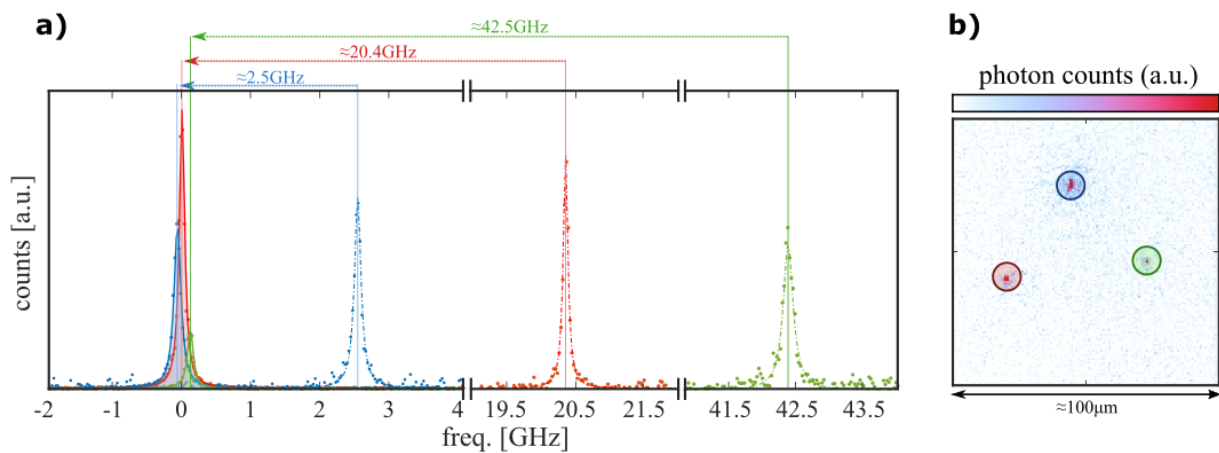


**Figure S3.4:** Frequency matching of three distinct molecules deposited on a gold substrate can be observed in the excitation spectra displayed in a) as solid lines with underlying shaded areas. This condition is the result of a set of individual shifting applied to the original configuration, corresponding to the spectra reported as dashed dotted color lines. b) fluorescence map showing the simultaneous excitation of all nanocrystals when the probe is centered around  $\nu_0$  and applied in wide-field configuration.

As mentioned in the main text, the shift phenomenon is independent on the substrate on which the NCX are deposited. Indeed, in Figure. S3.4 we report the result of an experiment in which three different DBT:Ac emitters, deposited on a gold substrate, have been tuned to the same reference frequency. The experiment is conceptually identical to the one reported in Figure 3.4 of the main text. However, in the case of DBT:Ac on gold, the accuracy can be slightly increased because of the generally stronger emission that one can get from emitters deposited on gold substrate with respect to glass substrate.



### 3.5.2. Measurements of DBT:DBN single crystals

#### Single-molecule trajectories and inter-molecular heterogeneity

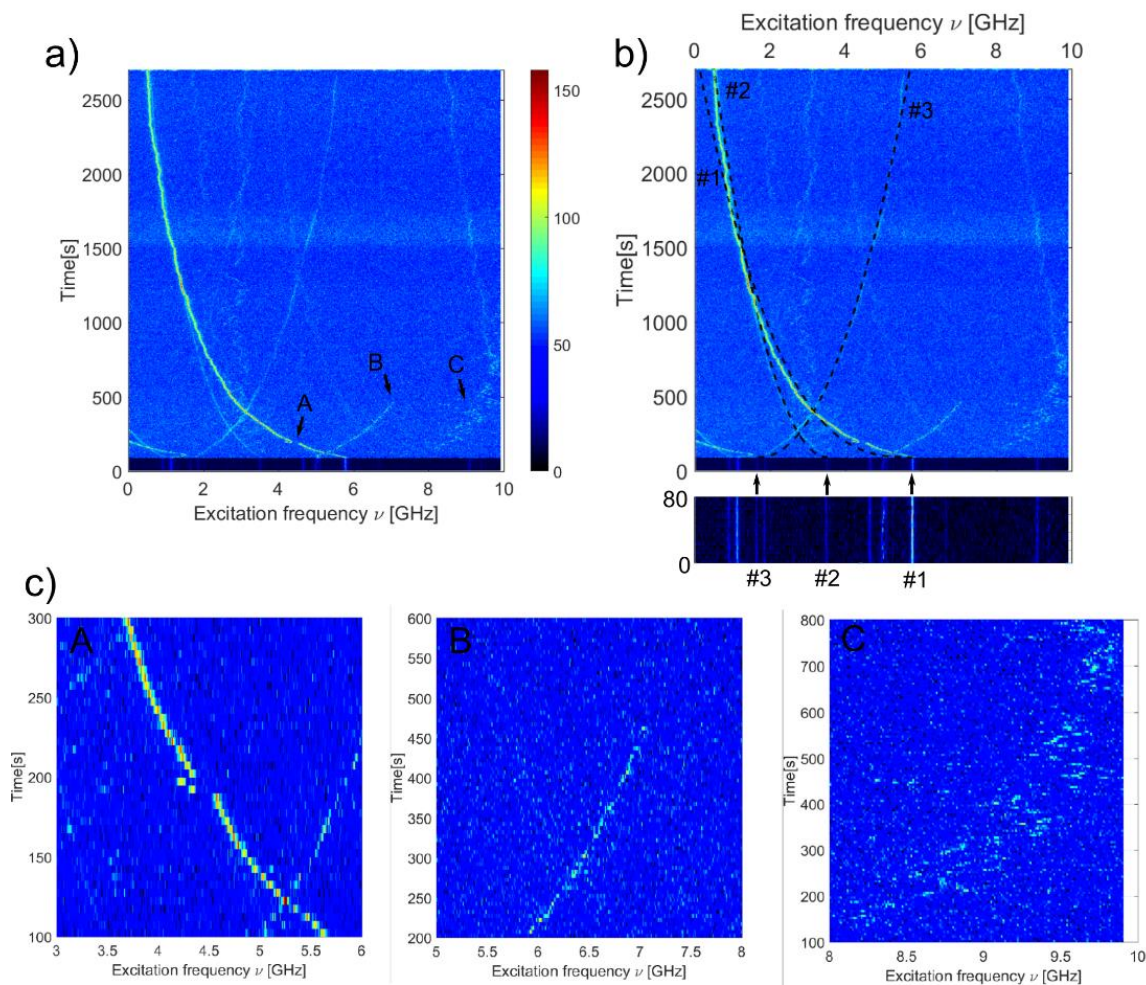


**Figure S3.5:** a) Single-molecule fluorescence excitation spectrum of DBT molecules in 2,3-DBN recorded in real time during exposure to a pump beam (631 nm, 45  $\mu$ W). Several ZPLs are visible showing different response to the pump beam. Highlighted events A-C are shown in (c). The dark blue background at the bottom indicates line scans without the pump beam. The probe beam was continuously scanned at 756.7 nm (0.7  $\mu$ W). Color bar: counts per 5 ms. b) Power law fits for three molecules, indicated with arrows; molecule #1 ( $\alpha=0.36$ ,  $B=-340$  MHz), molecule #2 ( $\alpha=0.49$ ,  $B=-60$  MHz), and molecule #3 ( $\alpha=0.47$ ,  $B=100$  MHz). The coefficients  $\alpha$  and  $B$  are as in eq. (1) of the main text. Note that molecule #1 has the largest shift, but also the largest departure from the power law fit. c) Typical examples of a smaller spectral jump possibly influenced by a nearby charge diffusion (A), large spectral jump or photobleaching event (B) and large and fast spectral diffusion with fast random jumps (C).

DBT:DBN single crystals are prepared by a co-sublimation method, using zone-refined DBN. This method is considered to produce molecular crystals of highest quality and purity. Furthermore, using these crystals with relatively high concentration of well-embedded DBT molecules, we can locally sense charging events, charge migration and fluctuations in electric field buildup. As each molecule is embedded in a slightly different environment, the response of individual molecules may differ. Figure S3.5 illustrates this on a set of several molecules. Apart from fairly stable trajectories in molecules #1, #2, and #3, one can discern other types of trajectories and local behaviors. For example, molecule #1 exhibits a small spectral jump



(labelled as A in Figure S3.5.c) for  $\sim 10$  s, which is likely an evidence of a nearby charging event. Event (B) highlights a molecule that suddenly photobleaches or undergoes a large spectral jump out of the frequency scan window (10 GHz). Trajectory (C) is from a spectrally unstable molecule that is seeing more frequent local perturbations due to local charge dynamics.

### Power law behavior of individual trajectories

Figure S3.5.b shows power law fits to three long trajectories presented in Figure S3.5.a. As can be seen, all molecules do not display the same electric field change, and their trajectories are quantitatively different. Furthermore, power law functions cannot fully describe the behavior of all individual molecules, but it is a fairly good approximation on larger timescales of up to 1 h. For example, molecule #1 in Figure S3.5.b shows the largest response to the pump beam, but its behavior is not well-fitted by a power law. On the other hand, molecules #2 and #3 show a fairly good match with a power law behavior and their fitting parameters are very similar, even for longer timescales.

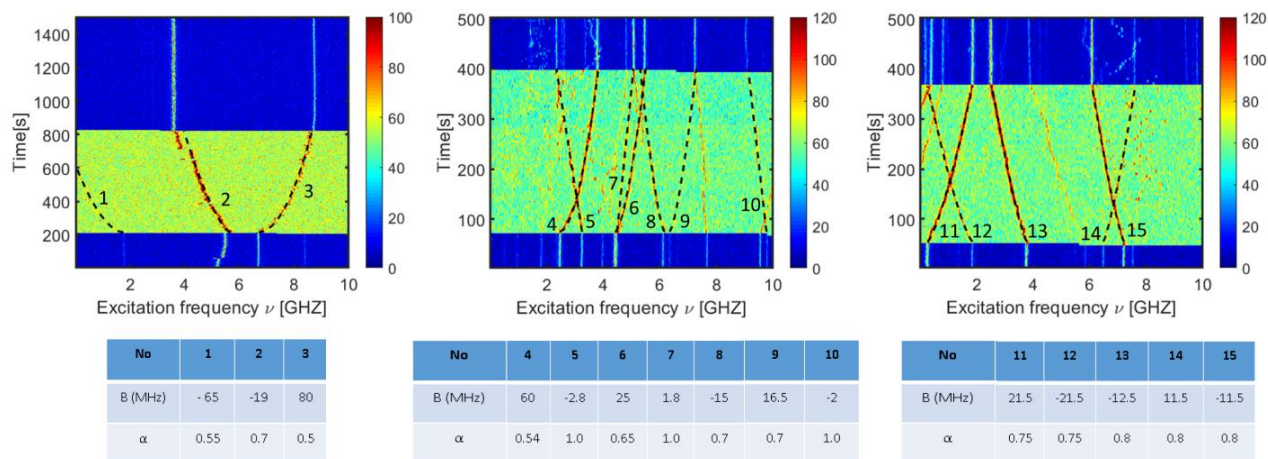


**Figure S3.6:** Examples of 15 single-molecule trajectories, recorded at different points on a DBT:DBN crystal. The trajectories are fitted with a power law equation,  $\nu = \nu_0 + B \cdot (t/t_0)^\alpha$ , where  $t_0 = 1$  s. The table includes fitted parameters B (MHz) and  $\alpha$  for all 15 molecules. The pump excitation power was in all experiments  $\sim 50 \mu\text{W}$  at 631 nm. Color bars: counts per 5 ms.

Despite the mentioned heterogeneities that are intrinsic to molecular systems perturbed with charging events at 1.2 K, we still find many molecules “well-behaving” in the pump beam. Figure S3.5 shows the examples of 15 single-molecule trajectories obtained on 3 different locations in a DBT:DBN crystal. All these trajectories (5 – 10 min long) are fitted well with a simple power-law equation. What is interesting to note is that up to several molecules in each scan can be fitted with very similar parameters B and  $\alpha$  (e.g. molecules 11-15 in scan 3, Figure S3.6), indicating that these DBT emitters experience very similar local electric fields. We find parameter  $\alpha$  mostly having values between 0.5 – 1.0, where the lower  $\alpha$  designates faster initial change in resonant frequency of a molecule and  $\alpha = 1$  means linear time dependence.

ZPLs of individual molecules do not drift or jump after the pump beam is switched off, as shown in Figure S3.7. In this example the ZPL was tuned with a fairly low power of the pump

beam ( $43 \mu\text{W}$ ). As shown in Figure 3.2 the ZPL lines remain stable and can be shifted much faster with more intense ( $6 \text{ mW}$ ), shorter pump pulses ( $1 - 3 \text{ s}$ ). This holds for a large majority of single emitters and indicates that charge reconfiguration in the crystal upon pump illumination is almost instantaneous, but it does no longer affect the frequency of the optical transition after the pump beam has been switched off. The latter observation indicates long recombination times and large electron-hole separations in the sample.

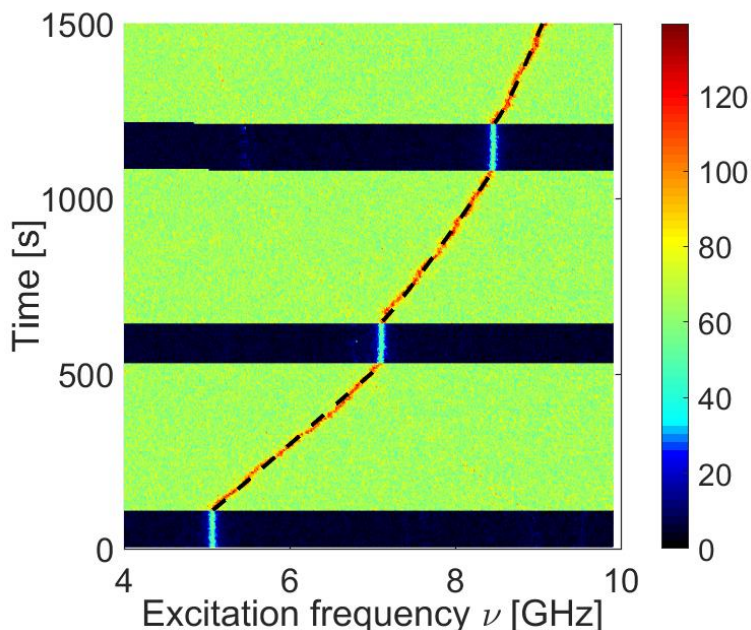


**Figure S3.7:** Start-stop experiment with alternating pump excitation (on/off), for DBT in 2,3-DBN. The pump beam excitation was  $43 \mu\text{W}$  at  $631 \text{ nm}$ , whereas the probe beam ( $0,7 \mu\text{W}$ ) was continuously scanned at  $756.7 \text{ nm}$ . Color bar: counts per  $5 \text{ ms}$ . Dashed lines represent power law fits to the data, with  $B = 5.2 \text{ MHz}$ , and  $\alpha_1=0.99$  (bottom fit),  $\alpha_2=0.92$  (middle fit),  $\alpha_3=0.84$  (top fit).

### Spectral shift power dependence in DBT:DBN

We have tested the behavior of individual emitters to increasing illumination powers of the pump beam. Figure S3.8 illustrates behavior of two emitters (#1 and #2) at three different powers, normalized to the dose of radiation. At  $47 \mu\text{W}$  of pump illumination, the rate of shift change decays in time due to the power law behavior. Increasing of the pump power leads to further increase of spectral shifts and has close-to-linear power dependence. i.e., similar power-law trend is present when the shifts are rescaled to the dose of the pump beam.

### Background fluorescence

Background fluorescence in both DBT:Ac and DBT:DBN originates from fluorescent molecules that are excited with the pump beam. In the latter case, the contribution is largely due to the non-resonantly excited background molecules. The measured signal has close to linear power dependence (Figure S3.9) indicating that we do not reach saturation of background signal at high excitation powers (above  $1 \text{ mW}$ ).

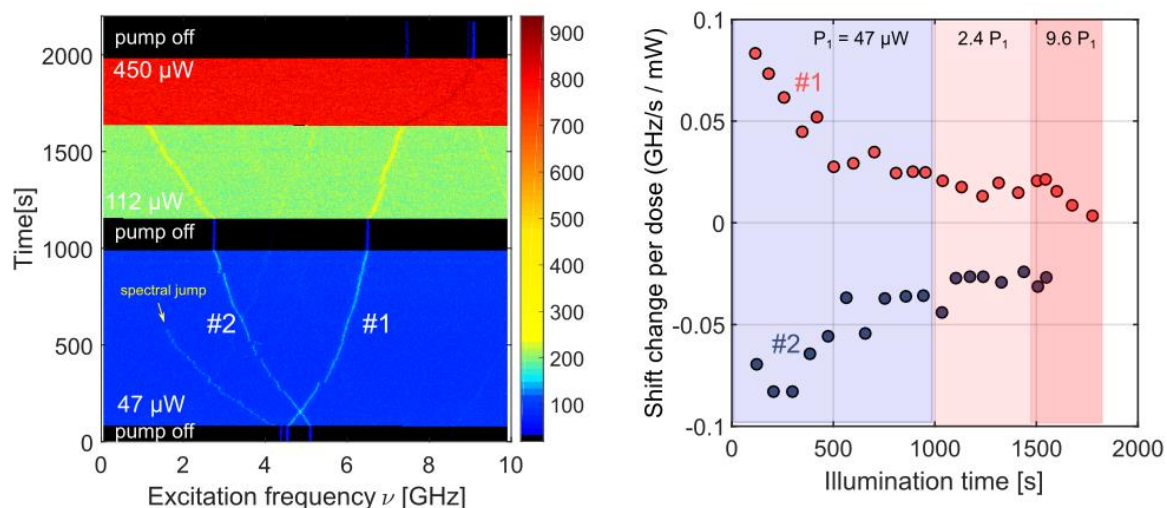


**Figure S3.8:** Left: Single-molecule fluorescence excitation spectrum of DBT molecules in 2,3-DBN recorded in real time with different pump beam excitation powers at 631 nm (47  $\mu\text{W}$ , 112  $\mu\text{W}$ , and 450  $\mu\text{W}$ ). Two stable ZPLs (#1 and #2) are visible showing fairly similar response to the pump beam. The black background in the image indicates line scans without the pump beam. The probe beam was continuously scanned at 756.7 nm (0.7  $\mu\text{W}$ ). Color bar: counts per 5 ms. Right: Shift changes for molecules #1 and #2 shown in the left image, plotted in real time. The color-coded zones denote regions of different pump power. The spectral jump indicated with a yellow arrow may be a signature of a discrete ionization or trapping event.

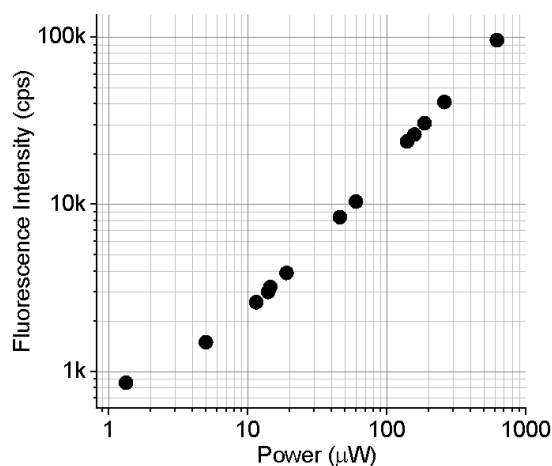


**Figure S3.9:** Fluorescence background signal change with excitation power of the pump beam at 631 nm. The background signal originates from many excited DBT molecules in 2,3-DBN single crystal.

We also observed that spectral shifts can be controlled by changing the polarization of the pump beam, affecting in this way the amount of excited DBT molecules (Figure. S3.10). The largest spectral shifts were obtained for the maximum of fluorescence background signal, proving that larger number of excited DBT molecules leads to greater charge generation and, consequently, larger spectral shifts.

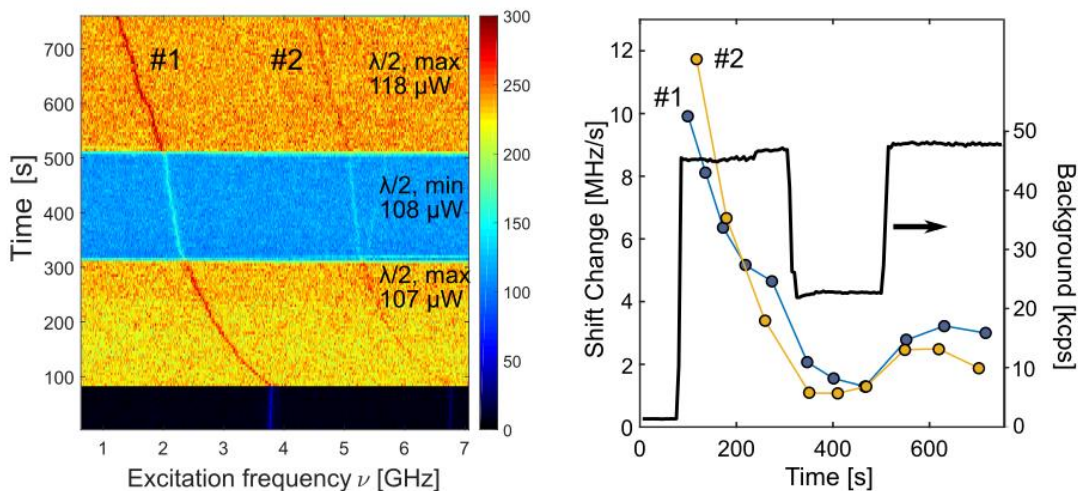


**Figure S3.10:** Left: trajectories of two DBT molecules (#1 and #2) in DBN, whereby the polarization of the pump beam is varied with a  $\lambda/2$  wave plate. The polarization state of the pump beam was adjusted in such a way that the background signal alternated between maximum ( $\sim 47$  kcps) and minimum ( $\sim 22$  kcps). To excite a larger number of molecules, the pump and the probe beam were previously circularly polarized with a  $\lambda/4$  wave plate. Color bar: counts per 5 ms. Right: the average change of the spectral shifts in time for molecules #1 (blue circles) and #2 (red circles).

### Dibenzoterrylene in polycrystalline naphthalene

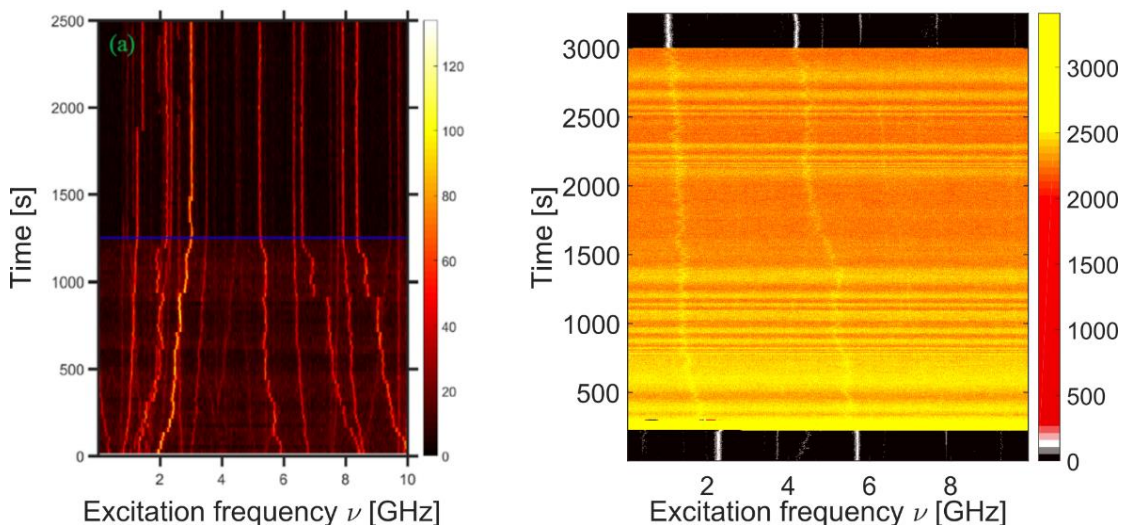


**Figure S3.11:** Tunable spectral shifts of DBT in polycrystalline naphthalene, with pump excitation at 570 nm (left) and 631 nm (right). Color scale counts per 5 ms.

Spectral shifts of DBT in polycrystalline naphthalene can be induced with a pump beam of broad excitation range. In this example (Figure S3.11), we have used a tunable pump laser at several wavelengths in a range of 570 – 635 nm. The ZPLs are photostable (no photobleaching or large spectral jumps) and the spectral shifts obtained are, on average, lower than in DBT:DBN and DBT:Ac systems, typically up to 1 GHz/mW per 1 hour of illumination. Spectral diffusion in this system is also more pronounced, with molecules changing the direction of their shifts in real time. The background signal has oscillating behavior (right panel). This pronounced background time-dependence is most likely due to the change in the



refractive index of a crystal, induced by migration of charges – an effect typically observed in photorefractive materials.

### 3.5.3. Quantum chemistry calculations

Quantum chemistry calculations were done in order to provide information about energies and character of electronically excited states in DBT/DBN and DBT/Ac crystalline systems. Performed calculations required big computer memory and were done by using the TDDFT/B3LYP method with 6-31G(d,p) or 3-21G bases. Theoretical calculations do not guarantee the same precision as the experimental data and thus should be treated with some caution. Calculations of electronic states in studied bimolecular systems (DBT:Ac and DBT:DBN) were performed for Ac and DBN molecules in their real crystal geometries. Embedding sites of DBT in both crystals were already optimized in our previous works.<sup>S3, S4</sup> Different substitution sites led to slightly different energies of the electronic states of DBT molecules embedded in DBN and Ac crystals.

#### Calculations on isolated molecules

Table S1 provides useful information about excitation energies of isolated DBT, DBN, and Ac molecules. The calculated lowest energy transitions ( $\Delta E$ ) agree well with the experimental values. Electron affinities (EA) and ionization potentials (IP) of isolated molecules shown in Table S1 can be used as useful descriptors of electron and hole stabilities, as they determine the polarization energies of created charges in the studied systems.<sup>S5</sup> Based on the values of electron affinities and ionization potentials, the activation energy needed to put the system into a conducting state can be estimated.<sup>S5, S6</sup> According to this empirical description, energy levels of electrons and holes on DBT (i.e., DBT<sup>-</sup> and DBT<sup>+</sup>) will be in between the energy levels of charged host molecules (e.g., Ac<sup>+</sup> and Ac<sup>-</sup>). DBT impurities will thus behave as traps for electrons and holes in both DBN and Ac. Therefore, the activation energy needed to drive the system into photoconducting state will decrease (from, e.g., 3.9 eV for pure anthracene crystal). This empirical interpretation of Karl and Silinsh is confirmed with our quantum chemistry calculations, as elaborated below in more details.

**Table S3.1:** Isolated DBT, DBN and Ac – excitation energies ( $\Delta E$ ), ionization potentials (IP) and electronic affinities (EA). TDDFT/B3LYP/6-31G(d,p) results.

Note that IP (DBT) < IP(Ac) < IP(DBN), and EA (DBT) > EA(Ac) > EA(DBN).

	$\Delta E$ [eV]	IP [eV]	EA [eV]
DBT	1.58	4.30	2.68
DBN	4.25	6.16	1.53
Ac	3.27	5.24	1.65

#### Energies of the excited electronic states of DBT

Energies and oscillator strengths for  $S_1 \rightarrow S_i$  transitions of an isolated DBT molecule were calculated with the aid of the ab initio RHF CIS/3-21G (a convenient method is lacking in the frame of the TDDFT method included in Gaussian 09). It is well known that ab initio methods

give larger values for the transition energies, thus the results of the CIS/3-21G calculations included in Table S3.2 were scaled with factor 1.48. Such procedure led to quite good agreement between the  $S_0 \rightarrow S_1$  transition energies calculated with the aid of both methods and describes well the experimental spectrum. An additional criterion for the sequence of states was their symmetry. Oscillator strengths for the  $S_0 \rightarrow S_i$  transitions calculated by using the CIS/3-21G method were systematically bigger than the corresponding values obtained with the TDDFT/6-31G(d,p) method, but relations between different transitions are similar. Taking into account these observations, we note high oscillator strengths of the transitions  $S_1(\text{Au}) \rightarrow S_4(\text{Bg})$  and  $S_1(\text{Au}) \rightarrow S_7(\text{Ag})$ , with the energies  $\sim 1.3$  eV and  $\sim 1.5$  eV, respectively. Our results are in agreement with the results of calculations described in the work of Sadeq et al.<sup>S7</sup> In conclusion, both states,  $S_4(\text{Bg})$  and  $S_7(\text{Ag})$ , can be involved in the excitation from the  $S_1(\text{Au})$  state, as proposed in our photoionization model which includes CT states (see below).

**Table 3.2:** Energies of excited electronic states of DBT molecule and the oscillator strengths (f) for the  $S_0 \rightarrow S_i$ <sup>S8</sup> and  $S_1 \rightarrow S_i$  transitions.

i	sym	TDDFT/B3LYP/6-31G(d,p)			CIS/3-21G			
		$S_0 \rightarrow S_i$		$S_1 \rightarrow S_i$	$S_0 \rightarrow S_i$		$S_1 \rightarrow S_i$	
		$\Delta E$ [eV]	f	$\Delta E$ [eV]	$\Delta E$ [eV]	f	$\Delta E$ [eV]	f
1	AU	1.584	0.383		1.533	1.105		
2	BG	2.601	0.000	1.017	2.583	0.000	1.049	0.022
3	AG	2.703	0.000	1.119	2.937	0.000	1.404	0.054
4	BG	2.872	0.000	1.288	3.012	0.000	1.479	0.640
5	AU	2.994	0.006	1.410	3.441	0.022	1.908	0.000
6	BU	3.087	0.010	1.503	2.760	0.011	1.227	0.000
7	AG	3.131	0.000	1.547	3.077	0.000	1.544	1.140
8	AU	3.267	0.201	1.683	3.159	0.157	1.626	0.000
9	BG	3.339	0.000	1.755	3.343	0.000	1.810	0.381
10	BU	3.354	0.012	1.770	3.288	0.021	1.755	0.000
11	BU	3.504	0.060	1.920	3.474	0.838	1.941	0.000
12	BG	3.593	0.000	2.009	3.700	0.000	2.166	0.046
13	BG	3.800	0.000	2.216	3.893	0.000	2.360	0.014
14	BU	3.844	0.418	2.260	3.995	0.231	2.462	0.000

### Calculations of locally excited (LE) and charge-transfer (CT) states

In this work, we make a distinction between two types of excited electronic states, which are characteristic for molecular solids and relevant for this work. The electronic excitation of a system with two or more molecules can lead to rearrangement of electronic charges between molecules, creating intermolecular electron transfers, or charge-transfer (CT) states. If such rearrangement of electron density happens intramolecularly, we talk about locally excited (LE) states. The electronic excited states may have also partially LE and partially CT character.

## Electronic states and transitions of bimolecular DBT/DBN system

**Table S3.3:** TDDFT/B3LYP/3-21G results of energies and character of the electronic states in DBT/DBN system, calculated in the real crystal structure geometry of DBN. Red color in the energy levels diagram on the right indicates the contribution of CT character in the presented states. The states CT1 and CT3 are purely CT (DBT→DBN) states. The state CT2 has comparable contribution of the CT and LE characters. Electronic excitations  $S_1 \rightarrow CT2$  and  $S_1 \rightarrow CT3$ , indicated by the red arrows, are supposed to contribute to the transfer of an electron from DBT to the nearby DBN molecule, leaving a hole on the DBT.

i	$\Delta E(S_0 \rightarrow S_i)$ [eV]	f	character of the dominant configuration of the electronic state
1	1.823	0.428	LE(DBT→DBT)
2	2.667	0.001	<b>CT1(DBT→DBN)</b>
3	2.671	0.002	LE(DBT→DBT)
4	2.778	0.002	LE(DBT→DBT)
5	2.843	0.004	LE(DBT→DBT)
6	2.955	0.001	BCT(DBN→DBT)
7	3.030	0.029	LE(DBT→DBT)
8	3.252	0.013	LE(DBT→DBT)
9	3.279	0.008	LE(DBT→DBT)
10	3.375	0.090	LE(DBT→DBT)
11	3.428	0.100	LE(DBT→DBT)
12	3.462	0.021	BCT(DBN→DBT)
13	3.541	0.083	LE(DBT→DBT)
14	3.553	0.030	LE(DBT→DBT)
15	3.618	0.013	<b>CT2(DBT→DBN)</b>
16	3.819	0.001	<b>CT3(DBT→DBN)</b>
17	3.842	0.024	LE(DBT→DBT)
18	3.938	0.149	LE(DBT→DBT)

The lowest-energy electronically excited state of the DBT/DBN system,  $S_1$ , is localized on the DBT component. A sequence of two excitations which would be in agreement with the excitation energies applied in the experiment ( $\sim 2.0$  eV), goes as follows:

1.  $S_0 \rightarrow S_1$ (DBT), energy  $\sim 1.8$  eV, and next
2.  $S_1$ (DBT)  $\rightarrow S_{15}$ (CT2),  $S_{16}$ (CT3),  $S_{17}$ (LE), with excitation energy in range 1.8-1.9 eV.

Also, the nearby  $S_{14}$  and  $S_{18}$  states, attributed in Table S3 to LE states, have some contribution of CT character and thus may contribute to the electron transfer from DBT molecule to the surrounding DBN matrix. All these calculated transitions are within the excitation energy of the pump beam ( $\sim 2$  eV). High excitation powers are needed to excite a DBT molecule from the  $S_1$  state to some higher electronic states with CT character, before the molecules relaxes back to the ground electronic state.

### Electronically excited states of DBT:Ac system

Electronically excited states of DBT/Ac system were calculated for two molecules, DBT and Ac, as well as for a DBT molecule surrounded by 4 molecules of Ac, arranged in the crystal geometry, as shown in Figure S3.12. The results of calculations are collected in Table S3.4 and graphically presented in Figure S3.12. The results for isolated DBT and Ac are also shown in Figure S3.12 for comparison.

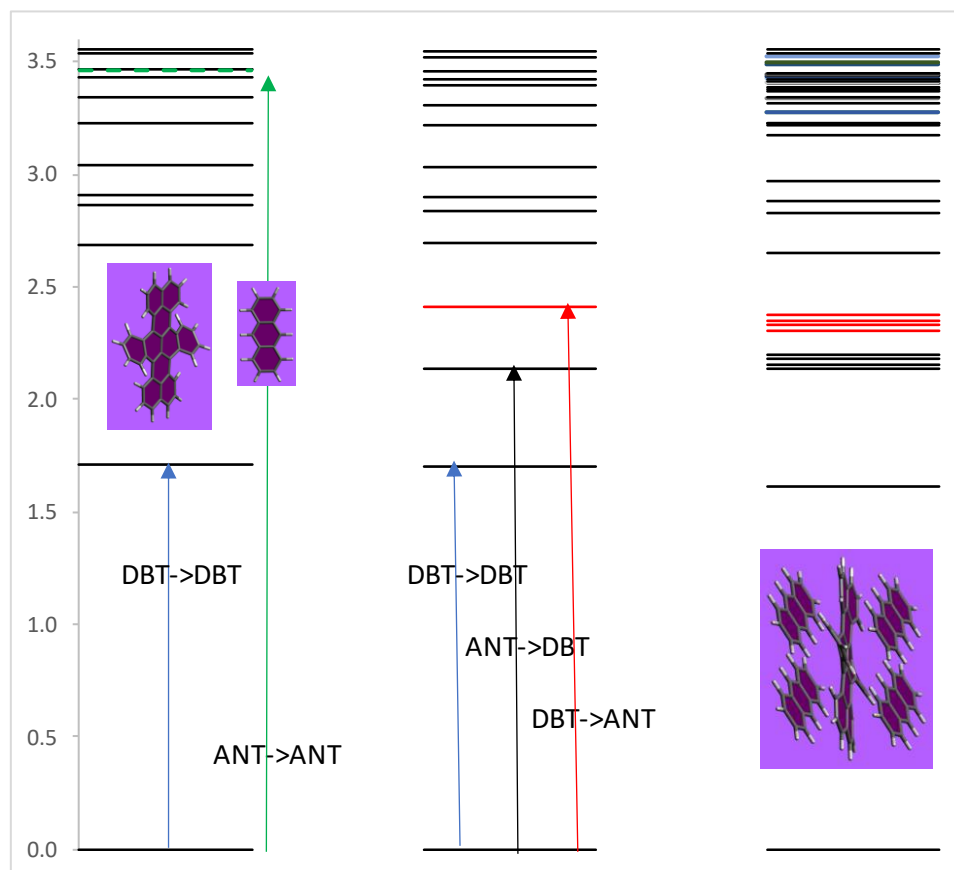


**Figure S3.12:** Diagrams of the electronic excited states of isolated DBT and Ac molecules (left), in the system composed of DBT molecule and one Ac molecule (center) and DBT surrounded by 4 molecules of Ac (right). Numerical data for DBT+4Ac are collected in Table S3.4.



**Table S3.4:** Energies and oscillator strengths of electronic transitions in the system DBT+4Ac molecules. Different colours were used to distinguish transitions with different character. The „band” nature of the states, manifested by several states with similar energy, is a consequence of the presence of 4 Ac molecules.

Type of the dominant electronic configuration	$\Delta E$ [eV]	f
DBT→DBT	1.618	0.281
Ac→DBT	2.139	0.029
	2.142	0.000
	2.188	0.000
	2.202	0.003
DBT→Ac	2.330	0.000
	2.335	0.000
	2.339	0.000
	2.377	0.014
DBT→DBT	2.654	0.000
	2.830	0.000
	2.885	0.000
	2.974	0.003
	3.178	0.001
	3.221	0.000
Ac→Ac	3.225	0.001
	3.227	0.001
	3.279	0.000
	3.281	0.003
DBT→DBT	3.320	0.033
Ac→Ac	3.341	0.000
	3.342	0.000
Ac→Ac DBT→DBT	3.369	0.148
Ac→Ac	3.379	0.000
	3.392	0.013
	3.403	0.000
Ac→Ac Ac→DBT	3.408	0.000
	3.413	0.013
	3.424	0.001
DBT→DBT	3.425	0.050
Ac→Ac	3.438	0.000
	3.444	0.006
	3.448	0.000
	3.450	0.003
	3.489	0.125
Ac→DBT	3.499	0.000

	3.530	0.018
	3.539	0.000
	3.557	0.014
	3.613	0.000
	3.622	0.018
	3.683	0.006
DBT→Ac	3.689	0.000
	3.711	0.000
	3.760	0.059
	3.765	0.000
	3.776	0.021

In the case of DBT/4Ac, the second photon, energy  $\sim 1.6$  eV, following excitation of DBT molecule to its  $S_1$  state (which is located 1.618 eV above the  $S_0$ ), leads to the LE(DBT\*) state of the energy 3.32 eV. This state is immersed in a dense distribution of excited states, described as Ac→Ac. In fact, we observed excited states where change of the distribution of charges following excitation concerns all 4 Ac molecules (see a visual example in Figure S3.13). Vibronic coupling leads to fluctuations of the energies of states, and, consequently, to their mixing. Charge-transfer dynamics was already modeled for the complex pentacene/C60<sup>S9</sup>, where it was based on the coupling of C–C bond-stretching and ring-breathings. Vibronic coupling between the LE(DBT\*) and a manifold of (Ac→Ac) states can be considered as the reason of their mixing and evolution to the charge separated states.

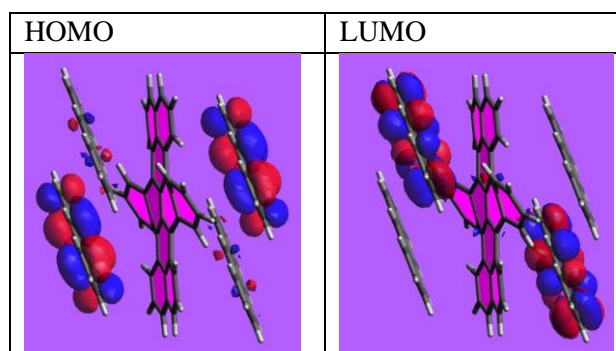


**Figure S3.13:** HOMO and LUMO orbitals for the Ac→Ac transition with the energy 3.279 eV.

The CT states between Ac molecules create charge carriers in Ac matrix, however we have not enough data to discuss this topic in more details.

### Recovery of neutral DBT

Upon excitation of DBT and subsequent electron ejection from DBT and charge transfer to a matrix molecule (DBN or Ac), the positively charged hole remains temporarily on DBT. We have considered the question of the energy barrier between DBT<sup>+</sup>-Ac and DBT-Ac<sup>+</sup> and possibility of hole transfer from DBT to Ac. In this respect, there are two possibilities, i.e., spontaneous filling of the hole and recovery of neutral DBT with the aid of optical excitation.

## Case A: Spontaneous filling of the hole

Our calculations are analogous to polarization energy calculations in organic semiconductors<sup>S10, S11</sup>, and the result is dependent on the number of host matrix molecules taken into consideration. Table S3.5 summarizes calculated energies for different numbers of Ac molecules in the unit cell.

**Table S3.5:** Energies of the systems where DBT is surrounded by different numbers of Ac molecules. Calculations were done with the ONIOM (B3LYP/3-21G:B3LYP/3-21G) method.

Number of Ac molecules	E(DBT <sup>+</sup> -Ac) [au]	E(DBT-Ac <sup>+</sup> ) [au]	$\Delta E$ [eV]
1 Ac	-1988.3167	-1988.2628	1.4652
4 Ac	-3598.0882	-3598.0654	0.6217
36 Ac	-20764.8899	-20764.8888	0.0299

The calculated energy difference in case of DBN–36Ac is small ( $\sim 0.03$  eV). Ionization potential in case of Ac molecule is smaller than the ionization potential of DBN. Similar calculations performed for DBT surrounded by molecules of DBN led to the energy barrier  $\sim 0.9$  eV, an order of magnitude bigger than for Ac.

## Case B: Recovery of neutral DBT with the aid of optical excitation.

**Table S3.6:** Energies of excitation for isolated cation of DBT with 1 molecule of DBN, and with 4 Ac molecules. Calculations performed with the TDDFT/B3LYP/3-21G method.

DBT <sup>+</sup>		(DBT-DBN) <sup>+</sup>			(DBT - 4 Ac) <sup>+</sup>		
$\Delta E$ [eV]	f	$\Delta E$ [eV]	f	character	$\Delta E$ [eV]	f	character
0.927	0.092	1.061	0.006	DBN→DBT	0.472	0.000	Ac→DBT
1.706	0.062	1.245	0.031	DBT→DBT	0.479	0.000	Ac→DBT
1.913	0.256	1.523	0.010	DBN→DBT	0.583	0.022	Ac→DBT
		1.562	0.019	DBT→DBT	0.600	0.000	Ac→DBT
		1.807	0.347	DBT→DBT	1.102	0.055	DBT→DBT
		1.865	0.027	DBT→DBT	1.658	0.054	DBT→DBT
					1.774	0.000	Ac→DBT
					1.778	0.046	Ac→DBT
					1.866	0.084	Ac→DBT
					1.875	0.000	Ac→DBT

In a range of small energies, comparable to the energies of excitation used in the experiment, there are CT transitions, where an electron is transferred from Ac or DBN to DBT.

1.523 eV in the system DBT<sup>+</sup>-DBN

1.778 eV in the system DBT<sup>+</sup>-4Ac

These results suggest that recovery of neutral DBT happens with the aid of optical excitation.

### Consistency of the model with experiments

We verify the consistency of our model with the following experimental observations:

- Illumination by the pump laser shifts the ZPLs almost continuously, and by up to several tens of GHz, with no significant broadening of the optical transition. This is consistent with our hypothesis that charges are trapped relatively far from the probed DBT molecule, so that each single-charge process gives rise to an undetectably small shift of the probed ZPL. The measured shift must result from the accumulation of many single-charge events at relatively large distances.
- The ZPL shift persists for long times, at least 24 h after the pump laser has been switched off. This indicates that the separated charges are far enough from each other that recombination by tunneling remains negligible on hours to days time scales. Such time scales require distances larger than tens of nm.
- The ZPL shift scales sub-linearly with power and can be fitted with a power law of time (eq. 1 of the main text). Power-law kinetics have been observed in the relaxation of charge distributions injected by electrodes in anthracene-based FETs.<sup>S12</sup> This observation supports our assignment of the ZPL shift to slowly varying charge distributions.
- The shift depends only weakly on the pump laser wavelength, with no clear effect of a resonance with DBT levels. This observation supports our assignment to a broad absorption or action spectrum, such as those of excited-state or molecular-ion absorption.
- The shift is observed both on dielectric and metallic substrates, indicating that the charge separation and trapping processes happen in the molecular material itself. The charges are not injected from non-organic materials outside the matrix.

The single-molecule time traces of resonant DBT molecules (Figure 3.1 and Figure 3.2.) give important hints as to local charge dynamics and electric fields. Instead of large discrete spectral jumps, the resonant DBT emitters appear to be continuously shifted for long periods of time by pump exposure. This suggests that many charge carriers contribute to the shift and that the separated charges do not reside in a close proximity of the probed DBT molecules. Furthermore, the long-term stability of the spectral lines after pump illumination points toward long recombination times and low tunneling rates of the charge carriers trapped in the matrix. Assuming the low tunneling rates, we can estimate a lower bound to the distance between separated charges of at least 20 nm.

We first considered direct two-photon excitation of matrix molecules (Ac and DBN) as the possible photoionization mechanism. However, the close-to-linear power dependence of the frequency shift, shown in Figure 3.2.a, rules out single-step, two-photon-induced

photoionization of the matrix. In both types of crystals, we observe background fluorescence whose spectrum shows that it originates from the pump-excited, non-resonant DBT molecules. This background also scales linearly with the excitation power (see SI). Finally, by using linearly polarized pump excitation on a well-oriented DBT:DBN single crystal, we verified that the intensity of the background fluorescence signal correlates with the magnitude of the spectral shift. As DBT cannot be ionized by a single pump or probe photon, we propose that DBT must be ionized via a cascade of two successive single-photon excitations (step A in Figure 3.5). Photoionization results in two charged molecules,  $\text{DBT}^+$  and  $\text{M}^-$  (step B in Figure 3.5). This charge-separated state most likely does not exist for long periods of time. Under conditions of strong illumination, however, both the trapped electron and the hole on DBT are likely to migrate further away into the matrix, creating thus  $\text{M}^-$  and  $\text{M}^+$  species with large separations. This conclusion is in line with our experimental observations. The latter step of photoinduced hole transport regenerates DBT to a photoactive state that can generate further separated electron-hole pairs (step C in Figure 3.5).

Charge separation in the matrix is most likely induced by several background chromophores. These are found in large amounts in the densely doped DBT:DBN crystal, but also in small numbers in the DBT:Ac NCX, e.g. most likely embedded at the nanocrystal surfaces or at imperfections. These background molecules probably exhibit broad optical transitions, thus do not readily appear in high-resolution spectra, and do not significantly affect the anti-bunching measurements. Because these molecules are not necessarily resonant with the probe and probably give rise to very broad optical lines, the process is expected to be nearly independent of the pump frequency, as shown in Figure 3.2.c.

The ZPL spectral shifts can be fitted with power laws, with a faster initial change that slows down in time (Figure 3.2). The spectral shift over time was also explained as consequent to charge transport in the guest-host system.<sup>S13</sup> Similar power-law behavior was reported for co-sublimated DBT:Ac crystals.<sup>S12</sup>, in the presence of hole injection by gold electrodes in contact with the anthracene crystal. These authors observed that charges initially trapped inside the crystal were subsequently de-trapped via migration in the host matrix and tunneling through the dielectric substrate (or via simple charge recombination through a metallic substrate). The similar kinetics in both cases suggests that dispersive transport in the organic matrix is at work in both cases.

It is worth noting that, during the pump illumination, we sometimes do observe small spectral jumps giving rise to noise on top of the power-law trend. These stochastic fluctuations of static electric field might indicate discrete charge hopping events and therefore give an idea of their distance from the probed DBT molecule.

We have also considered other possible mechanisms that may take place during intense laser illumination. While light-induced single-molecule frequency shifts have already been reported in the literature<sup>S14</sup>, the reported relatively weak shifts of about 600 MHz/W were reversible, non-tunable in time, and obtained under significantly stronger pump illumination. The authors ascribed the results to the combination of the beam absorption and ac-Stark effect<sup>S15</sup>. However,

tunable all-optical frequency shifts of single molecules, which persist long after switching off of the pump source, have never been reported for single-photon emitters.

## References

- (1) Hettich, C.; Schmitt, C.; Zitzmann, J.; Kühn, S.; Gerhardt, I.; Sandoghdar, V. Nanometer Resolution and Coherent Optical Dipole Coupling of Two Individual Molecules. *Science* **2002**, 298, 385–389. (2) Pototschnig, M.; Chassagneux, Y.; Hwang, J.; Zumofen, G.; Renn, A.; Sandoghdar, V. Controlling the Phase of a Light Beam with a Single Molecule. *Phys. Rev. Lett.* **2011**, 107, No. 063001.
- (3) Wang, D.; Kelkar, H.; Martin-Cano, D.; Rattenbacher, D.; Shkarin, A.; Utikal, T.; Götzinger, S.; Sandoghdar, V. Turning a Molecule into a Coherent Two-Level Quantum System. *Nat. Phys.* **2019**, 15, 483–489.
- (4) Orrit, M.; Bernard, J. Single Pentacene Molecules Detected by Fluorescence Excitation in a *p*-Terphenyl Crystal. *Phys. Rev. Lett.* **1990**, 65, 2716–2719.
- (5) Basché, T.; Moerner, W. E.; Orrit, M.; Talon, H. Photon Antibunching in the Fluorescence of a Single Dye Molecule Trapped in a Solid. *Phys. Rev. Lett.* **1992**, 69, 1516–1519.
- (6) Lounis, B.; Moerner, W. E. Single Photons on Demand from a Single Molecule at Room Temperature. *Nature* **2000**, 407, 491–493. (7) Nicolet, A. A. L.; Bordat, P.; Hofmann, C.; Kol'chenko, M. A.; Kozankiewicz, B.; Brown, R.; Orrit, M. Single Dibenzoterrylene Molecules in an Anthracene Crystal: Main Insertion Sites. *ChemPhysChem* **2007**, 8, 1929–1936.
- (8) Lettow, R.; Rezus, Y. L. A.; Renn, A.; Zumofen, G.; Ikonen, E.; Götzinger, S.; Sandoghdar, V. Quantum Interference of Tunably Indistinguishable Photons from Remote Organic Molecules. *Phys. Rev. Lett.* **2010**, 104, 123605.
- (9) Rezaei, M.; Wrachtrup, J.; Gerhardt, I. Coherence Properties of Molecular Single Photons for Quantum Networks. *Phys. Rev. X* **2018**, 8, No. 031026.
- (10) Troiani, F.; Ghirri, A.; Paris, M.; Bonizzoni, C.; Affronte, M. Towards Quantum Sensing with Molecular Spins. *J. Magn. Magn. Mater.* **2019**, 491, 165534.
- (11) Tian, Y.; Navarro, P.; Orrit, M. Single Molecule as a Local Acoustic Detector for Mechanical Oscillators. *Phys. Rev. Lett.* **2014**, 113, 135505.
- (12) Lombardi, P.; Ovvy, A. P.; Pazzagli, S.; Mazzamuto, G.; Kewes, G.; Neitzke, O.; Gruhler, N.; Benson, O.; Pernice, W. H. P.; Cataliotti, F. S.; Toninelli, C. Photostable Molecules on Chip: Integrated Sources of Nonclassical Light. *ACS Photonics* **2018**, 5, 126–132.
- (13) Türschmann, P.; Rotenberg, N.; Renger, J.; Harder, I.; Lohse, O.; Utikal, T.; Götzinger, S.; Sandoghdar, V. Chip-Based All-Optical Control of Single Molecules Coherently Coupled to a Nanoguide. *Nano Lett.* **2017**, 17, 4941–4945.

- (14) Rattenbacher, D.; Shkarin, A.; Renger, J.; Utikal, T.; Göttinger, S.; Sandoghdar, V. Coherent Coupling of Single Molecules to On-chip Ring Resonators. *New J. Phys.* **2019**, 21, No. 062002.
- (15) Colautti, M.; Lombardi, P.; Trapuzzano, M.; Piccioli, F. S.; Pazzagli, S.; Tiribilli, B.; Nocentini, S.; Cataliotti, F. S.; Wiersma, D. S.; Toninelli, C. A 3D Polymeric Platform for Photonic Quantum Technologies. *Adv. Quantum Technol.* **2020**, 3, 2000004.
- (16) Aumaitre, C.; Morin, J.-F. Polycyclic Aromatic Hydrocarbons as Potential Building Blocks for Organic Solar Cells. *Chem. Rec.* **2019**, 19, 1142–1154.
- (17) Yang, B.; Trebbia, J.-B.; Baby, R.; Tamarat, P.; Lounis, B. Optical Nanoscopy with Excited State Saturation at Liquid Helium Temperatures. *Nat. Photonics* **2015**, 9, 658–662.
- (18) Wild, U. P.; Güttler, F.; Pirotta, M.; Renn, A. Single Molecule Spectroscopy: Stark Effect of Pentacene in p-Terphenyl. *Chem. Phys. Lett.* **1992**, 193, 451–455.
- (19) Orrit, M.; Bernard, J.; Zumbusch, A.; Personov, R. Stark Effect on Single Molecules in a Polymer Matrix. *Chem. Phys. Lett.* **1992**, 196, 595–600.
- (20) Tamarat, P.; Lounis, B.; Bernard, J.; Orrit, M.; Kummer, S.; Kettner, R.; Mais, S.; Basché, T. Pump-Probe Experiments with a Single Molecule: ac-Stark Effect and Nonlinear Optical Response. *Phys. Rev. Lett.* **1995**, 75, 1514–1517.
- (21) Schädler, K.; Ciancico, C.; Pazzagli, S.; Lombardi, P.; Bachtold, A.; Toninelli, C.; Reserbat-Plantey, A.; Koppens, F. H. L. Electrical Control of Lifetime-Limited Quantum Emitters Using 2D Materials. *Nano Lett.* **2019**, 19, 3789–3795.
- (22) Moradi, A.; Ristanovic', Z.; Orrit, M.; Deperasin'ska, I.; Kozankiewicz, B. Matrix-Induced Linear Stark Effect of Single Dibenzoterrylene Molecules in 2,3-Dibromonaphthalene Crystal. *ChemPhysChem* **2019**, 20, 55–61.
- (23) Fiset-Cyr, A.; Dalacu, D.; Haffouz, S.; Poole, P. J.; Lapointe, J.; Aers, G. C.; Williams, R. L. In-Situ Tuning of Individual Position-Controlled Nanowire Quantum Dots via Laser-Induced Intermixing. *Appl. Phys. Lett.* **2018**, 113, No. 053105.
- (24) Takahashi, M.; Syafawati Humam, N.; Tsumori, N.; Saiki, T.; Regreny, P.; Gendry, M. Local Control of Emission Energy of Semiconductor Quantum Dots Using Volume Expansion of a Phase-Change Material. *Appl. Phys. Lett.* **2013**, 102, No. 093120.
- (25) Grim, J. Q.; Bracker, A. S.; Zalalutdinov, M.; Carter, S. G.; Kozen, A. C.; Kim, M.; Kim, C. S.; Mlack, J. T.; Yakes, M.; Lee, B.; Gammon, D. Scalable in Operando Strain Tuning in Nanophotonic Waveguides Enabling Three-Quantum-Dot Superradiance. *Nat. Mater.* **2019**, 18, 963–969.



- (26) Lombardi, P.; Trapuzzano, M.; Colautti, M.; Margheri, G.; Degiovanni, I. P.; Lo'pez, M.; Kück, S.; Toninelli, C. A Molecule- Based Single-Photon Source Applied in Quantum Radiometry. *Adv. Quantum Technol.* **2020**, *3*, 1900083.
- (27) Pazzagli, S.; Lombardi, P.; Martella, D.; Colautti, M.; Tiribilli, B.; Cataliotti, F. S.; Toninelli, C. Self-Assembled Nanocrystals of Polycyclic Aromatic Hydrocarbons Show Photostable Single-Photon Emission. *ACS Nano* **2018**, *12*, 4295–4303.
- (28) Nicolet, A. A. L.; Kol'chenko, M. A.; Hofmann, C.; Kozankiewicz, B.; Orrit, M. Nanoscale Probing of Charge Transport in an Organic Field-Effect Transistor at Cryogenic Temperatures. *Phys. Chem. Chem. Phys.* **2013**, *15*, 4415–4421.
- (29) Silinsh, E. A. *Organic Molecular Crystals: Their Electronic States*, 1st ed.; Springer-Verlag: Berlin, Heidelberg, **1980**.
- (30) Karl, N. In *Festkörperprobleme XIV*; Queisser, H. J., Ed.; Springer: Berlin, Heidelberg, **1974**; pp 261–290.
- (31) Hoesterey, D.; Letson, G. The Trapping of Photocarriers in Anthracene by Anthraquinone, Anthrone and Naphthacene. *J. Phys. Chem. Solids* **1963**, *24*, 1609–1615.
- (32) Moerner, W. E.; Silence, S. M. Polymeric Photorefractive Materials. *Chem. Rev.* **1994**, *94*, 127–155.
- (33) Stadtmüller, B.; Emmerich, S.; Jungkenn, D.; Haag, N.; Rollinger, M.; Eich, S.; Maniraj, M.; Aeschlimann, M.; Cinchetti, M.; Mathias, S. Strong Modification of the Transport Level Alignment in Organic Materials after Optical Excitation. *Nat. Commun.* **2019**, *10*, 1470.
- (34) Causa', M.; Ramirez, I.; Martinez Hardigree, J. F.; Riede, M.; Banerji, N. Femtosecond Dynamics of Photoexcited C60 Films. *J. Phys. Chem. Lett.* **2018**, *9*, 1885–1892.
- (35) Hahn, T.; Tscheuschner, S.; Saller, C.; Strohriegl, P.; Boregowda, P.; Mukhopadhyay, T.; Patil, S.; Neher, D.; Bassler, H.; Köhler, A. Role of Intrinsic Photogeneration in Single Layer and Bilayer Solar Cells with C60 and PCBM. *J. Phys. Chem. C* **2016**, *120*, 25083–25091.
- (36) Schwoerer, M.; Wolf, H. C. *Organic Molecular Solids*, 1st ed.; Wiley-VCH: Weinheim, **2008**.
- (37) Mallocci, G.; Joblin, C.; Mulas, G. On-line Database of the Spectral Properties of Polycyclic Aromatic Hydrocarbons. *Chem. Phys.* **2007**, *332*, 353–359.

**Supplementary References**

- (S1) S. Pazzagli, P. Lombardi, D. Martella, M. Colautti, B. Tiribilli, F. S. Cataliotti, C. Toninelli, *ACS Nano* 2018, 12, 4295–4303.
- (S2) R. C. Schofield, K. D. Major, S. Grandi, S. Boissier, E. A. Hinds, A. S. Clark, *J. Phys. Commun.* 2018, 2, 115027.
- (S3) A. Nicolet, P. Bordat, C. Hofmann, M.A. Kol'chenko, B. Kozankiewicz, R. Brown and M. Orrit, Single dibenzoterrylene molecules in an anthracene crystal. Main insertion sites, *ChemPhysChem* 8 (2007) 1929-1936.
- (S4) A. Moradi, Z. Ristanovic, M. Orrit, I. Deperasińska, B. Kozankiewicz, Matrix-induced Linear Stark Effect of Single Dibenzoterrylene Molecules in 2,3-Dibromonaphthalene Crystal, *ChemPhysChem* (2019)
- (S5) N. Karl, *Festkörperprobleme IX* 1974, 261–290.
- (S6) E. A. Silinsh, *Organic Molecular Crystals: Their Electronic States*, Springer, 1980.
- (S7) Z. S. Sadeq, Rodrigo A. Muniz, and J. E. Sipe, *Phys. Rev. Materials* 2, 075202 (2018).
- (S8) A. Nicolet, C. Hofmann, M. Kol'chenko, B. Kozankiewicz, and M. Orrit, Single dibenzoterrylene molecules in an anthracene crystal. I. Spectroscopy and photophysics, *ChemPhysChem* 8 (2007) 1215-1220.
- (S9) S. Joseph, M. Kumar Ravva, and J.-L. Bredas, Charge-Transfer Dynamics in the Lowest Excited State of a Pentacene–Fullerene Complex: Implications for Organic Solar Cells, *J. Phys. Chem. Lett.* 2017, 8, 5171–5176.
- (S10) J. E. Norton, J.-L. Bredas, Polarization Energies in Oligoacene Semiconductor Crystals, *J. Am. Chem. Soc.* 2008, 130, 12377–12384.
- (S11) F. Castet, P. Aurel, A. Fritsch, L. Ducasse, D. Liotard, M. Linares, J. Cornil, and D. Beljonne, Electronic polarization effects on charge carriers in anthracene: A valence bond study, *Phys. Rev. B*, 2008, 77, 115210.
- (S12) Nicolet, A. A. L., Kol'chenko, M. A., Hofmann, C. Kozankiewicz, B. & Orrit, M. Nanoscale probing of charge transport in an organic field-effect transistor at cryogenic temperatures. *Phys. Chem. Chem. Phys.* 15, 4415–4421 (2013).
- (S13) Scher, H. & Montroll, E. W. Anomalous transit-time dispersion in amorphous solids, *Phys. Rev. B* 12, 2455–2477 (1975).
- (S14) Plakhotnik T., Walser D., Renn A. & Wild U. P., Light induced single molecule frequency shift, *Phys. Rev. Lett.* 77, 5365–5368 (1996).

- (S15) P. Tamarat, B. Lounis, J. Bernard, M. Orrit, S. Kummer, R. Kettner, S. Mais, T. Basché, *Phys. Rev. Lett.* 1995, 75, 1514–1517.



# 4

## **Single-electron control for optical charge detection**

We first studied in Chapter 2 the Stark effect caused by an external electric field applied to a molecular crystal in direct contact with the electrodes. In Chapter 3, we discussed how light-induced charging processes in the vicinity of DBT molecules lead to a stable Stark shift in the zero-phonon line in three different host matrices. Our initial goal is to scale down charge sensing to its ultimate limits and detect one electron optically. An essential need for this purpose is combining single-molecule spectroscopy and electronic manipulation of single charges. In this chapter, we describe charge quantization and control in single-electron devices, and their compatibility with optical measurements of a single charge is discussed.

## 4.1. Single-electron transfer and control

### 4.1.1. Coulomb blockade

In many electronic devices, the charges flowing under an applied potential are usually considered as non-interacting particles. In contrast to this non-interacting scattering regime, interactions become very important in the so-called Coulomb blockade regime.<sup>1,2</sup> These interactions make it possible to control and manipulate individual charges. The Coulomb blockade regime requires certain conditions that can be discussed in terms of energy, conductivity, and capacitance. To understand when the Coulomb effect takes place, it is necessary to consider how the charging energy and the device properties scale with the dimensions of the device. In the following, we discuss these conditions.

### 4.1.2. Charge quantization and charging energy

Let us simplify the system and consider a tiny metallic island placed somewhere in free space (Figure. 4.1.). This system is assumed to be far enough from any leads that the number of charges inside the island is a constant, integer number.<sup>3</sup> Since the island is metallic, the charges are distributed on the surface of the island and generate an electric field around it. Assume we want to add an extra electron to the island, the electron must overcome this electric field, and this will cost energy. To calculate the energy, we consider the island as a capacitor with electrostatic energy:

$$E = \frac{Q^2}{2C} = \frac{e^2}{2C} N^2 = E_C N^2, \quad (4.1)$$

where  $e$ ,  $N$  and  $C$  are the electron charge, the number of charges and the self-capacitance of the island, respectively. Adding the first electron to a neutral island costs the energy of  $E_C = e^2/2C$  that is known as charging energy.<sup>2-5</sup> The origin of the charging energy is the electrostatic energy stored in the field, and which manifests itself as electron-electron interaction due to charge quantization. The charging energy depends inversely on the island capacitance, itself directly related to the size of the island (see next section for more detail). This means that, in small enough islands, electron charging energy will become dominant and charge quantization will become observable.

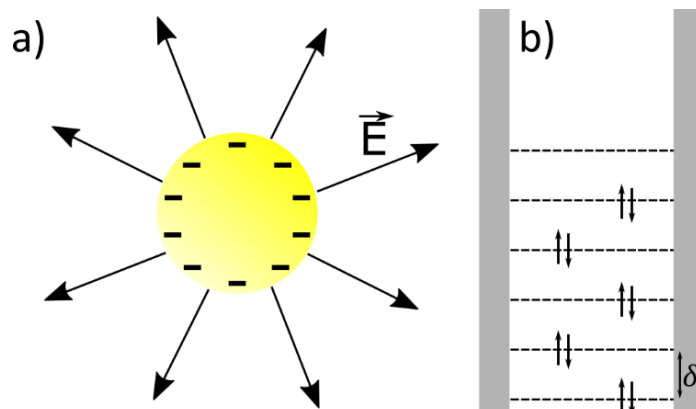


**Figure 4.1:** a) Charges inside a metallic island create an electric field around it which determines the charging energy. b) Quantum effect of energy level splitting inside a finite island. This quantization of energy is only valid in small island such as molecules.

Charging energy is not the only energy that must be considered when charging the island. Quantum mechanics allows us to express the spacing between energy levels inside the island<sup>3</sup> (Figure. 4.1.b). The level spacing at Fermi energy for a box with size of  $L$  scales as  $\delta \simeq \hbar^2/mL^{2.4}$  where  $m$  is the electron mass. This relation states that the level spacing inside the island becomes important for very small nanostructures such as molecules and 2D quantum dots.<sup>1,3</sup> For instance, the energy level splitting in a box with a length of 100 nm is  $\delta \simeq 10^{-10}$  eV whereas the charging energy for the same box is  $E_C = 1.2$  meV. Therefore, for structures larger than molecules, this quantum kinetic energy is often negligible. In the discussions of this thesis, we are not considering the quantum effect and the classical charging energy is the leading the charge states.

So far, the island was isolated and could store a certain amount of charge. To adjust the number of charges inside the island two bulk electrodes can be added to the system. A source electrode is placed close enough to the island that an electron can jump into it. A gate electrode is placed at a somewhat larger distance from the island to tune the electrostatic potential of the island with respect to the source. This configuration is known as a single-electron box. Figure. 4.2 presents the equivalent circuit of a single-electron box.

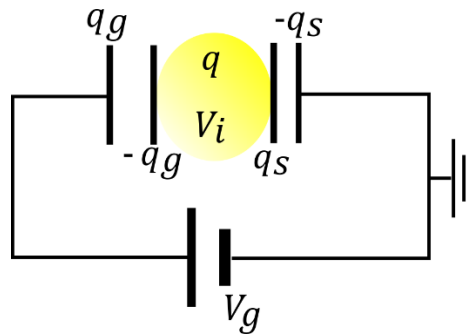


**Figure 4.2.** Equivalent circuit for an island close to two electrodes acting as source and gate.

The charge stored in the island is

$$q = -q_g + q_s = C_g(V_i - V_g) + C_s V_i = C V_i - C_g V_g, \quad C = C_s + C_g.$$

Therefore, the potential in the island follows from an external potential  $V_{ext} = V_g C_g / C$  according to:

$$V_i = \frac{Q}{C} + V_{ext} \quad (4.2)$$

Equation 4.3. shows that the island potential is given by the charge on the island plus the potential induced by the gate. It suggests that the potential of the island, and therefore the number of charges it supports, can be tuned by means of the gate electrode. Note that this potential is not quantized; what is quantized is the charge inside the island.

However, large charging energy is not sufficient to observe clear changes in the charge states of the island. An essential requirement is that electrons do not jump into, or escape from, the

island under thermal fluctuations. This condition is satisfied by ensuring that the charging energy is much larger than the thermal energy:

$$E_C \gg k_B T \quad (4.3)$$

Alternatively, the condition (4.3) is equivalent to demanding that the thermal Johnson noise is much lower than the shot noise due to charge quantization.

### 4.1.3. Self-capacitance of an island

In the previous section, we showed that the charging energy of an island inversely depends on its capacitance. The self-capacitance itself depends on the geometry and size of the island. In this section, we look at the self-capacitance of two simple shapes of islands that could be used to detect a single electron optically, a sphere and a disk island. The capacitance is defined as  $C = Q/V$  and the electric potential  $V$  on the surface of a sphere with the radius of  $R$  that stores charge  $Q$  is  $V = -\int_{\infty}^R E \cdot dR$ . From electrostatics, we know that the electric field is  $E = Q/4\pi\epsilon_0 R^2$ . Therefore, the capacitance for a metal sphere is obtained as follow.

$$C = 4\pi\epsilon_0 R \quad (4.4)$$

In a similar way, the potential of a disk island can be calculated analytically, and we have:

$$C = 2\pi\epsilon_0 R. \quad (4.5)$$

Note that these equations are calculated for the conditions under which the islands are in a vacuum. In practice, the dielectric constant of the environment also enters this equation multiplicatively. To have a feeling of the orders of magnitude of the capacitance as a function of these parameters, we give the self-capacitance for different island sizes and the temperature needed to satisfy charge quantization.

**Table 4.1:** Self-capacitance and maximal thermal energy needed to observe charge quantization, for spherical islands of different sizes.

R	C	$E_C$	$E/k_B$
10 $\mu\text{m}$	$6.3 \times 10^{-15}$ F	12 $\mu\text{eV}$	0.15 K
1 $\mu\text{m}$	$6.3 \times 10^{-16}$ F	120 $\mu\text{eV}$	1.5 K
100 nm	$6.3 \times 10^{-17}$ F	1.2 meV	15 K

### 4.1.4. Barrier

To manipulate the charges inside the island we need electrodes to add/remove electrons to/from the island. We must now estimate how close the electrodes must be to the island and how strong the resistance of the barrier should be. A first condition gives a lower bound for the resistivity of the barrier and is derived from Heisenberg's uncertainty relation  $\Delta E \cdot \Delta t \geq \hbar$ . Let us assume that we have paid the charging energy  $E_C = e^2/2C$  and added the first charge to the island.



The typical time that the charge stays inside the island should be of the order of the classical discharge time of a capacitor,  $RC = C/G$ . To have a well-defined state of an extra electron the uncertainty should not exceed the charging energy.<sup>1,3,4</sup>

$$\frac{e^2}{2C} \cdot \frac{C}{G} \gg \hbar, \quad G \ll \frac{2e^2}{h} = G_Q \approx 10^4 k\Omega \quad (4.6)$$

Where  $G$  is the conductivity and  $G_Q$  is known as quantum conductance<sup>6</sup> and appears when the transmission channel width becomes comparable with electron wavelength. Therefore, to prevent electron leakage from the island, it is necessary to have a barrier with conductivity less than the quantum of conductance. Satisfying this condition is relatively easy. For instance, an aluminium oxide barrier thicker than 1 nm would keep charges long enough in the box to measure quantize charge states.

Heisenberg's uncertainty relation defines an upper bound for the conductance of the barrier. A lower bound for the conductance can be defined by the transmission or tunnelling probability. In quantum mechanics the probability of tunnelling through a barrier for an electron is approximately given by a simple  $P_t = \exp^{-2\beta l}$ , with  $\beta = \sqrt{2m(U_e - E_b)/\hbar^2}$ ,  $l$  is the barrier width,  $m$  is the electron mass,  $U_e$  the electron energy and  $E_b$  the potential barrier. This probability decays swiftly as the barrier length increases. As an example, the probability of tunnelling for a barrier of 2 nm is  $10^7$  times lower than for a 1 nm barrier. A typical tunnelling barrier proper for electrical measurements is between 1 to 3 nm.

#### 4.2. Single-electron transistor

A single-electron transistor (SET) is an electronic device that takes advantage of Coulomb blockade to transfer electrons one by one<sup>1,3,7</sup>. Its structure is similar to the electron box, except that a third electrode (Drain electrode) is added to conduct the tunnelling current (Figure 4.3).

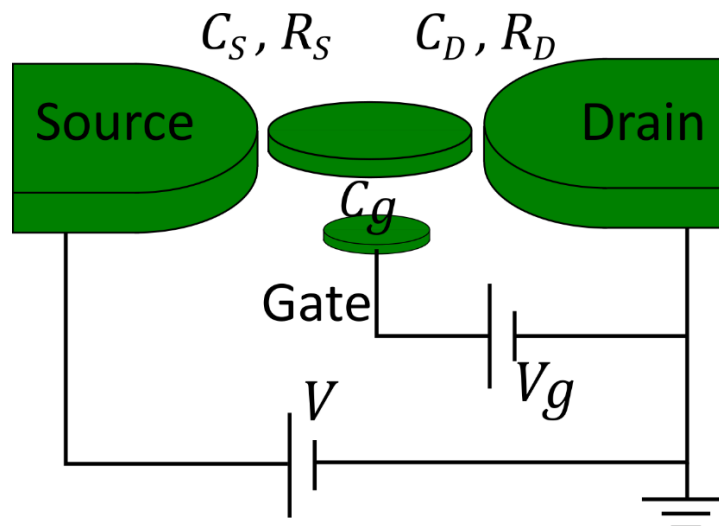


**Figure 4.3:** Schematic view of a SET. Two electrodes (source and drain) are placed near a cylindrical island. The electron tunnels through the tunnelling junction (typically between 1 to 3 nanometre) and enters the islands.  $C$  and  $R$  correspond to capacitance and resistivity of the tunnelling junctions. The island energy can be manipulated with a gate electrode, placed far enough to avoid electron transport through it.

The charging energy in a SET is  $E_C = e^2/2C_\Sigma$  where  $C_\Sigma = C_S + C_D + C_g$ . Similar to the electron box, the charge in the island can be calculated in a classical way:

$$Q = CV_i - C_S V_S - C_D V_D - C_g V_g \quad (4.7)$$

with island potential of  $V_i = V_{ext} + Q/C_\Sigma$  where the external potential is the potential induced by all the electrodes  $V_{ext} = (C_S V_S + C_g V_g + C_D V_D)/C_\Sigma$ . Adding extra electrodes introduces extra capacitance that can be even bigger than the self-capacitance of the island. This extra capacitance therefore reduces the charging energy. This inevitable reduction is the price to pay for full control over the tunnelling current and the number of electrons inside the island.<sup>3</sup>

#### 4.2.1. Current through a SET

The most important feature of SETs for our project, the optical detections of a single charge, is their ability to transmit very low currents and to trap electrons. In this section, we discuss the operation of SETs and we apply this discussion to present our approach for single-charge trapping. Figure 4.4 presents the different working regimes of SETs.

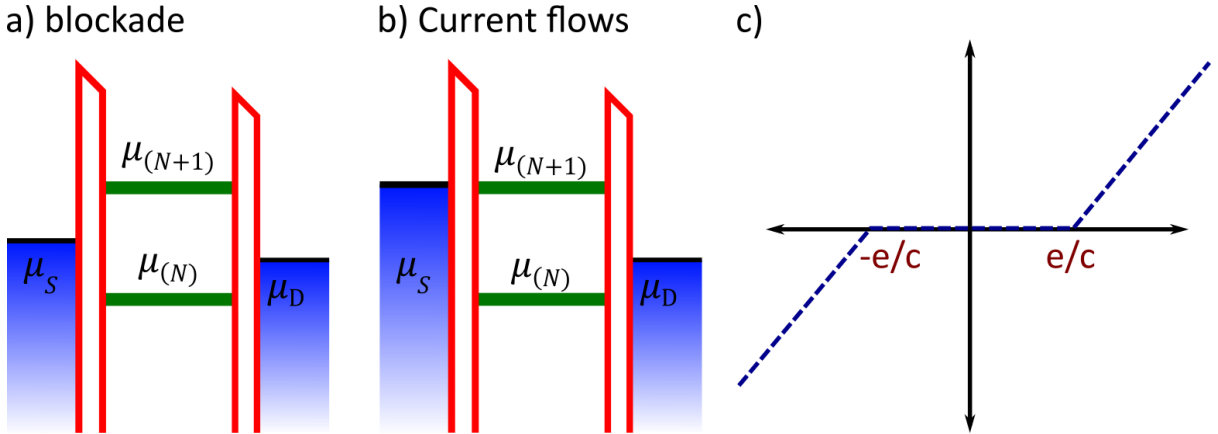


**Figure 4.4:** Working regimes of SETs. a) Charge transfer is blocked. b) current flows. c) Typical IV curve of a SET.

In order to change the charge state of the island, the electron need to overcome the chemical potential.

$$\mu(N) = (N - \frac{1}{2}) \frac{e^2}{C_\Sigma} - eV_{ext}. \quad (4.8)$$

In the Coulomb blockade regime, the electron does not have enough energy to enter the system. Therefore, the number of charges inside the island stays constant. A source-drain bias voltage will increase the electron energy and at  $V = e/C_\Sigma$  electrons reach enough energy to jump into (or out of) the island and current flows. The  $e/C_\Sigma$  value is the maximum threshold and can be suppressed by a gate voltage. Figure 4.4.c shows a typical IV measurement of an SET.

The electron flow becomes more interesting when a voltage is applied to the gate electrode. According to equation 4.8, the number of charges inside the island can be adjusted by the gate voltage. If we draw a 2D map of intensity  $I$  as a function of the source-drain voltage  $V_{SD}$  and

of the gate voltage  $V_g$  the map of Fig. 4.5 follows, which demonstrates the full characteristic of a SET. The white areas in Fig. 4.5 are known as Coulomb diamonds.

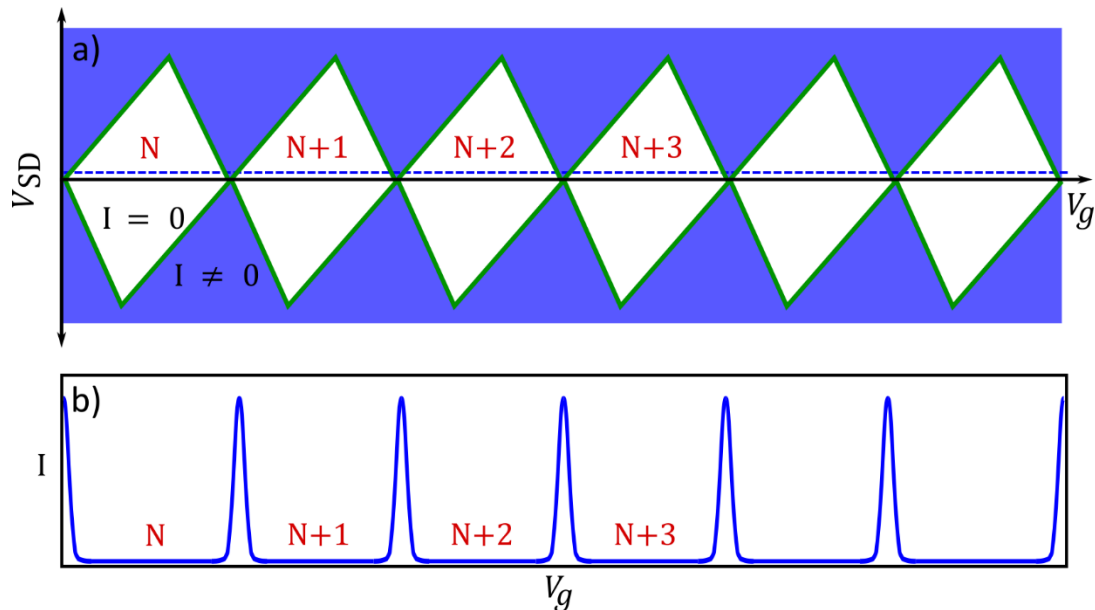


**Figure 4.5:** a) Schematic view of a typical SET characteristic displaying Coulomb diamonds. Note: the skewness is a result of different  $C_S$  and  $C_D$  that always exist due to the imperfect structures. b) Schematic of conductance as a function of gate voltage for low bias voltage.

Figure 4.5.a. is a schematic representation of a SET characteristic with typical Coulomb diamonds. Inside a Coulomb diamond (the white area) the current flow is blocked and the number of electrons in the island is fixed. Outside of the Coulomb diamonds the current flows and the number of electrons inside the island fluctuates.

#### 4.2.2. SETs for optical charge detection

In addition to the physical and electrical requirements for building and operating a SET, the optical charge detection we envision adds its own specific requirements. The most restrictive one is that the SET configuration must create a significant electric field at the position of the molecule. This means that the electric field should not be shielded by the electrodes or any other metallic structures close by. This feature rules out many SET configurations and fabrication recipes that have been successfully applied to electrical detection of Coulomb blockade. Accordingly, we had to develop a novel fabrication method to fulfil the electric-field condition.

The ability of electrical controlling of a single charge offers two approaches to detect a single electron optically.

1. By using SETs as an electron trap in the vicinity of an electric-field-sensitive molecule and electrically manipulate the charges inside the island. Figure 4.5.b shows that the current through the island changes from many tunnelling events ( $I \neq 0$ ) to a blockade state that the number of electrons inside the island is fixed by sweeping the gate voltage. Therefore in a low bias for source and drain and by tuning the gate, the SET can be adjusted in a way that maximum current is passing (on top of the peaks in Figure 4.5.b).

In this case, by slightly detuning the gate voltage the electric state changes. For a DBT molecule in DBN placed in the vicinity of the island the electric field of these states is different and the extra electron in the island can be measured optically by measuring the ZPL's Stark shift.

- Alternatively, a low coupled island to electrodes (island far from electrodes) and without a gate electrode that is easier to fabricate can be used to trap electrons. In this configuration the tunnelling barrier and capacitance need to be adjusted in a way that the tunnelling current be significantly low. As we need to distinguish single-electron tunnelling events through fluorescence changes, we will require long intervals between electron tunnelling events, typically a millisecond or longer. A thicker barrier increases the RC time, i.e., the typical time during which an electron remains localized on the island. In addition to the optical single-electron detection, this configuration enables one to measure extremely low current ( $\leq$  pA) optically that no electrical ammeter can measure. The following table compares the requirements on SETs and low-coupled island for optical detection of a single charge.

**Table 4.2:** Characteristic of SETs and SEBs for optical detection of a single charge

	SET	Low-coupled island
Bias Voltage	$> \mu\text{V}$	$> \mu\text{V}$
Tunnelling Current	$> \text{pA}$	$< 0.1 \text{ pA}$
Resistivity	$> 100 \text{ k}\Omega, \cong 1\text{-}3\text{nm}$	$> 10 \text{ G}\Omega, \cong 5\text{-}10\text{nm}$

### 4.3. Optical detection of an electron by using SET

The DBT/DBN system presented in chapter 2 is an excellent candidate for optical charge detection. In this system, the matrix-induced dipole moment caused a huge Stark shift of about  $1.5 \text{ GHz/kVcm}^{-1}$ . This sensitivity is sufficient to sense the electric field of one electron over 100 nm. COMSOL simulations were applied to map the electric field distribution around an island in a SET configuration. Figure 4.6 presents the electric field around a 100 nm island that is located 3 nm away from two bulk electrodes. Such a configuration is very similar to the SETs fabricated in our lab for single-electron detection and is discussed in the next chapter.

Considering the DBT:DBN system as the molecular probe for the electric field sensing, a field with a strength of only 80 V/cm could be detected. Based on the COMSOL simulation, the electric field of an island charged by one extra electron is around 100 V/cm at 300 nm away from the island. With the DBT:DBN system, this field could be easily detected as a shift in ZPL more than 3 times bigger than its linewidth. Note that in this estimation the molecule's dipole moment is assumed to be aligned along the electric field vector to obtain the maximum Stark shift. In an unfavourable case when the electric field is projected equally on all 4 possibilities of dipole moment orientation in DBT:DBN system and the Stark shift is minimum ( $500 \text{ MHz/kVcm}^{-1}$ , see figure 2.5) still a shift in ZPL, more than its linewidth is expected.

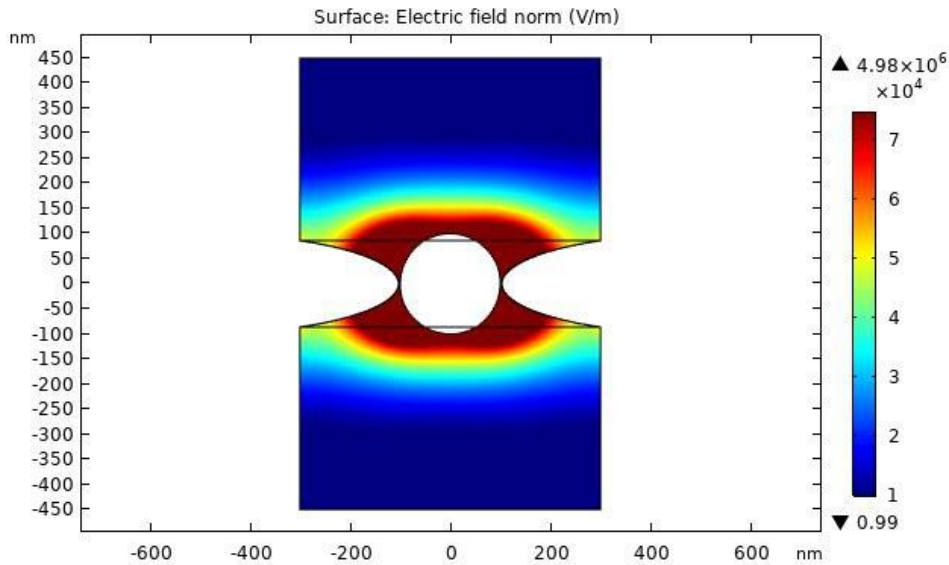


**Figure 4.6:** Electric field distribution around a 200 nm disc island with two nearby contacts.

#### 4.4. Conclusion

In contrast to the normal non-interacting regime for electric current in a resistance, Coulomb blockade is a result of charge carrier interactions. This interaction defines the charging energy of a finite island hanging somewhere in space. If electrons cannot leave or enter the island spontaneously, the charging energy allows us to manipulate the number of electrons in the islands electrically. We provided the conditions for the Coulomb blockade for a 100 nm disk island at a temperature of 15 K or lower. Adding leads and a gate electrode introduce a controllable electron trap with well-defined states with a controlled number of electrons. The electric field induced by adding one electron to the island is detectable by a sensitive molecule in the vicinity of the island as a shift on its optical transition energy (Stark effect). The electric field induced by the added electron was simulated using COMSOL. We showed that by applying DBT:DBN as the molecular probe for charge detection, shifts larger than the molecular ZPL linewidth are expected at 300 nm away from the island. In the next chapter we discuss the fabrication process of the desired SETs.

**References**

- (1) Coulomb Blockade. In *Quantum Transport: Introduction to Nanoscience*; Blanter, Y. M., Nazarov, Y. V., Eds.; Cambridge University Press: Cambridge, 2009; pp 211–298. <https://doi.org/10.1017/CBO9780511626906.005>.
- (2) Molen, S. J. van der; Liljeroth, P. Charge Transport through Molecular Switches. *J. Phys.: Condens. Matter* **2010**, *22* (13), 133001. <https://doi.org/10.1088/0953-8984/22/13/133001>.
- (3) Thijssen, J. M.; Zant, H. S. J. V. der. Charge Transport and Single-Electron Effects in Nanoscale Systems. *physica status solidi (b)* **2008**, *245* (8), 1455–1470. <https://doi.org/10.1002/pssb.200743470>.
- (4) Kastner, M. A. The Single-Electron Transistor. *Rev. Mod. Phys.* **1992**, *64* (3), 849–858. <https://doi.org/10.1103/RevModPhys.64.849>.
- (5) Liao, J.; Blok, S.; Molen, S. J. van der; Diefenbach, S.; Holleitner, A. W.; Schönenberger, C.; Vladyka, A.; Calame, M. Ordered Nanoparticle Arrays Interconnected by Molecular Linkers: Electronic and Optoelectronic Properties. *Chem. Soc. Rev.* **2015**, *44* (4), 999–1014. <https://doi.org/10.1039/C4CS00225C>.
- (6) Silva, P. R.; Nassif, C.; Sampaio, M.; Nemes, M. C. Quantum Conductance and Electrical Resistivity. *Physics Letters A* **2006**, *358* (5), 358–362. <https://doi.org/10.1016/j.physleta.2006.05.043>.
- (7) Chen, R. H.; Korotkov, A. N.; Likharev, K. K. Single-electron Transistor Logic. *Appl. Phys. Lett.* **1996**, *68* (14), 1954–1956. <https://doi.org/10.1063/1.115637>.







# 5

## Single-electron fabrication

In chapter 4 we discussed the role of SETs in single-charge control and trapping. Then we introduced two methods for optical detection of single electrons by using SETs combined with high-resolution spectroscopy on single DBT molecules. It was shown that to use a SET as an electron trap, it must have features that distinguish it from traditional SETs built earlier. The most important aspect is that the electric field created by the charged island should not be screened by any bulk metallic structure. Several fabrication methods were tested to produce favourable SETs for optical charge detection and a fabrication recipe was developed. This chapter describes all the efforts directed at SET fabrication during this PhD work.

A popular method to fabricate SETs is the shadow evaporation technique.<sup>1–6</sup> In this method, the island and electrodes are patterned on a resist with a large undercut (typically a few hundred of nanometre) using lithography, metal deposition and oxidation at different angles, and lift-off. Although shadow evaporation is a well-established technique, the SETs fabricated in this way almost always display an artefact of bulk metal around the main island that would screen the electric field of an electron. It renders this method unfavourable for making SETs for optical charge detection. In the following section, the fabrication processes used in this thesis to fabricate single-electron traps are described in detail. Initially, the fabrication started with e-beam lithography. Later we went through many other techniques such as focused ion beam milling, self-assembly of nanoparticles, and finally, a hybrid method using Atomic Layer Deposition (ALD) combined with e-beam lithography. The detailed description of the equipment used in this project can be found on Leiden University nanolab and Kavli nanolab websites<sup>7,8</sup>.

### 5.1. Electron beam Lithography

In section 4.1.3, it was demonstrated that the charging energy condition can be easily satisfied with an island of 100-300 nanometers at 1.5 Kelvin. This resolution is within reach of conventional electron-beam (e-beam) lithography.<sup>7</sup> In general, creating patterns using e-beam lithography relies on 4 main steps, namely: coating with an e-beam-sensitive resist, e-beam pattern generation, development of the exposed parts of the resist and descum (cleaning of residual resist after development). Those steps are shown in Figure 5.1.

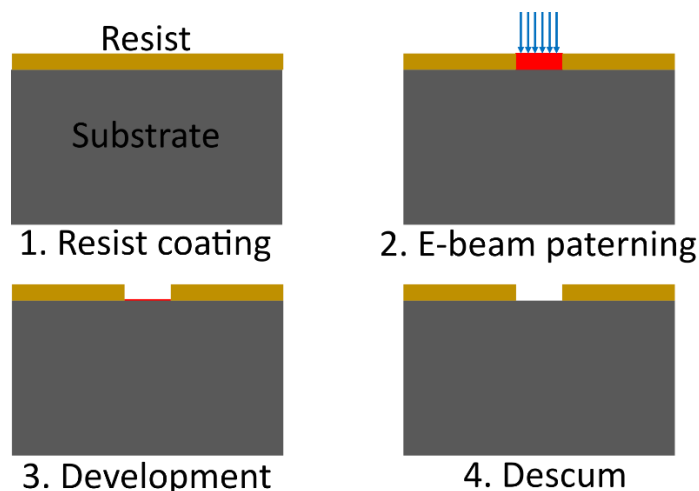


**Figure 5.1:** 4 main steps of e-beam lithography consisting of resist coating, electron beam exposure, developing and descum.

#### 5.1.1. Substrate preparation

All the fabrication in this thesis has been done on silicon (100) wafers supplied by University wafer. This substrate surface had 300 nm wet thermal silicon oxide on the polished side. Such an oxide layer is sufficient to avoid any current leak to the substrate. A diamond cutter was used to cut silicon wafers into squares of  $1 \times 1 \text{ cm}^2$ . The substrates were then flushed with isopropanol and blow-dried with a nitrogen jet to remove silicon grains left from cutting. Then the substrate was stored in boxes with sticky bottom to prevent scratches and damage.

### 5.1.2. Resist coating

After lithography and during metal deposition, there is always some material stuck in sharp corners and against vertical PMMA walls. This normally causes difficulties in lift-off and the formation of ‘flaps’ at the edges of structures (Figure 5.2.a). Bi-layers or multilayers are needed for producing undercut patterns to avoid flap formation and to increase patterning resolution.<sup>9–12</sup> A good undercut pattern consists of at least two layers of resists with different sensitivity. The more sensitive layer is placed between the substrate and the patterned layer (Figure 5.6.b). As a result, during lithography, this layer is overdosed and creates an empty space between the substrate and the pattern. Figure 5.6.a and b show the difference between having and not having an undercut layer. As can be seen, a bilayer undercut produces edges with much better quality and without any flaps.

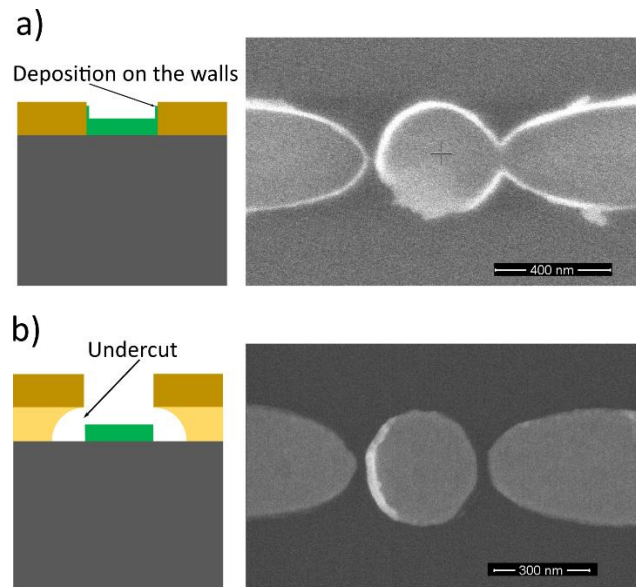


**Figure 5.2:** a) Use of single-layer resist causes flap formation because metal deposition on the walls whereas a bilayer resist b) creates a cavity or undercut between the substrate and the patterning resist that prevents flap formation and produces smooth edges.

The following steps are performed for the resist coating. To create the undercut we have chosen an e-beam-sensitive resist consisting of a double-layer stack out of PMMA 662.06 (600 kDa) and PMMA 672.045 (950 kDa) from ALLRESIST both are positive resists. The following protocol was used to coat the substrate with the resist:

1. Sonicating the substrates in an acetone bath for 2 minutes.
2. Taking the substrate out and immediately flushing with synthesis grade iso-propanol before acetone dries.
3. Blow-drying with nitrogen jet.
4. Mounting the substrate onto the spin-coater using vacuum. Drop-casting PMMA on the substrate with a clean pipet. After transferring the PMMA to the pipet it is better to push the liquid a little bit back into the bottle to avoid bubbles. It is very important to use a small droplet just enough to cover the surface of the substrate. Extra PMMA flows underneath the substrate and causes the sample to tilt on the e-beam stage. The result of this tilt is a change in the focus of the beam and a loss in resolution.

5. Spin-coating of the resist. Start with a spreading step of 1-4 second at 500 rpm followed by 1 minute at 4000 rpm.
6. Baking the resist on a hot plate for 2 minutes at 180°C.

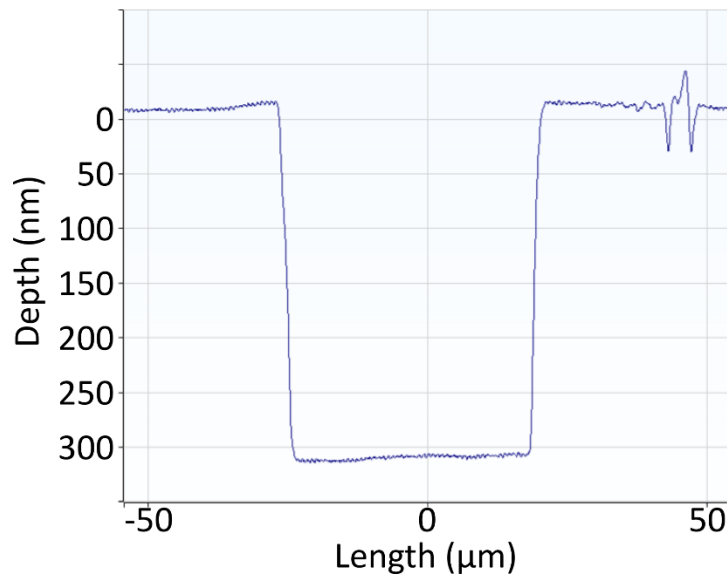


**Figure 5.3:** profilometry measurement of the thickness of PMMA 662.06 (600k) spin coated at 4000 rpm, 60 s and baked for 2 minutes at 180 °C.

First, the PMMA 662.06 was coated on the substrate then PMMA 672.045 was added. Figure 5.3 shows the profilometry data over a cross section of a scratch on coated PMMA 662.06. The 300 nm thickness is in good agreement with the value indicated in the resist datasheet. The thickness of the second layer is 220 nm. The shallow protrusion at the edges is due to the shrinkage of the polymer during scratching.

### 5.1.3. E-beam pattern generator

The electron beam pattern generator EBPG Raith-100 was used. The E-line software was used to design the structures. A small scratch was made in one corner of the substrate before placing it on the device stage (Figure 5.4). This scratch is to define the origin of coordinates and to find it in case of second lithography patterning on the same sample. Also, particles produced during scratching are used as a reference for better e-beam focusing (by making sharp images of those).

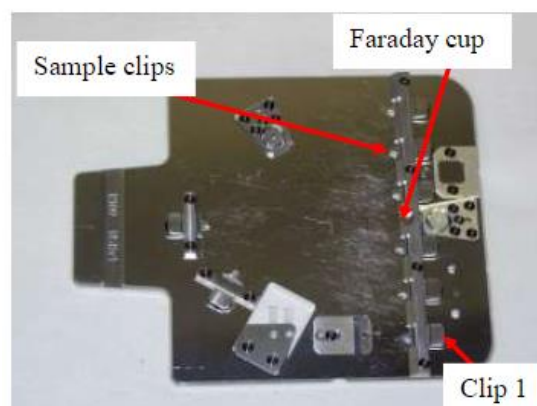


**Figure 5.4:** Sample stage of Raith-100 with 6 different sample clamps with a Faraday cup to measure current and clips to hold the substrate.

The electron exposure using EBPG Raith-100 has several parameters that must be optimized to achieve the best resolution. They are beam-step size, beam diameter, beam current, acceleration voltage and exposure dose. There is a clear link between the resolution and all these parameters, but most of them except for the dose are machine-specific. The optimal exposure dose varies depending on the resist type, shape, and size of the structures. Therefore, it is necessary to perform dose tests. A good starting point for PMMA 672.045, which is the patterning resist here, is  $300 \mu\text{C}/\text{cm}^2$ . After a few rounds of dose test, it was determined that the best dose for writing islands with a radius of 200nm is  $260 \mu\text{C}/\text{cm}^2$ .

In the section 4.1.4 we showed that tunnelling barriers need to be around 1-3 nanometre to have electrically controllable SETs. This resolution goes far beyond the default resolution of e-beam lithography (10-20 nm). However, we tried to break through this limit by using pattern displacement<sup>13</sup> and overdosing. In short, the structures of islands and two electrode tips were repeated many times in an array. Each element of the matrix was slightly different in the dose and the electrode tips position (Figure 5.5.a). The displacements and doses were distributed according to the initial dose tests to cover all possible gaps between electrodes and the islands. Therefore, the desired gap was expected to be formed at least in one of the structures. However, due to the random displacement errors of the beam, the resolution limits of the resist, and the requirement to place two electrodes at the same distance to the island, we could never achieve such a gap in a one-step lithography process. The electrodes were always either touching the island (Figure 5.5.b) or placed too far from it (Figure 5.5.c).

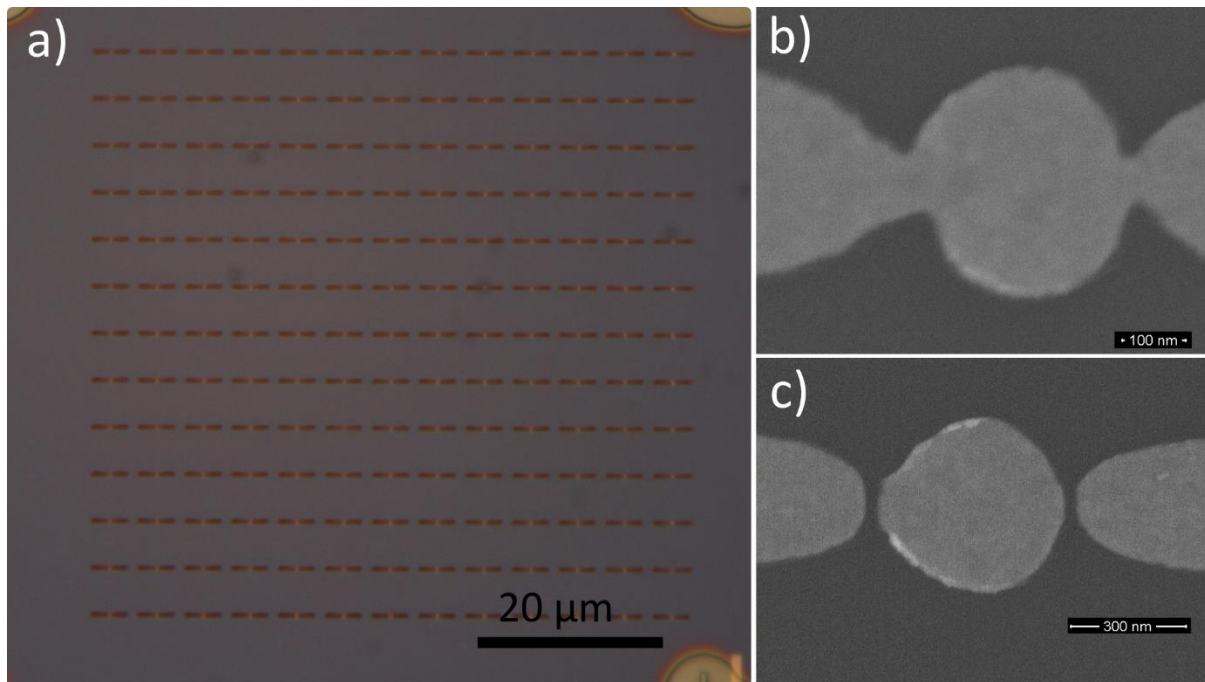


**Figure 5.5:** a) The design of island with shifted electrode tips. The structure is repeated in an array and each copy has different displacement and dose. b) overdosed sample. c) very big gap 20nm.

#### 5.1.4. Development, descum and metal deposition

Samples were developed in methyl-isobutyl-ketone (MIBK): isopropanol (IPA) mixture (1:3 volume/volume) solution at 25°C for 30 seconds immediately followed by flushing with isopropanol. Dry nitrogen jet was used to blow dry sample after development.

To remove all residual PMMA resist in the trenches descum was applied to the sample. During this process, the left-over PMMA are burned out by oxygen plasma. Descum has a significant effect on the surface quality of the deposited layer.<sup>14</sup>

We used e-beam and thermal evaporation systems to deposit metals on the substrate. Pure gold was used to make nanostructures and to increase the adhesion of gold to the substrate (silicon oxide), 2nm Chromium was deposited first then gold with desire thickness was added .<sup>15,16</sup>

lift-off: In nanofabrication, lift-off is a very tricky and important step. In our structure, the most sensitive parts are the tips of electrodes. The tips of the electrodes are very sharp (few nanometers at the tip diameter). This is to have less electric field shielding by electrodes. The sharp tips are very fragile therefore lift-off process must be very smooth. A recopies was developed to have a very clean and safe lift-off without any metal residual.

- The samples were placed in a large beaker containing 100 ml Acetone. A magnetic stirrer was placed inside the beaker and the lid was properly sealed. And placed on the heater.
- The beaker was heated to 40° C while stirring at 200 rpm for 24 hours. Acetone dissolves PMMA and motion flow created by stirring, peels off the gold layer. The size of the beaker permitted for the stirrer to be at a safe distance from the sample
- To ensure the lift-off is done properly, the sample was checked by optical microscope without removing it from acetone bath. Because PMMA is completely dissolved, any remained gold flake sticks to the substrate if acetone dries. The Van Der Waals force is so strong that removing the attached gold flake is impossible considering that any harsh action like sonication damages the sample.
- Remained unwanted gold was removed by flushing the sample with acetone jet while the sample is still inside the acetone bath.

## 5.2. Self-assembly

An alternative way to make SETs is to use self-assembly of gold nanoparticles (NPs) and nanorods (NRs). Formerly, Prof Wilfred Van der Wiel and his colleagues at U. Twente showed that it is possible to grab a NP in between two NRs and to define a tunnelling barrier between those (Figure 5.6). Here the NP is the electron box, and the NRs are used as electrodes to deliver electrons to it (source & drain).<sup>14</sup> The main advantage of this technique is that small NPs (tens of nm) can be used to form an NR-NP-NR configuration. As a result, the charging energy is around 10 meV, which is much higher than the thermal energy at 1.2 K, the temperature we can reach in our cryostat.



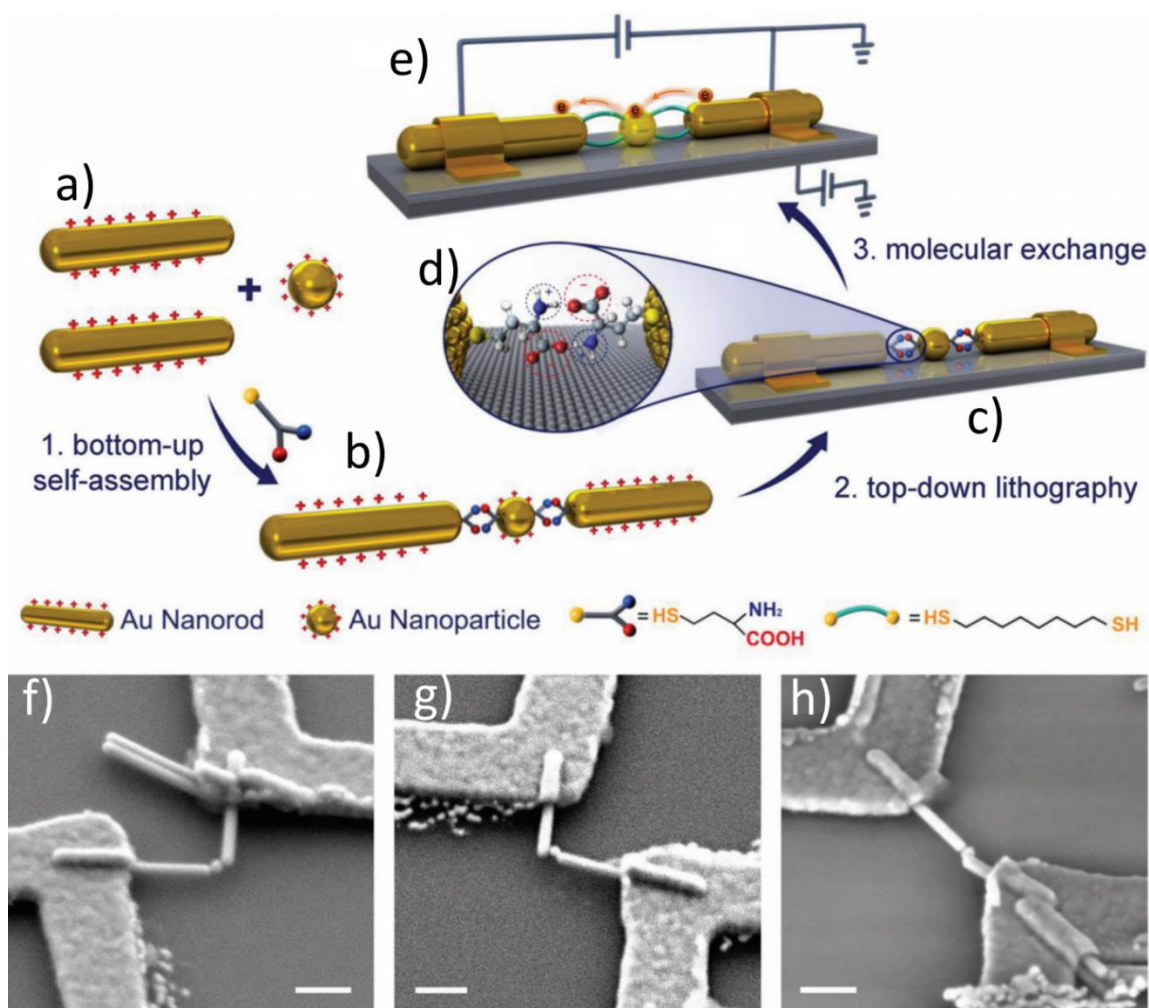


**Figure 5.6:** Process of bottom-up single-electron transistor fabrication based on the self-assembly of NR-NP-NR particles. a) Two Au NRs and a single Au NP (b) self-assembled as NR-NP-NR linked with homocysteine molecules (c) deposition of the assembly on a silicon substrate in order to form a SET and contacting of the assembly with metal electrodes defined by e-beam lithography. d) Final product by an exchange of the linker molecule homocysteine by 1,8-octanedithiol and. f-h) SEM images of representative SETs; the scale bars correspond to 100 nm. <sup>14</sup>

Homocysteine has been used as an electrostatic linker molecule between the NP and NRs (Figure 5.5.d). The thiol group of the homocysteine binds to the surface of the Au NPs and the tips of the NRs. The zwitterionic groups at the NPs and the tips of the NRs attract each other through a two-point electrostatic interaction and NR-NP-NR assemblies take shape (Figure 5.5.b). Similar to what has been done in <sup>14</sup> the following recipe was used to replicate the NR-NP-NR assemblies:

1. 200  $\mu\text{L}$  of 30 nm gold NPs supplied by Vendor company were added to 800  $\mu\text{L}$   $25 \times 10^{-3}$  m CTAB aqueous solution under ultrasonication. The solution was condensed to 200  $\mu\text{L}$  by centrifugation at 10,000 rpm followed by removal of 800  $\mu\text{L}$  of transparent supernatant.
2. 200  $\mu\text{L}$  of the Au NR solution ( $40 \times 150$  nm) was added to 800  $\mu\text{L}$   $25 \times 10^{-3}$  m CTAB under ultrasonication. Then it was centrifuged at 6000 rpm for 6 min, and 960  $\mu\text{L}$  of the transparent supernatant was removed followed by the addition of 160  $\mu\text{L}$  of Milli-Q water.

3. 2  $\mu\text{L}$  of  $1 \times 10^{-3}$  M homocysteine solution and 2  $\mu\text{L}$  of Au NPs solution were added to the NR vial.
4. After 24 hours the solution was drop-casted on a silicon substrate. Note that in the work in reference 14, 120 minutes for the formation of NR-NP-NR assemblies is mentioned. But we did not observe any assemblies after 120 minutes.
5. The substrate was dried with a nitrogen jet.

In scanning electron microscopy (SEM) imaging, different combinations of NP-NR assemblies were observed. As can be seen in the images of figure 5.6, in addition to the desired NR-NP-NR (figure 5.7.a), other assemblies like necklace of NRs (figure 5.7.b) and NP-NR-NP (figure 5.7.c) are also formed.

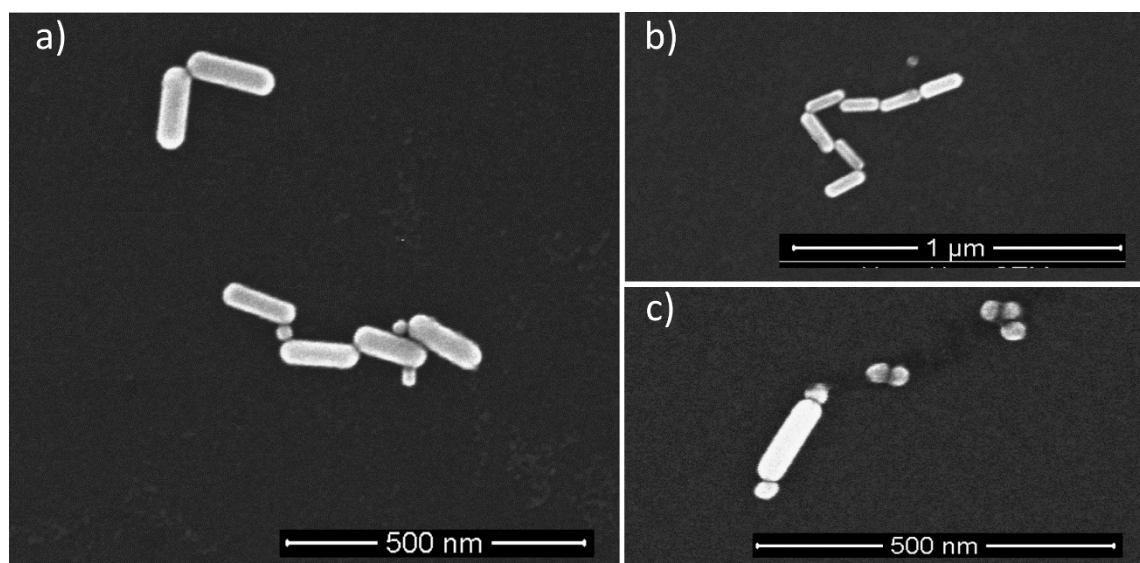


**Figure 5.7:** a) Self-assembly of the desired combination of a) NR-NP-NR and also other combinations of (b) necklace of NRs and c) NP-NR-NP

The next step in making SETs is to transfer the assemblies to find the desired assemblies on the substrate and connect them to the contact pad. Unfortunately, the clean-room facilities of the Leiden University would not permit the later steps of this fabrication, which prevented us from continuing our work on this project. However, until the time of writing this thesis, we kept on collaborating with Professor van de Wiel's group to proceed with this approach.

### 5.3. Hybrid recipe to make SETs

In section 5.1 we showed that single-step e-beam lithography alone is not appropriate for making the barriers. However, it is possible to define the barrier by using e-beam lithography along with oxide deposition.<sup>15</sup> Generally, this method consists of three main steps. First, the islands are written on a substrate. Then, they are covered with a layer of insulator (Aluminium or Silicon oxide). Finally, the electrodes are added in such a way that they slightly overlap with the island. The oxide layer isolates the islands, defines the tunnelling barrier, and at the same time simplifies the alignment of the contacts to the island. Figure 5.8 shows the overall process. The main challenge of this approach is to accurately define the thickness of the insulator layer.



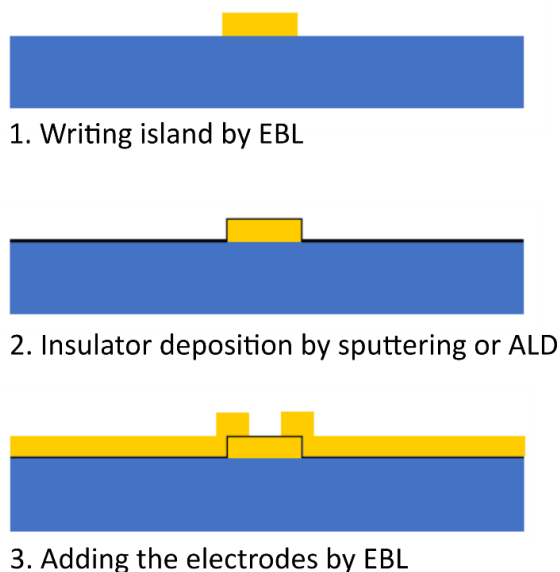


**Figure 5.8:** General overview of the hybrid method consisting of 3 main processes: 1. Patterning the island by EBL. 2. Covering the island with an insulator layer such as  $\text{SiO}_2$  or  $\text{Al}_2\text{O}_3$  by sputtering or ALD. 3. Patterning the electrodes.

One way is the deposition of thin films on the surfaces by sputtering. During sputtering a source material (target) is bombarded with accelerated ions. The energetic ions tear off target atoms or molecules as either individual atoms or clusters of atoms or molecules. The ejected particles land on the surface of the sample and coat it with a thin film. The thickness distribution of the coated films depends on the angular distribution of sputtered particles, on the collisions between sputtered particles and gas molecules, and on the shape of the target.<sup>16</sup> Because of the particles' collisions and scattering, the coated layer covers both vertical and horizontal surfaces. The ratio between horizontal and vertical deposition strongly depends on the distance between the sample and the target.<sup>16</sup> For the sputtering device available at Leiden university<sup>7</sup> this ratio is measured to about 30% for silicon oxide. Therefore, in order to achieve a tunnelling barrier of 1 to 3 nanometre on sides of the disk shape islands, a silicon oxide layer of 4 to 10 nanometre is needed.

Electrical measurements showed that sputtering is not a reliable method in making barriers. The non-uniformity of the sputtered film in thin layers causes either short cuts or excessive resistivity in the samples. Another disadvantage of sputtering is the instability of the sputtering rate. It makes optimizing the coated layer almost impossible. Also, silicon oxide in thin film is not a good insulator and often causes leakage due to pinholes.<sup>17</sup> Therefore, we abandoned the approach of sputtering silicon oxide and sputtering and considered alternative methods with more precise control over the thickness.

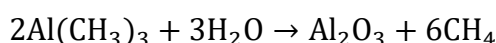
### 5.3.1. Atomic Layer Deposition

Atomic layer deposition (ALD) is a technique for thin film deposition with atomic precision control over the thickness. The process of ALD is based on vapor chemical process in which a thin film grows layer by layer. Each layer consists of a two-dimensional layer of single atoms or molecules. In each individual layer the substrate is exposed to a pulse of precursors molecules in vapor shape. The precursor molecules react on the surface of the substrate in a self-limit manner. The reaction stops as soon as all the reaction sites on the surface are full.

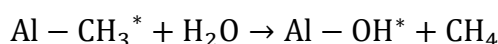
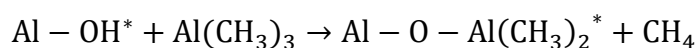
Therefore, a single atomic size layer with no overlap forms. A thin film can be grown by repeating the reaction process. In addition to the uniform film over whole sample surfaces, ALD provides precise control over the thickness (atomic size). ALD has been used to deposit many materials <sup>21</sup> and has found wide variety of applications in research and industries. These unique features suggest ALD as an excellent method to make the barrier.

Unlike silicon oxide, aluminium oxide provides better electric insulation in thin layers. It is hard and stable with good adhesion to many surfaces. Also, it has high electrical resistivity ( $\sim 10^{-16} \Omega$ ) and small dielectric constant in thin film (around 3 for a few nanometre). This makes it suitable for barrier fabrication.  $\text{Al}_2\text{O}_3$  has been used previously as tunnelling barrier in <sup>1-5</sup>. We used ALD to coat the fabricated island and to create a tunnelling junction between the electrodes and the island.

A common reaction for aluminium oxide deposition by ALD is based on the following chemical vapor deposition (CVD) reaction <sup>20</sup>.



In ALD this reaction is performed in two half-reactions. <sup>20-24</sup>



To deposit  $\text{Al}_2\text{O}_3$ , at first, a sample is exposed to trimethylaluminum (TMA), which would react with hydroxyl groups on the surface. This reaction proceeds until all the surface reaction sites are full. Subsequently, TMA is pumped away. The same process is then performed with  $\text{H}_2\text{O}$ . The  $\text{H}_2\text{O}$  reacts with methyl groups on the surface until this surface reaction reaches completion. <sup>22</sup> The time for each cycle is around 12 seconds and the thickness of each layer is about 1 Å. These cycles are repeated to achieve the desired film thickness.

To deposit  $\text{Al}_2\text{O}_3$  we used the Oxford ALD device of the Kavli lab at TUDelft. The device can operate at different temperatures from 20 to 500 °C. It has been shown that gold nanostructures at high temperatures deform and even can penetrate the substrate. <sup>25</sup> To avoid any possible damage to the sample, the device was operated at 105°C.  $\text{Al}_2\text{O}_3$  was deposited on several samples, each with a different number of cycles. Each batch of samples loaded into the ALD machine was accompanied by a bare silicon substrate as a control. This piece was used to measure the thickness of the coated layer using the ellipsometry technique. Based on the ellipsometry data the deposition rate is estimated to about 0.6 Å per cycle. A larger error of around 2 Å has been observed for the first 10-12 cycles due to the measurement errors in a very thin film, or alternatively because of the inhomogeneities in concentrations of the precursors during the first cycles of the deposition. Figure 5.9 shows the thickness of the deposited layer as a function of the number of cycles.

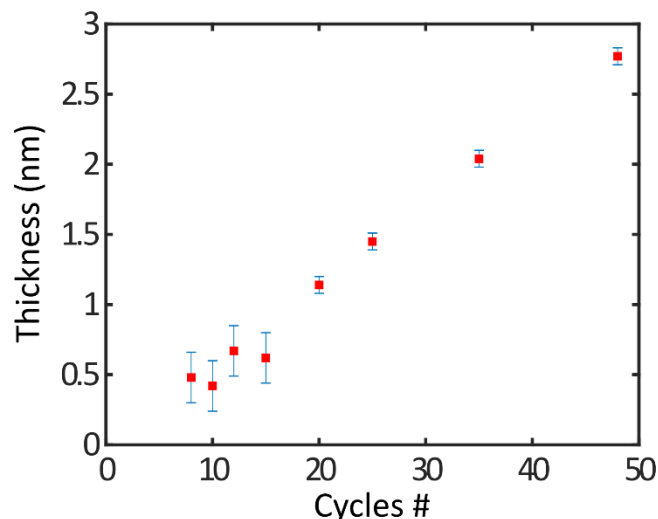


**Figure 5.9:** Thickness of  $\text{Al}_2\text{O}_3$  for versus ALD number of cycles measured by ellipsometry.

### 5.3.2. Final recipe for making SETs

Finally, we have settled on a 10-step hybrid fabrication method that yielded the desired SETs. This method consists of e-beam lithography, gold deposition and ALD. The E-line software was used to draw the structures. Each component is defined in a different layer, allowing us to print them in separate steps. To find writing parameters (dose, beam spot size and beam speed) for the layers, many different tests have been performed. The most critical part of the design is the electrode overlap with island, after 9 round of lithography each round on a chip with 450 SETs, the best shift for the electrodes in respect to the island and the proper dose was found.

In a nutshell, the fabrication recipe consists of 3 lithography steps to pattern the island, make the electrodes, and finally connect these electrodes to the contact pad. Atomic layer deposition was used to insulate the island and to create the tunnelling junction. The final protocol was executed in sequential steps as follows.

1. E-beam lithography to fabricate the islands:
  - Two layers of PMMA resist (662.06-600k and 672.045-950k) were spin coated on the substrates as explained in section (5.1.2).
  - A matrix of  $15 \times 15$  individual 200 nm islands separated by 5  $\mu\text{m}$  from each other were patterned by Raith-100 e-beam lithography. The islands were written with a beam spot size of 32 nm (PC 14) and a dose of 220  $\mu\text{C}/\text{cm}$ .
  - In order to find the structures back during the second and the third steps of lithography, e-beam markers were also patterned in this stage. The suitable dose to write a marker was 360  $\mu\text{C}/\text{cm}$ , which provided a beam spot size of 32 nm.
  - Samples were developed in mixture of methyl-isobutyl-ketone (MIBK) and isopropanol (IPA) (1:3 volume/volume) at 25°C for 30 seconds, immediately followed by flushing with isopropanol.
2. Deposition: 2 nm of Chromium and 20 nm of gold were deposited by a resistance evaporator.
3. Lift-off: was done based on the recipe described in section 5.1.4. Figure 5.10 shows one of the fabricated islands with a diameter of about 200 nm.

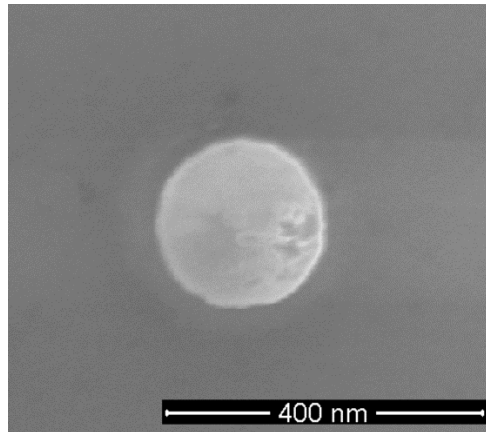


**Figure 5.10:** 200 nm gold island patterned by e-beam lithography and deposited by the resistance evaporator technique.

4. Insulation: ALD was used to deposit  $\text{Al}_2\text{O}_3$  with various thicknesses (from 0.6 to 4.2 nm) to electrically insulate the islands.
5. E-beam lithography to fabricate the electrodes: Raith-100 EBPG has an alignment error of up to 50 nm in overlapping two layers printed in two different steps. Previously, it was mentioned that many islands were printed in a matrix. For each element of this matrix the electrodes were displaced with respect to the center of the islands. Repeating this displacement in all directions allowed us to compensate for the alignment error and end up having several perfect structures somewhere in the array. Moreover, to select for the optimal dose, the dose was also varied up to twice bigger than the original value. This would increase the chance of getting the desired overlap between tips of electrodes and island. The procedure for making source and drain electrodes was therefore very similar to the one used for fabricating the islands:
  - Two layers of PMMA resist (662.06-600k and 672.045-950k) were spin coated on the substrates.
  - The electrodes were patterned with a beam spot size of 89 nm (PC 10) and a basic dose of  $300 \mu\text{C}/\text{cm}$ .
  - Samples were developed in MIBK:IPA 1:3 mixture at  $25^\circ\text{C}$  for 30 seconds immediately followed by flushing with isopropanol.
6. Gold deposition: Initially, 25 nm of gold were deposited at this stage. Later, we found that electrode tips often crack at their overlaps with the island (Figure 5.11). A possible explanation is the height difference between the island and the substrate. This difference creates a shadow during evaporation in case the sample is slightly tilted. As a result, the electrode at the edge of the island disconnects or is thinner and can easily break. To avoid this problem, we found it better to deposit a thicker second layer, with a thickness of at least 1.5 times that of the first layer. At the end, 2 nm Chromium followed by 30 nm of gold were deposited on the substrate.

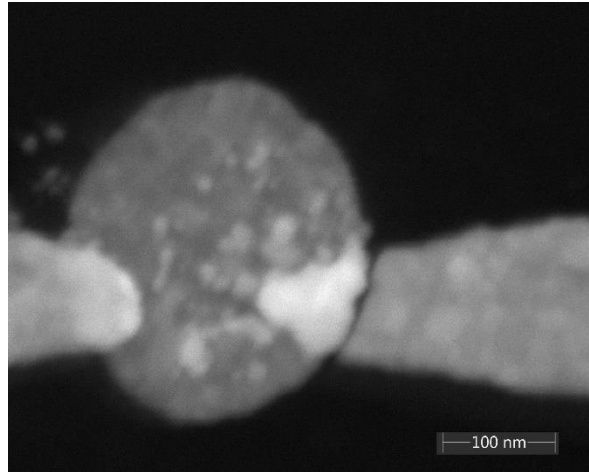


**Figure 5.11:** A crack in the tip of an electrode caused by insufficient electrode thickness.

7. An SEM (Thermo Fisher Scientific Apreo 2) was used to image the samples and to measure the intersection to calculate the  $C_S$  and  $C_D$  capacitances. The charging energy depends on this intersection area. Larger intersection areas increase the total capacitance and consequently decrease the charging energy. Considering this limitation and the self-capacitance of the island, the total capacitance of  $C_S$  and  $C_D$  should not exceed 100 aF. SEM imaging is known to be destructive to the inspected samples due to charging and carbon contamination deposited on the sample. To mitigate these effects the sample was plasma cleaned before inserting it into the SEM and each batch of SETs had an extra twin set to be used for imaging. Figure 5.12.a, b, and c show three examples of fabricated SETs with the desired overlap, a too large overlap, and no overlap, respectively.

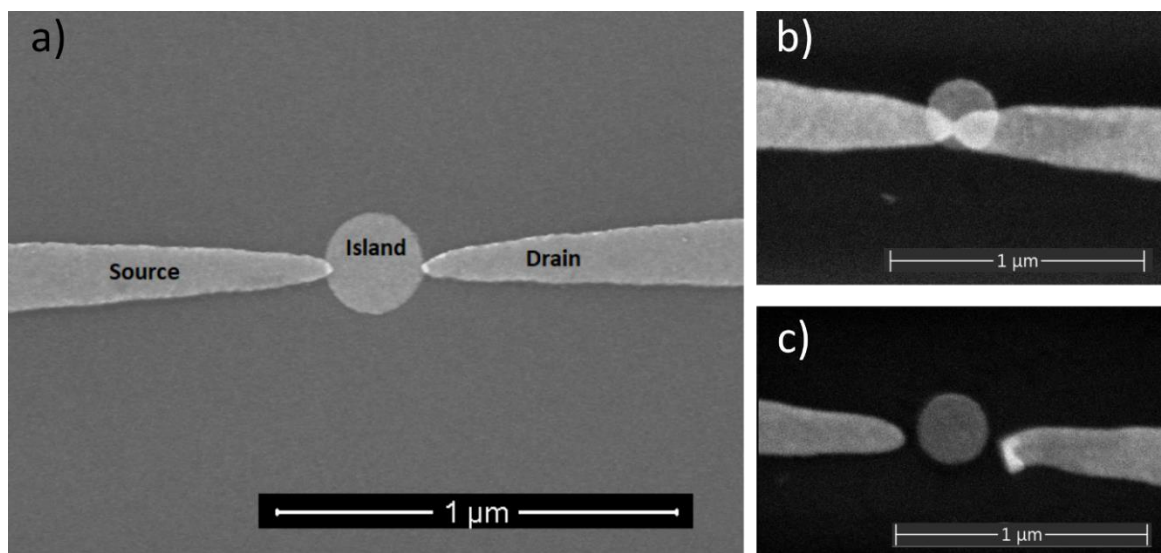


**Figure 5.12:** Fabricated SETs with different doses and shifts for the electrodes. a) desired intersection between island and electrodes, less than  $800 \text{ nm}^2$ , resulting in  $C_S + C_D$  less than 100 aF. b) over-exposed sample with a too large overlap and short contact between electrodes. c) no overlap.

8. E-beam lithography was used to connect well-fabricated SETs to  $200 \times 200 \text{ μm}^2$  contact pads using a dose of  $280 \text{ μC/cm}$  and a beam spot size of 800 nm (PC 1).
9. 2 nm of Chromium were deposited as adhesion layer followed by 50 nm gold using the resistance evaporation technique. The contact pads were chosen to be thicker because

during wire bonding, the wire penetrates at least 30nm into the pad. The extra thickness is needed to prevent the wire from reaching the silicon and leaking current to the silicon substrate.

10. Lift-off was done based on the recipe described in section 5.1.4. Figure 5.13 shows the final product.

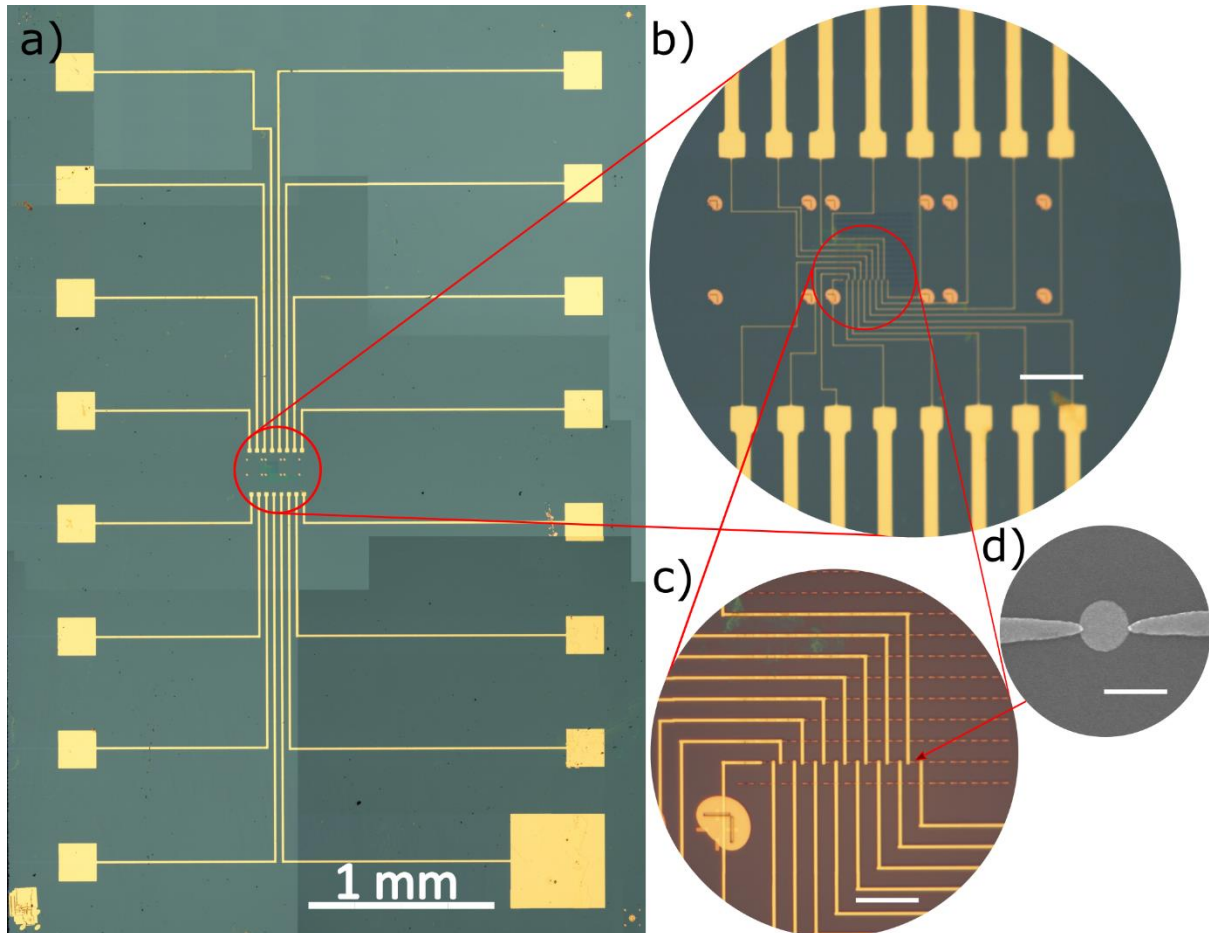


**Figure 5.13:** Final product of our hybrid recipe to fabricate SETs. a) An overview of the fabricated electronic chip with 16 contact pads to connect 8 SETs. b) A 20 times zoom-in image to the region that the big contact pads connect to the microstructures, scale bar 50  $\mu\text{m}$ . c) A 100 times zoom-in to the region that SETs are located and the SETs are connected to the bigger structure with 500 nm width leads, scale bar 10  $\mu\text{m}$ . d) An SEM image of a desired SET, scale bar 250 nm.

#### 5.4. Sample storage and transport

Since the SET samples rely entirely on tiny nm-sized gaps between the electrodes and the island, they are prone to disastrous damage through dielectric breakdown. Therefore, these samples are extremely sensitive to stray electrostatic charges.

In order to reduce the risk of damage, the following protocol was always carefully followed, as a single mistake can ruin days of work:

- Samples were coated with Electra92 (Allresist) conductive polymer immediately after the final lift-off. Electra 92 resistivity is  $1\Omega/\text{m}$ . it creates a parallel circuit to the transistors with much less resistivity. This parallel circuit

makes equal electric potential between any two points of the sample and transfers incident stray charges safely.

- We always wore a wrist strap connected to the ground while working with the sample.
- Any unnecessary insulators were removed from the working desk.
- Extreme care was taken to avoid any contact with the chip leads.
- The sample was kept in a box with a sticky bottom to prevent it from moving around.
- The sample box was sealed with a static shielding bag during transportation.

Despite all these precautions, many samples were damaged during transportation or preparation. Figure 5.14 shows some examples of these damages. It is almost impossible to know when and how the damages occurred. The only reliable solution is taking absolute care during sample transportation and preparation.

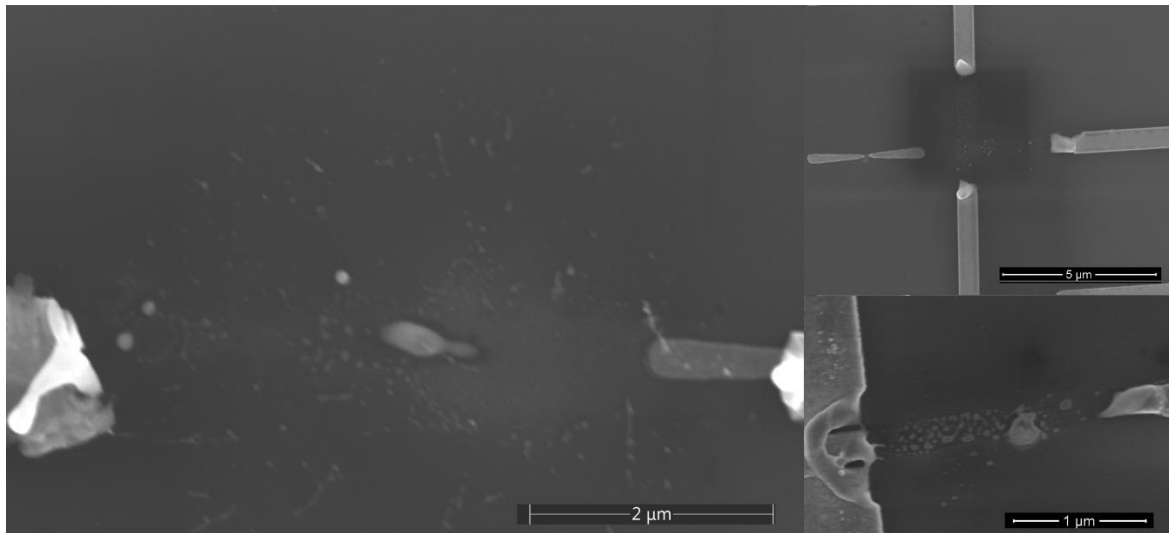


**Figure 5.14:** Some examples of samples damaged by static electricity.

### 5.5. Electrical measurements

At the early stages of the project, the electrical measurements were done in Leiden. The sample was wire-bonded to a printed circuit board and attached to the cryostat insert. The cryostat used for electrical measurement is an Oxford instrument Teslatron closed-cycle cryostat that was purchased by the Leiden University condensed matter section within the Nanofront program. Then current-voltage measurements were acquired by the Keithley source-meter model 2450SMU. The measured I-V characteristics, unfortunately, did not display the expected behaviour for SETs, due to damage or to current leakage. Later, SEM images revealed that all measured samples at this stage were damaged. The tip of the electrodes melted in all SETs and the tunnelling barrier was destroyed. SEM images of the sample taken after each step from preparation to measurement revealed that the samples were damaged during the measurement. Figure 5.15 presents some of the damaged samples. To overcome this problem, the set-up was refurbished so that the risk of damaging the sample was minimized. The electrical measurements have been performing at Leiden University and Delft University of Technology with collaboration with Prof. Herre Van der Zant.

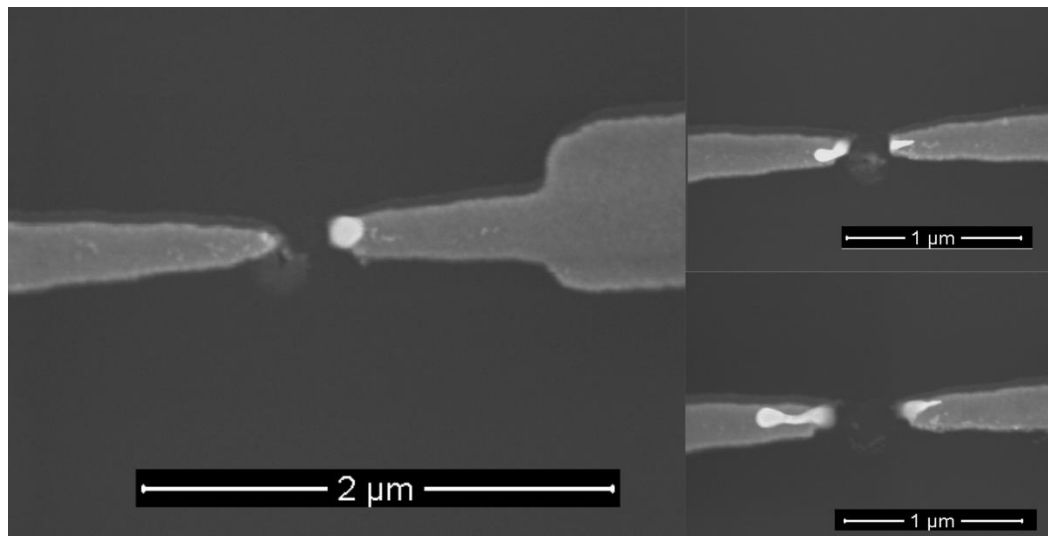


**Figure 5.15:** Samples damaged during I-V measurements.

## 5.6 Conclusion

At first, we used E-beam lithography (EBL) to fabricate SETs. The resolution of EBL limits its application to nanostructures with tens of nanometre resolution. Overdosing and shifting techniques were applied to create the tunnelling barrier but no successful fabrication was achieved by this technique. Then, we tried to fabricate the SETs by taking advantage of self-assembled Au nanorods and nano-particles. Although some positive results were obtained, and the desired assembly of NR-NP-NR could be achieved, the lack of facilities hindered further development of this project. Finally, we developed a hybrid fabrication method based on EBL and ALD, and we produced proper SETs. Electrical measurements were performed on our fabricated SETs but the measured I-V did not show the typical curve of a SET. Further investigation revealed that, in all cases, the SETs were damaged during the measurements. This damage was mostly caused by major defects in the electrical measurement setup that caused a sudden change in the electrical potential on the sample and blew it up. Electrical measurements still remain to be performed on our samples.



## References

- (1) Brenning, H.; Kubatkin, S.; Delsing, P. Fabrication of Aluminum Single-Electron Transistors with Low Resistance-Capacitance Product. *Journal of Applied Physics* **2004**, *96* (11), 6822–6826. <https://doi.org/10.1063/1.1806996>.
- (2) Hergenrother, J. M.; Tuominen, M. T.; Tighe, T. S.; Tinkham, M. Fabrication and Characterization of Single-Electron Tunneling Transistors in the Superconducting State. *IEEE Transactions on Applied Superconductivity* **1993**, *3* (1), 1980–1982. <https://doi.org/10.1109/77.233570>.
- (3) Ji, L.; Dresselhaus, P. D.; Han, S.; Lin, K.; Zheng, W.; Lukens, J. E. Fabrication and Characterization of Single-electron Transistors and Traps. *Journal of Vacuum Science & Technology B: Microelectronics and Nanometer Structures Processing, Measurement, and Phenomena* **1994**, *12* (6), 3619–3622. <https://doi.org/10.1116/1.587625>.
- (4) Joyez, P.; Lafarge, P.; Filipe, A.; Esteve, D.; Devoret, M. H. Observation of Parity-Induced Suppression of Josephson Tunneling in the Superconducting Single Electron Transistor. *Phys. Rev. Lett.* **1994**, *72* (15), 2458–2461. <https://doi.org/10.1103/PhysRevLett.72.2458>.
- (5) Wei, Y. Y.; Weis, J.; Klitzing, K. v.; Eberl, K. Edge Strips in the Quantum Hall Regime Imaged by a Single-Electron Transistor. *Phys. Rev. Lett.* **1998**, *81* (8), 1674–1677. <https://doi.org/10.1103/PhysRevLett.81.1674>.
- (6) Dolata, R.; Scherer, H.; Zorin, A. B.; Niemeyer, J. Single Electron Transistors with Nb/AlO<sub>x</sub>/Nb Junctions. *Journal of Vacuum Science & Technology B: Microelectronics and Nanometer Structures Processing, Measurement, and Phenomena* **2003**, *21* (2), 775–780. <https://doi.org/10.1116/1.1560213>.
- (7) MSM Nano Lab <https://nano.physics.leidenuniv.nl/> (accessed Oct 14, 2020).
- (8) Kavli Nanolab Delft <https://www.tudelft.nl/en/faculty-of-applied-sciences/about-faculty/departments/quantum-nanoscience/kavli-nanolab-delft/> (accessed Oct 14, 2020).
- (9) Yang, H.; Jin, A.; Luo, Q.; Li, J.; Gu, C.; Cui, Z. Electron Beam Lithography of HSQ/PMMA Bilayer Resists for Negative Tone Lift-off Process. *Microelectronic Engineering* **2008**, *85* (5), 814–817. <https://doi.org/10.1016/j.mee.2008.01.006>.
- (10) Haller, I.; Hatzakis, M.; Srinivasan, R. High-Resolution Positive Resists for Electron-Beam Exposure. *IBM Journal of Research and Development* **1968**, *12* (3), 251–256. <https://doi.org/10.1147/rd.123.0251>.
- (11) Chao, P. C.; Smith, P. M.; Palmateer, S. C.; Hwang, J. C. M. Electron-Beam Fabrication of GaAs Low-Noise MESFET's Using a New Trilayer Resist Technique. *IEEE Transactions on Electron Devices* **1985**, *32* (6), 1042–1046. <https://doi.org/10.1109/T-ED.1985.22071>.

- (12) Jr, R. E. F.; Katine, J. A.; Liu, J.; MacDonald, S. A.; Rooks, M. J.; Santini, H. A. E. Fully Undercut Resist Systems Using E-Beam Lithography for the Fabrication of High Resolution MR Sensors. US6821715B2, November 23, 2004.
- (13) Shi, X.; Verschueren, D.; Pud, S.; Dekker, C. Integrating Sub-3 Nm Plasmonic Gaps into Solid-State Nanopores. *Small* **2018**, *14* (18), 1703307. <https://doi.org/10.1002/sml.201703307>.
- (14) Chiew, H. T.; Tan, J.; Lim, S.; Lee, K. S.; Ren, L. Y.; Lee, B. C.; Quek, P. S.; Pey, K. S. Surface Morphology Change of Titanium Nitride Film after Metal Layer Photolithography Rework Causing Oxide Film De-Lamination. In *2006 IEEE International Integrated Reliability Workshop Final Report*; 2006; pp 213–214. <https://doi.org/10.1109/IRWS.2006.305249>.
- (15) Hoogvliet, J. C.; van Bennekom, W. P. Gold Thin-Film Electrodes: An EQCM Study of the Influence of Chromium and Titanium Adhesion Layers on the Response. *Electrochimica Acta* **2001**, *47* (4), 599–611. [https://doi.org/10.1016/S0013-4686\(01\)00793-9](https://doi.org/10.1016/S0013-4686(01)00793-9).
- (16) Hieber, H. Aging Properties of Gold Layers with Different Adhesion Layers. *Thin Solid Films* **1976**, *37* (3), 335–343. [https://doi.org/10.1016/0040-6090\(76\)90603-9](https://doi.org/10.1016/0040-6090(76)90603-9).
- (17) Makarenko, K. S.; Liu, Z.; Jong, M. P. de; Zwanenburg, F. A.; Huskens, J.; Wiel, W. G. van der. Bottom-Up Single-Electron Transistors. *Advanced Materials* **2017**, *29* (42), 1702920. <https://doi.org/10.1002/adma.201702920>.
- (18) Chen, X.; Park, H.-R.; Pelton, M.; Piao, X.; Lindquist, N. C.; Im, H.; Kim, Y. J.; Ahn, J. S.; Ahn, K. J.; Park, N.; Kim, D.-S.; Oh, S.-H. Atomic Layer Lithography of Wafer-Scale Nanogap Arrays for Extreme Confinement of Electromagnetic Waves. *Nature Communications* **2013**, *4* (1), 2361. <https://doi.org/10.1038/ncomms3361>.
- (19) *Handbook of Sputtering Technology*; Elsevier, 2012. <https://doi.org/10.1016/C2010-0-67037-4>.
- (20) Muller, D. A.; Sorsch, T.; Moccio, S.; Baumann, F. H.; Evans-Lutterodt, K.; Timp, G. The Electronic Structure at the Atomic Scale of Ultrathin Gate Oxides. *Nature* **1999**, *399*, 758–761. <https://doi.org/10.1038/21602>.
- (21) George, S. M.; Ott, A. W.; Klaus, J. W. Surface Chemistry for Atomic Layer Growth. *J. Phys. Chem.* **1996**, *100* (31), 13121–13131. <https://doi.org/10.1021/jp9536763>.
- (22) Groner, M. D.; Elam, J. W.; Fabreguette, F. H.; George, S. M. Electrical Characterization of Thin Al<sub>2</sub>O<sub>3</sub> Films Grown by Atomic Layer Deposition on Silicon and Various Metal Substrates. *Thin Solid Films* **2002**, *413* (1–2), 186–197. [https://doi.org/10.1016/S0040-6090\(02\)00438-8](https://doi.org/10.1016/S0040-6090(02)00438-8).
- (23) Higashi, G. S.; Fleming, C. G. Sequential Surface Chemical Reaction Limited Growth of High Quality Al<sub>2</sub>O<sub>3</sub> Dielectrics. *Appl. Phys. Lett.* **1989**, *55* (19), 1963–1965. <https://doi.org/10.1063/1.102337>.

(24) Dillon, A. C.; Ott, A. W.; Way, J. D.; George, S. M. Surface Chemistry of Al<sub>2</sub>O<sub>3</sub> Deposition Using Al(CH<sub>3</sub>)<sub>3</sub> and H<sub>2</sub>O in a Binary Reaction Sequence. *Surface Science* **1995**, *322* (1), 230–242. [https://doi.org/10.1016/0039-6028\(95\)90033-0](https://doi.org/10.1016/0039-6028(95)90033-0).

(25) de Vreede, L. J.; van den Berg, A.; Eijkel, J. C. T. Nanopore Fabrication by Heating Au Particles on Ceramic Substrates. *Nano Lett.* **2015**, *15* (1), 727–731. <https://doi.org/10.1021/nl5042676>.



# 6

## **Seeking for single-electron signals**

The discovery of the DBT/DBN molecular system with its high sensitivity to the electric field and the fabrication of SETs have paved the way to the optical detection of a single electron. However, there are still many challenges to overcome before achieving this goal. In this chapter, these challenges and the efforts to detect one single electron is described.

In chapter 4 we presented two methods based on using SETs to control and detect single charges. Although those methods require detailed knowledge of the electrical properties of the SETs (that are still under investigation), we performed optical measurements on our current SETs samples, which are reported in the present chapter.

## 6.1. Sample preparation

### 6.1.1. Crystal transfer to the chip

As we discussed in chapter 5, because of the high resistance and narrow insulator gaps of the junctions, the SETs are extremely sensitive to any potential change and to discharge of static electricity. Hence, the main and most important consideration in sample preparation is the protection of the sample against static charges. In all the steps from sample preparation to measurement, it is essential that sample, tools, and experimenter are properly grounded with the same ground.

The first step in preparing a sample is to transfer the DBT/DBN crystals to the chip. DBT molecules need to be placed within one hundred nanometers of the SETs to be able to sense the electric field of one electron. In chapter 2 we showed how DBT/DBN sublimated single crystal can be optically pasted on a glass surface. The same approach was used to attach the crystal to the chip and top of the SETs. Here, due to the presence of the nanostructures underneath the crystal, its contact surface with the sample is reduced and therefore its adhesion is reduced too. We also realized soon that imaging the SETs through the crystal is very challenging. This is because of the crystal anisotropy, of the difference in refractive index with the sample's environment and because of the thermal-change-induced cracks in the crystal which scatter the light. One solution to those problems is to use thinner crystals. Crystals with less thickness are more flexible and can bend between the nanostructure and better stick to the surface. Also, thinner crystals refract the light to a lesser extent, which improves the image quality. Further experiments have shown that crystals with a thickness of approximately 1 micrometre stick strongly enough to the surface.

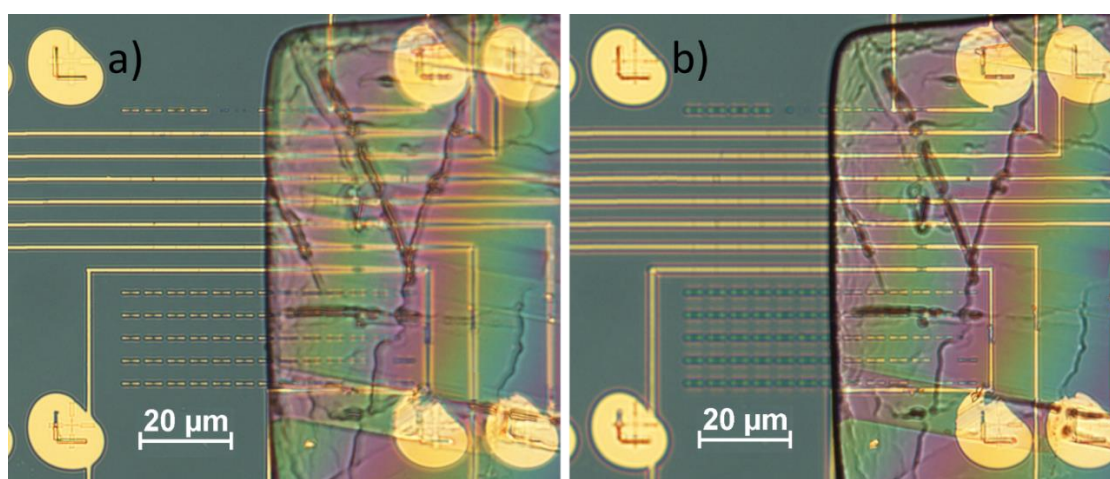


**Figure 6.1:** DBT/DBN crystal aligned and optically pasted on top of the SETs. a) Focused on the chip surface at the part without crystal. b) Focused on the nanostructure through the crystal.

The thickness of the crystals was measured before attaching them to the sample by a Broker DektakXT profilometer. The appropriate crystal was then transferred to the chip using steel

needles. Then, the crystal was adjusted on top of the SETs under an optical microscope. This step requires a lot of care and patience because any contact with lead electrodes can cause irreparable damage. Once the crystal was in place, it was gently pressed against the chip and stuck there. Figure 1.6 shows an example of a crystal successfully transferred to the chip. By comparing Figures 6.1.a and b, it is obvious that although the thickness of the crystal is only one micrometre, the difference in refractive index causes distortion and a large difference in focus.

### 6.1.2. Wire bonding

We used a wire bonder to connect the SETs to a chip holder and later to the power supply. A tiny droplet of silver paste was used to attach the chip to a chip holder attached to a printed circuit board. When the silver paste was dried and the chip was safely in place, all the pins on the circuit board were intermediately shorted from the back side and connected to same ground. This step was taken to prevent any potential change on the contact pad during wire bonding. A similar sample was used before wire bonding on the main sample to adjust wiring parameters such as power and time of ultrasound and applied force to the wire and contact pad. This significantly reduces the number of failed bonds. Since the contact pads are made of gold, we also used gold wire to have a stronger contact bond. The adhesion of wire bonding is often enhanced by heating up the sample, but this was ruled out in our case due to the presence of crystals on the chip. The wiring was always started with making the first bond on the chip holder then the second bond on the contact pad of the chip. This prevented damage to the contact pads if the bonding parameters were not properly adjusted. One of the contact pad of the holder was wired to the metal plate that the chip was pasted on it. This connection is the back gate and was used to manipulate the island potential. Therefore, Figure 6.2 shows the wire-bonded chip placed on the chip holder. The DBT/DBN crystal can be seen on top.

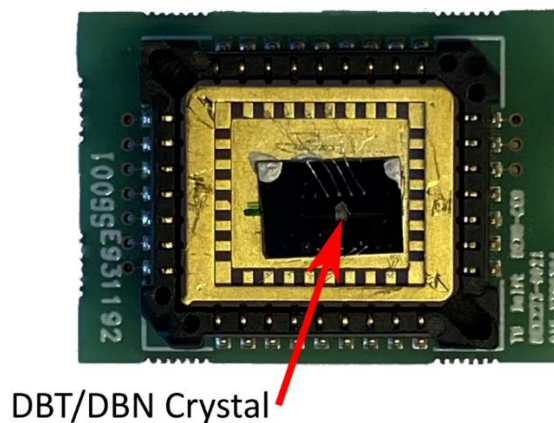


**Figure 6.2:** The fabricated chip wire bonded to the contact pads of the chip holder and held in place with conductive silver paste.

### 6.1.3. sample transportation

SETs are at more risk when they are connected to the big contact pads of the chip holder. To avoid damage during transportation, the chip holder was installed on the cryostat insert right after wiring and before disconnecting the intermediate shorts. The insert electrical contact pins are connected to a switch box showed in Figure 6.3. The switch box is designed to keep all the

pins at the same potential. Each individual key on the switch box has three states: ‘ground’ that internally connects the pins so they will be at the same potential, ‘off’ that disconnects the pins, and ‘measure’ that connects each pin to its related BNC connection. The BNC connections are used to apply voltages on the SETs electrodes. The switch box keys are kept on ‘ground’ during the preparation and cooling down. Also, all the other electrical connections such as temperature and pressure sensors, flow level meters for liquid helium and nitrogen, and vacuum pump were disconnected when the sample was inside the cryostat.

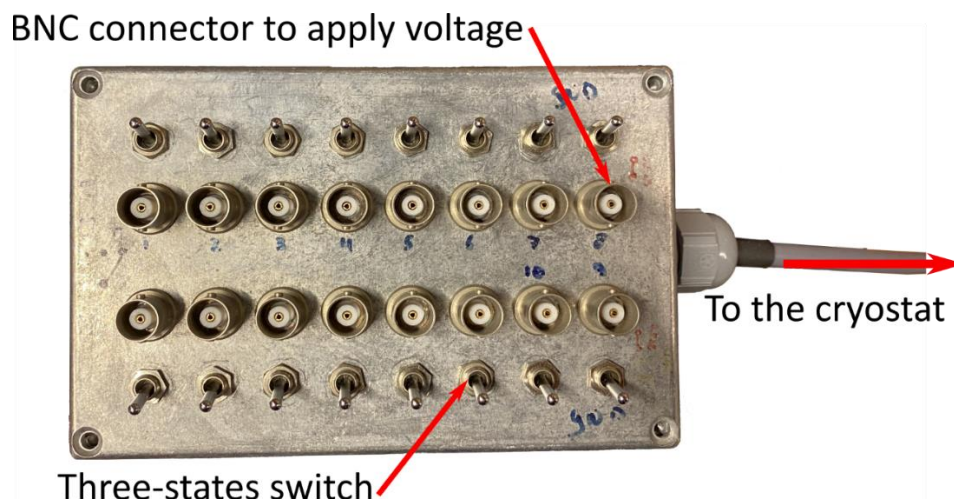


**Figure 6.3:** Home-made switch box to control SETs. The three-state switches are to ground, disconnect, and connect SET electrodes to the power supply.

## 6.2. Experimental section

The experiments were done at 1.2 K in a Janis flow cryostat. A tunable M-squared Ti:Sapphire equipped with TraScan unit and a WS6-200 HighFinesse wavemeter was used to excite DBT molecules at 756.6 nm, the wavelength of the ZPL of DBT/DBN (chapter 2). This laser system allows us to do excitation spectroscopy on molecules with sub-MHz resolution. A typical confocal microscope with a cryogenic objective (NA=0.8) was used for imaging. The same detector and sets of long-pass filters used in chapter 2 were used for detection of the fluorescence light.

Initially, a Keithley source-meter model 2450SMU was used to apply voltages on SET electrodes. However, we have found out that this Keithley device produces short and strong voltage pulses, especially when the voltage range is changed. These short pulses will unavoidably damage the SETs. To avoid damage caused by potential changes of commercial power supplies, a home-made battery-fed power supply was built and used to apply voltages. The power supply is shown in Figure 6.4. It is a very simple system with 4 batteries and two potentiometers that can provide up to 1.5 V on each of its 2 outputs with a resolution of 0.5 mV. The power supply outputs were connected to the switch box BNC connectors via short BNC cables (30 cm). Low bias voltages (0.5 mV) were applied to the source-drain electrodes and the gate voltage was scanned.





**Figure 6.4:** Home-made battery-fed power supply with two outputs and 0.5 mV resolution.

### 6.3. Results and Discussions

The biggest problem in optical measurements is determining the exact location of the SET islands. Figure 6.5 shows an example of sample images in reflection (6.5.a) and fluorescence (6.5.b) modes.

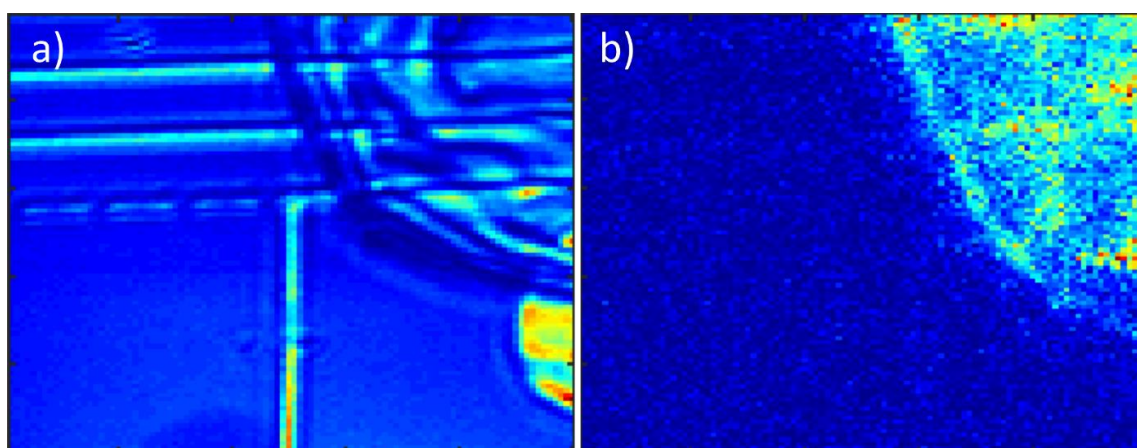


**Figure 6.5:** Confocal a) scattering and b) fluorescence images of the sample. The islands are not distinguishable in either case.

From these images, it is obvious that identifying the exact location of the islands is not easy. To feel the electric field of one electron, measurements must be done on molecules that are located a few hundred nanometres away from the island. Considering the size of islands (200 nm) and the imaging resolution that is about 400 nm, locating the islands is a serious challenge to the optical detection of an electron. Finally, the approximate location of the islands was determined by following the leads and the laser light was parked on the estimated position.

Another issue in optical measurements is finding molecules at the indicated spot. The TraScan unit brings the ability to scan the laser over large frequency ranges (THz scans). Applying this feature allowed us to find molecules at the desired spot. Figure 6.6 shows more than 6 molecules which were found at the estimated location of the island.

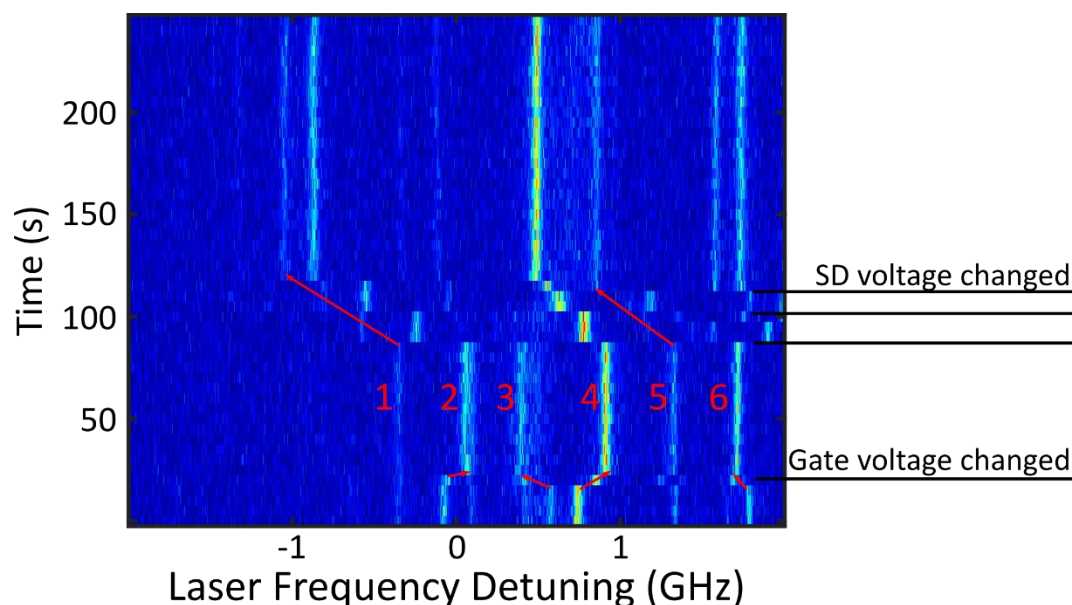


**Figure 6.6:** Molecule response to the Gate and Source-Drain electric field presents information about their approximate location.

First, the response of the molecule to the gate and source-drain (SD) voltages was investigated. The molecules' response to different applied electric fields gives information about their location. For convenience, the electric field caused by applied voltage to the gate and SD is called  $E_G$  and  $E_{SD}$  respectively. The first jump in Figure 6.6 is due to the  $E_G$  when all the other jumps (2<sup>nd</sup>, 3<sup>rd</sup> and 4<sup>th</sup>) are response to the  $E_{SD}$ . Molecules 2 and 4 were blue-shifted while molecules 3 and 6 were red-shifted with the  $E_G$ . That means their dipole moment is oriented differently with respect to the gate electric field. All 4 molecules were also shifted with  $E_{SD}$ , indicating that these molecules are placed close to the SD electrodes. Interestingly, molecule 1 and 5 did not show any shift under  $E_G$  while they jumped to the higher frequency under  $E_{SD}$ . Most probably these molecules are located on top of the island that the gate electric field is shielded by the island, but they were shifted by  $E_{SD}$ . Then by keeping the voltages constant, the molecules also remained stable.

In the case of molecules showed in Figure 6.6, many shifts were observed, generally due to the  $E_G$  and  $E_{SD}$ . This observation was also true in other measurements and molecules always showed a linear response to  $G_E$  and  $SD_E$ . In many cases, no distinct shift that could be specifically related to the presence of an electron in the molecule's vicinity could be observed or at least recognized. However, one case, shown in Figure 6.7, was an exception. In this measurement, again SD was in low bias and gate voltage was ramped up. The molecule does not show a large response to the  $E_G$  (the small shift is because of laser drift). This indicates that the molecule is on top of the island and does not feel  $E_G$ . Then suddenly at 25 mV for the gate voltage it jumped by 20 MHz (about one linewidth of ZPL). 25 mV is within the estimated size of a Coulomb diamond (50 mV) for the fabricated SETs. The jump can be a signal of adding one extra electron to the island and therefore, of the optical detection of one electron. But it may also have other reasons such as a sudden change in trapped charges distribution in the vicinity of the molecule (in the substrate, crystal, or aluminium oxide for instance) or charge leakage. Although there are compelling reasons to believe the observed jump is related to adding one extra electron to the island, without accurate knowledge of the electrical properties of SETs it is hard to make a definite statement about it.

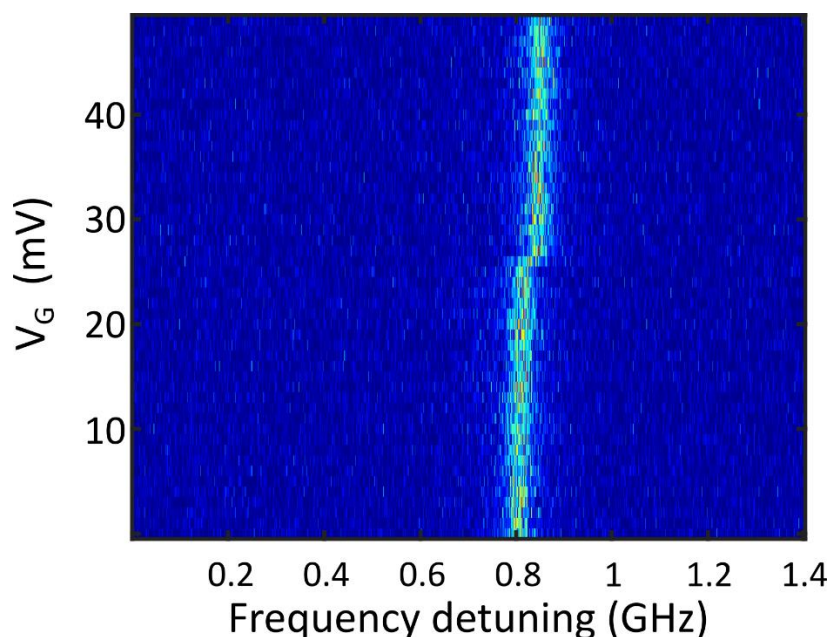


**Figure 6.7:** A molecule placed on top of the island experience a sudden shift of 20 MHz at gate voltage around 25 mV. The observed jump could indicate the presence of an extra electron on the island and indicate the optical detection of a single electron. The scan time was 250 s and molecule was extremely stable during the scan.

#### 6.4. Conclusion

In Chapter 2, the optical properties of DBT/DBN system were examined and it was shown that the DBT molecules are very stable and show large linear Stark shift. In this chapter DBT/DBN crystals were used for the optical detection of a single electron. Sample preparation and crystal transfer to the chip were discussed. Tips and precautions related to sample transportation and measurement preparation were stated. Despite the difficulties in identifying the location of the island, by investigating the response of molecules to the electric  $G_E$  and  $SD_E$ , information about the approximate location of molecule with respect to the island was obtained. Finally, in one of the measurements, a signal that possibly indicated the presence of an electron in the vicinity of the molecule was observed. However, it is hard to claim the optical detection of a single electron due to the lack of electrical properties of SETs and repetition of the measurement. The most important step in following is measuring the electrical properties of SETs and investing in performing simultaneous optical and electrical measurements.



# Summary

Single-molecule spectroscopy has become a powerful method for using organic fluorescent molecules in numerous applications. Along with sensing applications in biology and solid-state physics or a variety of applications in quantum information technology, molecules offer interesting possibilities for fundamental research. One of the very interesting areas is the study of charge transport and electric field sensing at the nanoscale. Developing molecular nanosensors for electric fields can not only help to fundamentally explore the motion of charges in conductors and semiconductors but can also lead to very sensitive and accurate instruments for quasi-static charge tracing or even single-electron charge detection. Such research could eventually lead to the construction of precise electric field sensors that can act as an interface between the quantum state of an electron and the outside world. With this in mind, we developed fluorescence molecular systems and electronic circuits with the aim of electric-field sensing and optical detection of one single electron. Chapter 1 gives a general overview of cryogenic single-molecule spectroscopy and Stark effect.

In Chapter 2 of this thesis, I describe a very sensitive molecular probe for the electric field. The system is based on embedding dibenzoterrylene (DBT) as the probe (guest) molecule in a 2,3-dibromonaphthalene (DBN) host matrix. Single crystals of DBN doped with DBT were grown by co-sublimation. DBT molecules embed along the crystal a-axis by replacing 3 host molecules. The herringbone structure of the DBN crystal introduces distortion and bending in a DBT molecule and breaks its symmetry. The DBT deformation combined together with the effect of electronegativity of the bromine atoms, induce a large electric dipole. The dipole moment change of 2.1 D was measured experimentally, which is in good agreement with the calculated dipole moment change of 2.46 D. As a result of inducing such a dipole moment, a large and homogeneous linear Stark shift of up to  $2 \text{ GHz/kVcm}^{-1}$  was measured for a DBT molecule. For a field of 10 kV/cm, this shift is 600 times larger than the linewidth of the molecule's Zero-Phonon line (ZPL) and indicates its high sensitivity to the electric field. We also studied the optical properties of the system. A very stable narrow ZPL with a linewidth of about 40 MHz and brightness of about  $10^7$  emitted photons per second were measured experimentally. Quantum chemistry calculations confirmed our finding of a large dipole moment of the DBT molecule induced by the host matrix. Our simulations confirmed that the insertion of DBT into the matrix unit cell can be done in 8 different ways, corresponding to the 8 matrix DBN molecules in the unit cell. Although these sites lead to different orientations of dipole moments (and therefore to different Stark coefficients in an arbitrarily applied electric field), in terms of optical transition energy, they all have the same energy due to the 3 mirror symmetries of the system. This system can be used for electric field probing in nanostructures or as an excellent tuneable single-photon emitter. More importantly for our project, it is an excellent candidate for optical single-electron detection.

In Chapter 3 we studied a novel phenomenon and described its capability to tune the optical transition of fluorescent molecules. The light-induced charge carrier in several guest/host molecular systems was explored. Generated charge carriers in the vicinity of the molecule generate a local electric field and produce a Stark shift. These charges have a long lifetime of the order of several hours. The generated Stark shift can be used for long-lived, electrode-less, fine tuning of optical transitions in fluorescent molecules. We then introduce a photoionization model, to describe the charge generation and propagation in the matrix. The effect was used to tune ZPLs of DBT molecules in three different host matrixes – polycrystalline naphthalene, single crystals of 2,3-dibromonaphthalene and anthracene nanocrystals. For the nanocrystals, a shift of more than 100 GHz was obtained. Our collaborators in Florence used the effect for frequency matching of 5 different DBT molecules spatially separated from each other. This fine tuning offers many possibilities for applications of molecules in quantum technologies such as integrating many single-photon emitters in molecular electronics and photonic circuits.

In Chapter 4, I introduce single-electron transistors (SETs). The working principles of SETs are discussed theoretically, and their operation and properties are presented. The number of electrons inside a finite island is an integer number and can be controlled precisely by adding electrons one by one, if the Coulomb blockade condition is satisfied. This offers the idea of trapping a single electron in a metallic island in the vicinity of a molecular probe that is sensitive to electric fields, such as the DBT/DBN system. This integrated circuit can be employed to detect a single electron optically. In this hybrid approach the number of electrons inside the island can be controlled electrically. Simultaneously, the molecule can translate the existence of extra electrons into a shift of its optical transition, that is detectable optically. Although SETs exist for decades, their use for this application requires specific conditions. The essential aspect is that the electric field created by the charged island should not be shielded by the leads or by any other bulk metal. A suitable configuration of a SET for single charge detection was designed. It consists of a 200 nm island with very pointed leads that have minimum overlap with the islands. A COMSOL simulation shows that the electric-field strength of a trapped electron in such a SET device can be sensed up to 200 nm away from the island, considering DBT in DBN as the probe molecule.

Considering all the requirements and the facilities in our lab, a fabrication method was developed to manufacture the SETs. In Chapter 5, the different fabrication approaches used are presented. The effort started with e-beam lithography. Despite using several tricks such as overdosing the electrodes with respect to the island in a SET configuration, the poor resolution of e-beam lithography prevented the fabrication of the tunnelling gap. Another fabrication method based on self-assembly of gold nanoparticles and nanorods was developed. 40 nm gold nanospheres (as island) were assembled in between two nanorods (as electrodes) by using homocysteine molecules as the linker. The lack of dedicated fabrication facilities prevented us from following up this approach. Finally, a 10-step hybrid method was developed to fabricate the SETs. In this method the e-beam resolution limit was overcome by separating islands from electrodes with an insulating layer that acts as the tunnelling gap. In this method, 200 nm islands were patterned using

e-beam lithography, and then a tunnelling gap was grown with atomic resolution using atomic layer deposition. The ability to precisely control the thickness of the insulating layer allows us to create a broad distribution of tunnelling gaps. A large number of transistors were damaged during transportation and electrical measurement by static electricity and instability of the electrical potential in the electronic setup. After failing to measure the SETs in Leiden, we pursued the electrical measurements in collaboration with Professor H. van der Zant's group at Delft University of Technology.

In chapter 6, the efforts to detect one electron optically is described. The DBT:DBN crystal was optically pasted on the fabricated chip. The optical measurements were performed at 1.2K by immersing the sample in liquid helium. Due to the difference between the refractive index of the crystal (1.6) and the liquid helium (1.02) and to the formation of many cracks in the crystal during cool-down, finding the SETs underneath the crystal turned out problematic. The approximate location of the islands was determined using the matching of microscopic images and studying the molecular response to source-drain and gate electric field. Afterwards, source-drain were kept in low bias voltage and the gate voltage was scanned while excitation spectrum of the molecule was recorded. Gate voltage manipulates the potential of the island and allows one electron to enter the island at a certain voltage. Therefore, the electric field of the electron can be observed as a jump in the molecular spectrum or nonlinearity in the Stark shift. Although such a signal was observed, the reproducibility was not sufficient to claim optical detection of a single electron. The efforts to detect one electron optically are being continued.





# Samenvatting

De spectroscopie van een enkel molecuul heeft een krachtige methode opgeleverd om fluorescerende organische moleculen in tal van studies toe de passen. Naast detectie toepassingen in de biologie en vastestoffysica, of in de kwantuminformatie technologie, zijn moleculen ook interessante studie objecten voor fundamenteel onderzoek. Een van de zeer boeiende gebieden is ladingstransport en de detectie van elektrische velden op nanoschaal. Het ontwikkelen van moleculaire nanosensoren voor elektrische velden kan niet alleen helpen om de beweging van ladingen in geleiders en halfgeleiders op fundamenteel niveau te onderzoeken, maar kan ook leiden tot zeer gevoelige en nauwkeurige instrumenten voor quasi-statische ladingsopsporing of zelfs ladingsdetectie van één enkel elektron. Dergelijk onderzoek zou uiteindelijk kunnen leiden tot de constructie van nauwkeurige elektrische-veldsensoren die kunnen fungeren als interface tussen de kwantumtoestand van een elektron en de buitenwereld. In dit verband hebben we moleculaire fluorescentiesystemen en elektrische netwerken ontwikkeld met als doel de elektrische-veld detectie en optische detectie van een enkel elektron. Hoofdstuk 1 geeft een algemeen overzicht van de spectroscopie van een enkel molecuul en van het Stark-effect.

In Hoofdstuk 2 van dit proefschrift hebben we een zeer gevoelige moleculaire sonde van het elektrische veld ontwikkeld. Het systeem is gebaseerd op het integreren van dibenzoterryleen (DBT) als het sondemolecuul (gast) in een 2,3-dibroomnaftaleen (DBN) gastheermatrix. Eénkristallen van DBN gedoteerd met DBT zijn gegroeid door co-sublimatie. DBT-moleculen worden geïntegreerd langs de a-as van het kristal door drie gastheermoleculen te vervangen. De visgraatstructuur van het DBN-kristal introduceert vervorming en buiging in een DBT-molecuul en breekt de symmetrie ervan. De DBT-vervorming gecombineerd met het effect van elektronegativiteit van de broom-atomen induceert een grote elektrische dipool. De gemeten dipoolmoment verandering van 2,1 D komt goed overeen met de berekende dipoolmoment verandering van 2,46 D. Als gevolg van het induceren van zo'n dipoolmoment is er voor een DBT-molecuul een grote en homogene lineaire Stark verschuiving van maximaal 2 GHz /  $\text{kVcm}^{-1}$  gemeten. Voor een veld van 10 kV / cm is deze verschuiving 600 keer groter dan de lijnbreedte van de ZPL "Zero-Phonon line" van het molecuul. Dit duidt dit op een grote gevoeligheid voor elektrische velden. We hebben ook de optische eigenschappen van het systeem bestudeerd. Een zeer stabiele, smalle ZPL met een lijnbreedte van ongeveer 40 MHz en een helderheid van ongeveer  $10^7$  uitgezonden fotonen per seconde zijn gemeten. Kwantumchemische berekeningen bevestigen onze vondst van een groot, door de gastheermatrix geïnduceerd dipoolmoment van het DBT-molecuul. Moleculaire-mechanica simulaties bevestigen dat het invoegen van DBT in de eenheidscel van de matrix op acht verschillende manieren kan gebeuren, wat overeenkomt met de acht matrix-DBN-moleculen in de eenheidscel. Hoewel deze plekken tot verschillende oriëntaties van dipoolmomenten (en dus tot verschillende Stark-coëfficiënten in een willekeurig aangelegd elektrisch veld) leiden, hebben ze allemaal dezelfde energie dankzij de drie spiegelsymmetrieën van het systeem. Dit

systeem kan worden gebruikt voor het meten van elektrische velden in nanostructuren of als een uitstekend afstembare lichtbron van éénfoton toestanden. Wat nog belangrijker is voor ons project, is dat het een uitstekende kandidaat is voor optische detectie van één elektron.

In Hoofdstuk 3 hebben we een nieuw fenomeen bestudeerd en het vermogen ervan om de optische overgang van fluorescerende moleculen af te stemmen. In verschillende gast/gastheer moleculaire systemen zijn de door licht geïnduceerde ladingdragers onderzocht. Ladingdragers in de buurt van het molecuul genereren een lokaal elektrisch veld en produceren een Stark-verschuiving. Deze ladingen hebben een lange levensduur: van de orde van enkele uren. De geproduceerde Stark-verschuiving kan worden gebruikt voor langdurige, elektrode-vrije fijn-afstemming van optische overgangen in fluorescerende moleculen. Vervolgens introduceren we een foto-ionisatiemodel om de ladingsopwekking en -propagatie in de matrix te beschrijven. Het effect is gebruikt om ZPL's van DBT-moleculen af te stemmen in drie verschillende gastheermatrices: polykristallijn naftaleen, 2,3-dibroomnaftaleen éénkristallen, en antraceen nanokristallen. Bij nanokristallen werd een verschuiving van meer dan 100 GHz verkregen. Onze collega's in Florence hebben dit effect gebruikt voor frequentiematching van 5 verschillende ruimtelijk van elkaar gescheiden DBT-moleculen. Het afstemmen biedt allerlei toepassingen van moleculen in kwantum-technologieën, zoals de integratie van veel éénfoton lichtbronnen in moleculaire elektronica en fotonische schakelingen.

In Hoofdstuk 4 van dit proefschrift heb ik éénelektron transistoren (SETs) geïntroduceerd. De werkingsprincipes van SETs worden theoretisch besproken, en hun werking en eigenschappen gepresenteerd. Het aantal elektronen binnen een eindig eiland is een geheel getal en kan nauwkeurig worden geregeld door elektronen één voor één toe te voegen wanneer aan de voorwaarde van de Coulomb blokkade is voldaan. Dit maakt het mogelijk om één enkel elektron te vangen in een metalen eiland in de buurt van een moleculaire sonde die gevoelig is voor elektrische velden, zoals een DBT/DBN-systeem. Deze geïntegreerde schakeling kan worden toegepast om één elektron optisch te detecteren. Bij deze hybride benadering kan het aantal elektronen binnen het eiland elektrisch worden aangestuurd. Tegelijkertijd kan het molecuul het bestaan van extra elektronen vertalen naar een verschuiving van de optische overgang die detecteerbaar is. Hoewel SETs al tientallen jaren bestaan, vereist het gebruik ervan voor deze toepassing specifieke voorwaarden. Het essentiële aspect is dat het elektrische veld dat wordt gecreëerd door het geladen eiland niet mag worden afgeschermd door de toevoer draden of door enig ander bulkmateriaal. Er is een geschikte configuratie van SETs voor detectie van enkele lading ontworpen. Het bestaat uit een 200 nm groot eiland met heel puntige toevoerdraden die minimale overlap met de eilanden hebben. Een COMSOL-simulatie laat zien dat de elektrische veldsterkte van een gevangen elektron in zo'n SET tot 200 nm van het eiland kan worden waargenomen, waarbij DBT in DBN wordt beschouwd als het sondemolecuul is.

Rekening houdend met alle vereisten en de faciliteiten in ons laboratorium, is een fabricagemethode ontwikkeld om de benodigde SET's te vervaardigen. In Hoofdstuk 5 worden de verschillende fabricage methoden gepresenteerd. De inspanning begon met elektronenbundel lithografie. Ondanks het gebruik van verschillende trucs, zoals overdosering van de elektroden ten opzichte van het eiland in een SET-configuratie, verhinderde de slechte resolutie van de elektronenbundel de fabricage van de tunnel opening. Vervolgens is er een andere fabricagemethode ontwikkeld op basis van zelfassemblage van gouden nanodeeltjes en nanostaafjes. Veertig nanometer grote gouden nanobolletjes (als eiland) zijn gepositioneerd tussen twee nanostaafjes (als elektroden) door het gebruik van homocysteïne moleculen als

verbinding. Door het ontbreken van speciale fabricagemogelijkheden konden we niet verder gaan met deze aanpak. Tenslotte werd een tien-stappen hybride methode ontwikkeld om de SETs te fabriceren. Bij deze methode werd de resolutielimiet van de elektronenbundel overwonnen door eilanden van elektroden te scheiden met een isolatielaag die fungeert als de tunnel opening. Bij deze methode zijn eilanden van 200 nm van een patroon voorzien met behulp van elektronenbundel-lithografie, en vervolgens is de tunnel opening met behulp van atomaire depositie met atomaire resolutie gegroeid. Het vermogen om de dikte van de isolatielaag nauwkeurig te beheersen stelt ons in staat een brede verdeling van tunnelopeningen te maken. Een groot aantal transistoren is tijdens het transport en elektrische meting beschadigd geraakt door statische elektriciteit en instabiliteit van de elektrisch potentiaal in de elektronische opstelling. Omdat we de SETs in Leiden niet hadden kunnen meten, hebben we de elektrische metingen voortgezet in samenwerking met de groep van professor H. van der Zant aan de Technische Universiteit Delft.

In hoofdstuk 6 worden de pogingen om één elektron optisch te detecteren beschreven. Het DBT: DBN-kristal is op de gefabriceerde chip geplakt. De optische metingen werden uitgevoerd bij 1,2 K door het monster onder te dompelen in vloeibaar helium. Door het verschil tussen de brekingsindex van het kristal (1,6) en het vloeibare helium (1,02), alsmede de vorming van vele scheuren in het kristal tijdens het afkoelen, bleek het moeilijk om de SETs onder het kristal te vinden. De geschatte locatie van de eilanden werd bepaald door het matchen van microscopie beelden en het bestuderen van de reactie van de moleculen op de source-drain spanning en het aan de gate aangelegde elektrische veld. Daarna werd het source-drain spanningsverschil laag gehouden en werd de gate-spanning gescand terwijl het excitatiespectrum van het molecuul opgenomen werd. De gate spanning manipuleert de potentiaal van het eiland en laat het eiland een elektron bij een bepaalde spanning binnen. Daarom kan het elektrische veld van het elektron worden waargenomen als een sprong in het moleculaire spectrum of een niet-lineariteit in de Stark verschuiving. Hoewel een dergelijk signaal werd waargenomen, was de reproduceerbaarheid niet voldoende om optische waarneming van elektronenbundel enkel elektron te claimen. De inspanningen om één enkel elektron optisch te detecteren worden voortgezet.



# Curriculum Vitae

I was born on 11th April 1985 in Shahrood, Iran. I got my bachelor's degree in Optics and Laser Engineering at Malek-Ashtar University of Technology, Isfahan, Iran in 2009. I then started my Master education at the Institute for Advanced Studies in Basic Science, Zanjan, Iran in 2011. Under the supervision of Dr. Akhlaghi I worked on a phase-shifting digital holography-based method to determine the temperature profile around a laser-heated particle. After obtaining my MSc degree in 2014, I entered mandatory military services and was conscripted to serve as a teacher in outlying villages. During this time, I enjoyed teaching Physics and Mathematics to young students. In April 2016, I started my PhD in the group of Prof. dr. Michel Orrit at Leiden University. My research during that period was in the field of single-molecule spectroscopy with the goal of optical detection of a single electron.



# List of Publication

1. A. Moradi, Z. Ristanović, M. Orrit, I. Deperasińska, B. Kozankiewicz, *Matrix-induced Linear Stark Effect of Single Dibenzoterrylene Molecules in 2,3-Dibromonaphthalene Crystal*, *ChemPhysChem* 2019, **20**, 55-61.
2. Maja Colautti, Francesco S. Piccioli, Zoran Ristanović, Pietro Lombardi, Amin Moradi, Subhasis Adhikari, Irena Deperasinska, Boleslaw Kozankiewicz, Michel Orrit, and Costanza Toninelli, *Laser-Induced Frequency Tuning of Fourier-Limited Single-Molecule Emitters*, *ACS Nano* **2020 14** (10), 13584-13592.





# Acknowledgments

During my Ph.D. journey many people have contributed towards the work reported in this thesis. Some of them helped in the professional area and many in the private domain. I like to acknowledge their contribution here.

First and foremost, I express my gratitude to my supervisor, Prof. Michel Orrit. Your guidance throughout all the stages of my Ph.D. has been fundamental for its completion. Your broad knowledge and passion for science has been very inspiring and motivates me always. I really appreciate your endless support to me to overcome the issues both in academic and my private life. Where I am now, would not have been possible without your patience during all this time.

Many thanks to Dr. Zoran Ristanovic for working alongside me in the lab and having day to day discussions. I am honored to be able to work with you and having your guidance and help during writing. I would also like to thank Prof. Sense Jan van der Molen for being my second supervisor contributing to the electrical part of the project as well as scientific thoughts whenever needed. I am thankful to Dr. Sanli Faez for his broad scientific advice and creative ideas.

I owe a big thank to Nico Verhart who taught me how to work with the setups and equipment in the low- temperature lab. Dr. Subhasis Adhikari, for help in the experiments and data analysis. A special acknowledgment goes to Prof. Bolesław Kozankiewicz and Dr. Irena Deperasińska for providing DBT/DBN crystals and doing quantum chemistry calculation. I would like to thank Dr. Sergii Pud for giving advice on nanofabrication and doing atomic layer deposition. Special thanks to Prof. Herre van der Zant for giving me the opportunity to do experiments in his lab in Delft and his scientific support with the electrical measurements.

I would like to thank Henriette van Leeuwen and Annette Bor for carefully handling so much paperwork, Harmen van der Meer for mechanical support, Peter van Veldhuizen, Raymond Koehler, Rene Overgaw for providing support on electronics, Wilferd van der Geest for supplying liquid Helium, Douwe Scholma and Marcel Hesselberth for teaching me how to use the cleanroom facilities, Dr. Mojtaba Nasiri for helping with COMSOL simulation, Lenart de Bruin for the Dutch translation of the summary.

Thanks to Niloofar Moosavi, for the effort she put in the cleanroom to improve the fabrication recipe. Thanks to Kaveh, for his genius constructive advice on nanofabrication. Many thanks to Christopher for scientific discussion and his help in organizing social events. Maria and Wouter thanks for helping with the electrical measurements. Peter Gast and Wolfgang Löffler, thank you for all your help with my teaching-assistant duties, it was enjoyable working as a TA with you. I owe a big thanks to Prof. Edgar Groenen for generously offering me his time to talk about my personal issues.

My gratitude should go beyond my PhD period. I am thankful to all the professors and teachers from my masters, bachelors, and high school periods. Mr. Farokhzadeh, your enthusiasm in teaching Physics sparked my interest in Physics. Dr. Akhlaghi, Dr. Reihani and Dr. Hajizade, all the progress I made would not have happened without the knowledge you taught me. I believe our friendship has been always much beyond the student-teacher communication.

I am deeply grateful for the boundless love, care and support of my parents, sisters, and grandparents. Mom and dad, I heard from many of your students that you have always been inspiring and compassionate teachers. You always helped me in my studies but the biggest lesson I learned from you was love, kindness and patience.

My PhD period would not have been this wonderful without all my friends in Leiden and Delft: Enrico, Thomas, Biswajit, Martín, Martin, Xueyan, Aquiles, Hamed, Ali, Weichun, Gabriele, Hamideh, Nelli, Gesa, Esmee, Christopher, Robert, Sid, Xuxing, Nasrin, Zohre, Eduardo, Martina, Christopher, Deep, Weibke, Mina, Arash, Negar, Sonya, Masoud, Sahar, Siamak, Khatere, Marjan, Vahid, Elnaz, Darya, Artemis, Sirous, Babak, Pooyan, Sadaf, Melika, Reza, Hanie, Mohamad, Hamraz, Bahar, Bahareh, Mahpar, and all the others with whom I had nice moments together and whose name I may not have mentioned. I am sending you all my best wishes and hope you are always happy, healthy, and successful.